

Molecular models for water vapor flows in silica nanopores

Citation for published version (APA):

Kim, J. (2014). *Molecular models for water vapor flows in silica nanopores*. [Phd Thesis 1 (Research TU/e / Graduation TU/e), Mechanical Engineering]. Technische Universiteit Eindhoven.
<https://doi.org/10.6100/IR781466>

DOI:

[10.6100/IR781466](https://doi.org/10.6100/IR781466)

Document status and date:

Published: 01/01/2014

Document Version:

Publisher's PDF, also known as Version of Record (includes final page, issue and volume numbers)

Please check the document version of this publication:

- A submitted manuscript is the version of the article upon submission and before peer-review. There can be important differences between the submitted version and the official published version of record. People interested in the research are advised to contact the author for the final version of the publication, or visit the DOI to the publisher's website.
- The final author version and the galley proof are versions of the publication after peer review.
- The final published version features the final layout of the paper including the volume, issue and page numbers.

[Link to publication](#)

General rights

Copyright and moral rights for the publications made accessible in the public portal are retained by the authors and/or other copyright owners and it is a condition of accessing publications that users recognise and abide by the legal requirements associated with these rights.

- Users may download and print one copy of any publication from the public portal for the purpose of private study or research.
- You may not further distribute the material or use it for any profit-making activity or commercial gain
- You may freely distribute the URL identifying the publication in the public portal.

If the publication is distributed under the terms of Article 25fa of the Dutch Copyright Act, indicated by the "Taverne" license above, please follow below link for the End User Agreement:

www.tue.nl/taverne

Take down policy

If you believe that this document breaches copyright please contact us at:

openaccess@tue.nl

providing details and we will investigate your claim.

Molecular models for water vapor flows in silica nanopores

PROEFSCHRIFT

ter verkrijging van de graad van doctor aan de
Technische Universiteit Eindhoven, op gezag van de
rector magnificus, prof.dr.ir. C.J. van Duijn, voor een
commissie aangewezen door het College voor
Promoties, in het openbaar te verdedigen
op donderdag 13 november 2014 om 16.00 uur

door

Junghan Kim

geboren te Seoul, Zuid-Korea

Dit proefschrift is goedgekeurd door de promotor en copromotoren.
De samenstelling van de promotiecommissie is als volgt:

voorzitter:	prof.dr.	L.P.H. de Goey
promotor:	prof.dr.ir.	A.A. van Steenhoven
copromotoren:	dr.ir.	A.J.H. Frijs
	dr.	S.V. Nedeaa
leden:	prof.dr.	A. Frezzotti (Politecnico di Milano)
	prof.dr.ir.	C.R. Kleijn (TU Delft)
	prof.dr.	P.A.J. Hilbers
	prof.dr.ir.	D.M.J. Smeulders

*God doesn't play dice with the world...
But, we play dice to understand his work.*

This work was financially supported by the European Community's Seventh Framework Program FP7/2007-2013 under grant agreement ITN GASMEMS 215504.

Copyright © 2014 by J. Kim

All rights reserved. No part of this publication may be reproduced, stored in a retrieval system, or transmitted, in any form, or by any means, electronic, mechanical, photocopying, recording, or otherwise, without the prior permission of the author.

Printed by Gildeprint Drukkerijen - Enschede

A catalog record is available from the Eindhoven University of Technology Library

ISBN: 978-90-386-3723-5

Contents

1	Introduction	1
1.1	Motivation and background	1
1.2	Research objective and thesis outline	4
2	Simulation methods for flow and heat transfer in micro- and nanosystems	7
2.1	Introduction	7
2.2	Molecular Dynamics	8
2.2.1	Introduction to MD	8
2.2.2	PumMa Molecular Dynamics	11
2.2.3	Boundary conditions	12
2.2.4	Macroscopic properties	17
2.2.5	Controllers	20
2.2.6	Parallelization of the computations	23
2.3	ReaxFF	25
2.4	Direct Simulation Monte Carlo	28
2.5	Conclusion	33
3	Geometry effects on rarefied nanochannel flows	35
3.1	Introduction	35
3.2	Method	37
3.2.1	Methods outline	37
3.2.2	Validation of the method	40
3.3	Results and discussion	41
3.3.1	Data and error analysis	41
3.3.2	Velocity profile	44
3.3.3	Slip velocity for different Knudsen numbers	45
3.3.4	Maximum and average velocity	50
3.3.5	Flow rates in 2D(slit) and 3D(circular and rectangular) geometries	50
3.3.6	Effects of the accommodation coefficient on the average velocity	51
3.4	Conclusion	55

4	Geometry effects on choked subsonic nanochannel flows in the transition regime	57
4.1	Introduction	58
4.2	Methods	58
4.2.1	Molecular Dynamics	59
4.2.2	Direct Simulation Monte Carlo	60
4.2.3	Sampling	62
4.3	Expansion flow with an isothermal wall condition (wall temperature 300K)	63
4.3.1	Pressure	63
4.3.2	Velocity	64
4.3.3	Temperature	66
4.4	Expansion flow with heated walls (wall temperature 400K)	67
4.5	Conclusion	70
5	Optimization of flexible three site water models	73
5.1	Introduction	73
5.2	Simulation method	75
5.2.1	PumMa Molecular Dynamics	75
5.2.2	Liquid density	76
5.2.3	Self-diffusion coefficient	76
5.3	Water models	77
5.3.1	Modified TIP3P models	77
5.3.2	Tabulated potential water model	83
5.3.3	Comparison with other models	90
5.4	Conclusion	92
6	Development of EEM based silicon-water and silica-water wall potentials for non-reactive Molecular Dynamics simulations	95
6.1	Introduction	95
6.2	Tabulation process	97
6.2.1	Crystal structure	97
6.2.2	Si-OH ReaxFF force field	99
6.2.3	Final tabulated potentials	105
6.3	Validation of wall potential	107
6.3.1	Validation method	107
6.3.2	Results and discussion	109
6.4	Conclusion	111
7	Molecular simulation of water vapor outgassing from silica nanopores	113
7.1	Introduction	113
7.2	Method	114
7.2.1	Simulation details	114
7.2.2	Half-life	117
7.3	Results and discussion	118

7.3.1	Effect of outlet pressure	118
7.3.2	Effect of temperature	119
7.3.3	Effect of geometry	122
7.3.4	Effect of materials	126
7.4	Conclusion	128
8	Conclusions and Recommendations	129
8.1	Conclusions	129
8.2	Recommendations for further research	131
	Postface	133
A	Pressure calculation in nanochannel flow	135
A.1	Pressure calculation in developing flow	135
A.2	Boundary effect	137
B	Expansion flow with heated walls	139
B.1	Pressure	139
B.2	Velocity	139
	Bibliography	143
	Nomenclature	158
	Summary	161
	Acknowledgements	163
	List of publications	165
	Curriculum vitae	167

1

1.1 Motivation and background

Gas flows in micro- and nanosystems are of great importance both for scientific reasons and for various practical applications, like fluidic micro-actuators for active control of aerodynamic flows, vacuum generators for extracting biological samples, mass flow and temperature micro-sensors, pressure gauges, micro heat-exchangers for the cooling of electronic components or for chemical applications^[1].

The research is also related to many of the problems occurring in industry. For instance, one of the biggest concerns which can be found in semiconductor industry is the outgassing problem. Outgassing refers to gaseous emissions from solids which have been adsorbed previously^[86]. It is usually caused by exposure to high operating temperature and/or low external pressure.

Outgassing can create problems in many ways. First of all, it creates a problem for the wafer level packaging. Wafer level packaging is essential for miniaturization and high level integration of semiconductor industry. It allows the encapsulation of micro electro mechanical systems (MEMS) or integrated circuits (IC), by using micro-machining technology before the standard IC packaging process. Wafer bonding is a key technology for wafer level packaging in MEMS applications. By bonding a cap wafer to a MEMS, the mechanical structures can be sealed in a package and protected against the outside environment. Unwanted gasses are sometimes created within the sealed micro structures during or after wafer bonding^[60]. Outgassing may create bubbles at the bonded interface or destroy the vacuum in the sealed micro cavity. This can degrade the reliability of MEMS and nano electro mechanical systems (NEMS) and can lead to a failure in the device^[35].

Outgassing sometimes creates problems also during the wafer bonding process. Fusion bonding of silicon is a very commonly used wafer bonding technology due to its simplicity and high bond strength^[103]. During the bonding pro-

cess, wafer surfaces are brought into contact (pre-bonded) in vacuum followed by high temperature annealing to strengthen the bond. Outgassing of water molecules remaining in the MEMS wafer, before wafer bonding, was found to be the main reason for bonding failures^[60].

Another problem of outgassing is that it can be a source of contamination of the vacuum chamber where ultra high vacuum (UHV) is necessary. UHV may be roughly defined as vacuum pressures below $10^{-8}mbar$, and it is becoming more important since it is required for extreme ultraviolet (EUV) lithography. EUV lithography is one of the most promising methods for next generation device manufacturing for semiconductor industry^[106]. Study of water outgassing is important since water is a dominant background medium in vacuum processing chambers^[106]. It can cause contamination and oxidation on multilayer reflecting optics surfaces. It will not only reduce system throughput because of the associated reduction in EUV reflectivity, but also introduce wavefront aberrations that compromise the ability to print uniform features^[106].

Other than in the semiconductor industry, the study of outgassing can be also used to solve problems in spacecraft industry. McMullin et al. showed that water contamination can degrade the optical instruments in a spacecraft^[113]. Neutral gas mass spectrometers are also affected because very thin atmospheres can be completely obscured by outgassing^[136]. Outgassing of water can even perturb spacecraft control during maneuvers by the recoil force exerted by the gas for non isotropic outgassing^[150].

Considering the great complexity of micro-fabrication processes, the understanding of outgassing behavior also becomes a very complex task: it is dependent on temperature, outlet pressure, geometry, surface materials, etc. All these complicated behaviors have to be understood and controlled.

In order to understand the nature of outgassing happening in the micro- and nano system, it is necessary to develop fundamental knowledge on multi phase micro- and nano flow, especially for gases and vapors. The prediction of the behavior in micro- and nano gas flows is challenging due to the large surface area to volume ratios of the flows causing dominating surface effects, large spatial gradients of the flow parameters and rarefaction effects, and the breaking down of the continuum description.

The rarefaction degree is commonly determined by the Knudsen number, Kn . The Knudsen number is defined as the ratio of the average traveling distance of molecules in between successive collisions λ , and the characteristic length scale L of the gas flows.

$$Kn = \frac{\lambda}{L}. \quad (1.1)$$

The mean free path λ is defined as:

$$\lambda = \frac{1}{\pi\sqrt{2}\sigma^2n} \quad (1.2)$$

where, n is the number density and σ is the diameter of the molecules^[29].

Micro gas flows are normally classified as rarefied due to their inherent small length-scale. Several flow regimes can be distinguished^[89]:

- For $Kn \leq 10^{-2}$, the fluid flow can be considered as a continuum flow.
- For $10^{-2} < Kn < 0.1$, it is considered as a slip flow.
- For $0.1 < Kn < 10$, it is considered as a transition flow.
- For $Kn \geq 10$, it is considered as a free molecular flow.

Rarefaction effects become more important as the Knudsen number increases. The limits of a continuum model can be overcome by using a particle-based method such as Direct Simulation Monte Carlo (DSMC)^[20] and Molecular Dynamics (MD). The particle-based methods do not assume that the medium is continuous, and therefore they are computationally much more expensive. DSMC is often preferred for gas flows as it is computationally faster compared to MD. However, DSMC is not appropriate to simulate liquid and solid. It is also not preferred for the flow inside a channel with a complicated atomic structure (e.g. silica wall), as the effect of complex gas-wall interaction is dominant in small channels. Sophisticated boundary conditions in DSMC are not always able to capture these effects.

Molecular Dynamics is a method that can be used to study all three different phases of a substance, but is limited by spatial and time restrictions because of computational resources. It suits our following needs to study gas dynamics in nano scale system. It is a method that:

- can cover both liquid and vapor phases.
- can model polyatomic molecules.
- can describe gas-surface interactions including wetting and adsorption effects.

In the classical mechanics approach of MD simulations molecules are treated as classical objects, resembling very much the ‘ball and stick’ model^[114]; atoms correspond to soft balls and elastic sticks correspond to bonds. The laws of classical mechanics define the dynamics of the system. The ‘quantum’ or ‘first-principle’ MD simulations, which started in the 1980s with the seminal work of Car and Parinello^[28], take explicitly into account the quantum nature of the chemical bond. The electron density function for the valence electrons, that determine bonding in the system, is computed using quantum equations, whereas the dynamics of ions is followed classically. In our study, classical non-reactive MD simulation will be the backbone simulation technique to study heat and flow. However, ‘first principle’ reactive force field MD simulation will also be used to help building up the parts that are needed for classical MD simulation.

As mentioned before, the time limitation is the most severe problem in MD simulations. Relevant time scales for heat and mass flow process extend over

many orders of magnitude. For example, the condensation of water takes tens of picoseconds, whereas outgassing of water molecule from a nanopore may take several hours. However, the presence of significant fast motions limits the time step in numerical integration to about one femto second. While this may become feasible in the near future, the nanosecond time scale for heat and flow system comprising several tens of thousands of atoms is the current time scale of standard MD simulations. The limit also exists in increasing the size of the simulation domain. It is not only the computational power but also the memory size that limits the length scale of the simulation. Many alternative strategies and extensions of MD, like wall potentials, are being explored to study larger length scale simulations.

1.2 Research objective and thesis outline

The main goal of this thesis is to investigate outgassing of water molecules from silicon/silica nanopores. Therefore, we will develop techniques for Molecular Dynamics that can simulate heat transfer and rarefied gas flows in a sub micro scale system. MD is a method which should be able to simulate the processes in a high Knudsen regime as well as in a low Knudsen regime. However, MD has been more widely used for the simulation of liquids^[9] and solids^[30] than for the simulation of gas. The system size was mostly limited to a size below $10nm$ scale.

This study will focus on MD techniques for simulating rarefied gas at a larger scale ($50nm \sim 1000nm$) without losing its advantages. The chosen procedure for achieving this goal is to develop numerical methods that speed up the Molecular Dynamics (MD) method, like parallelization, inclusion of wall potential models, and new methods to model the molecules. These methods are implemented in the MD simulation code PumMa^[2]. Additional studies, like inclusion of complex geometry for wall models, pressure calculation methods, and density controller, have been carried out as well.

Firstly, the standard numerical techniques used in the analysis, Molecular Dynamics (MD), Reactive Force Field (ReaxFF) molecular dynamics^[37], and Direct Simulation Monte Carlo (DSMC), are explained in Chapter 2. Molecular Dynamics techniques for heat transfer and mass flow are introduced in this chapter.

Chapters 3 and 4 deal with nanochannel flow simulations. A nanochannel is the most basic geometry of all MEMS and NEMS devices. A Poiseuille-like gas flow in a nanochannel with different geometries is analyzed here. Circular, rectangular and slit channels are considered, and their effects on heat and mass transfer are studied and analyzed. Fully developed and developing flows are studied as well. Both isothermal and heat transfer situations are studied for the developing flow. The calculated velocity slip and temperature distribution are compared with the results from Direct Simulation Monte Carlo (DSMC) simulations, and the similarities and differences are discussed.

In Chapter 5, the flexible 3 point water models are described. To develop

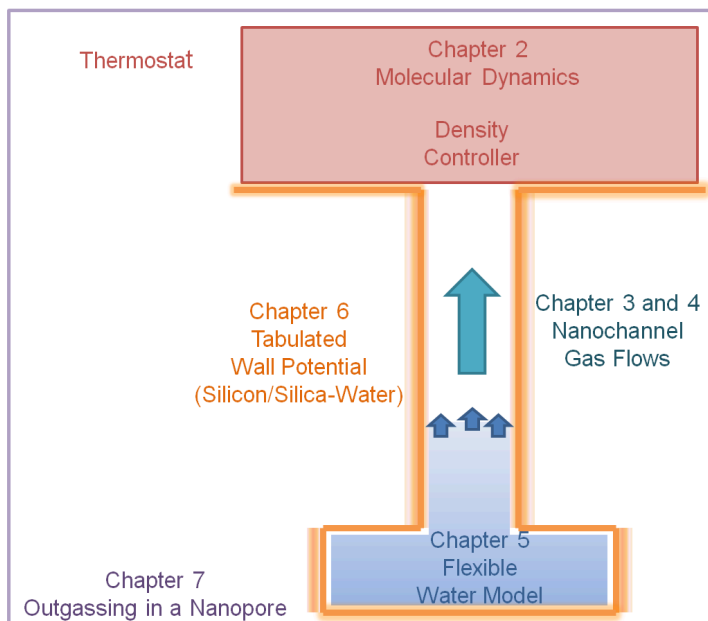


Figure 1.1: Schematic overview of the outgassing process in a nanopore and its relation to the topics studied in the chapters of this thesis.

a suitable water model for PumMa MD, a set of MD simulations of a modified TIP3P model and a ReaxFF based tabulated water model have been performed. The characteristic liquid density, self-diffusion coefficients, and radial distribution functions are determined and compared to experimental data.

In Chapter 6, a new implicit wall potential model representing silicon and silica walls is developed by tabulating the ReaxFF potential between bulk silicon/silica wall molecules and a water molecule. Contact angle simulations are performed in order to validate the outcomes.

In Chapter 7, simulations on outgassing in a nano pore will be described, representing water outgassing from complicated nano systems (cracks, NEMS devices, etc.) In this chapter, the findings from the previous chapters are combined (Figure 1.1). Four major factors (temperature, pressure, geometry, and surface interaction) are studied to find the most important factors in the early and end stages of the outgassing process.

Finally in Chapter 8, the conclusions of the thesis are summarized, and recommendations for further research are addressed.

2

Simulation methods for flow and heat transfer in micro- and nanosystems

The small length scales in micro- and nanosystems (high Knudsen number) cause the Navier-Stokes equations to break down, making the CFD solution invalid in some areas. For such conditions, particle based methods, such as Direct Simulation Monte Carlo (DSMC) and Molecular Dynamics (MD) are preferred. These particle based methods, mainly focusing on MD, will be explained in this chapter. Reactive empirical force field (ReaxFF) will also be explained in this chapter as an additional technique.

2.1 Introduction

Flows in nanochannels and nanopores, are to be solved numerically. For most flow problems, Computation Fluid Dynamics (CFD) is the standard way to solve them. However, it is known that, if the Knudsen number is too high, the small length scales in micro- and specially nanosystems cause the Navier-Stokes equation to break down, making the CFD solution invalid in some areas^[65]. Low Reynolds and high Knudsen number is a typical condition of a micro- and nanofluid. For such conditions, other solution methods exist that are more suitable, such as Direct Simulation Monte Carlo (DSMC) and Molecular Dynamics (MD).

Gas-surface interaction is very important for the proper description of heat transfer and flow at high Knudsen numbers, e.g. in micro- and nanochannels, or at low pressures. Reliable techniques needed to model gas-surface interactions will be discussed in this chapter. Controllers are also very important features of flow simulations. Temperature, density, and pressure controllers will be explained together with numerical measurement techniques.

Along with the explanations on Molecular Dynamics method, special attention will be paid to DSMC and ReaxFF methods, which will be used together with MD in this research.

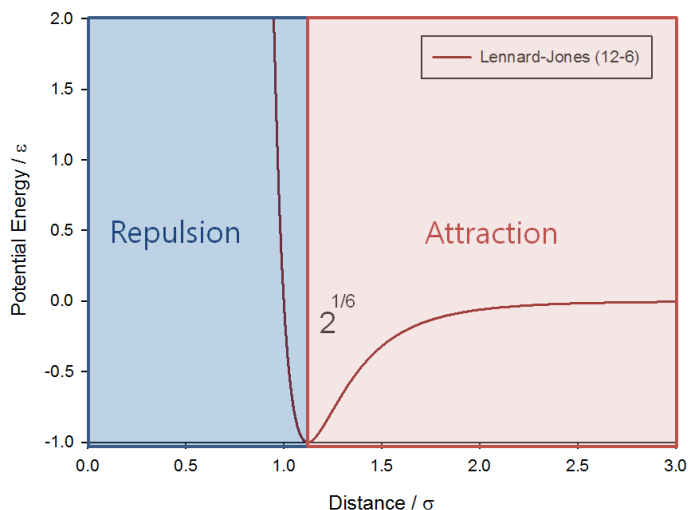


Figure 2.1: The Lennard-Jones potential.

2.2 Molecular Dynamics

2.2.1 Introduction to MD

Molecular dynamics is a statistical ensemble based model to study systems from a molecular point of view. In this method, atoms are considered as point masses, and they interact with each other through some intermolecular potential. Unfortunately, there is no universal definition for the inter-atomic interaction. So we use a number of approximate potentials or force fields (e.g. hard sphere, soft sphere, etc.). Among those potentials, Lennard-Jones potential^[98] (Figure 2.1) is one of the most used potentials, and it is also used in our PumMa Molecular Dynamics package^[2] for the simulations with argon molecules.

In Figure 2.2, typical steps for an MD method are described by a flow chart. The following five steps are main elements of the MD method:

1. *Input data.*

In order to be able to start an MD simulation, a set of input data is needed. This set includes input data for the simulation, such as the number of iteration steps (IT) to be performed, time step Δt . Furthermore force field parameters and topologies for different types of molecules in the system are required. Finally, the geometry of the system is needed to be described by boundary conditions.

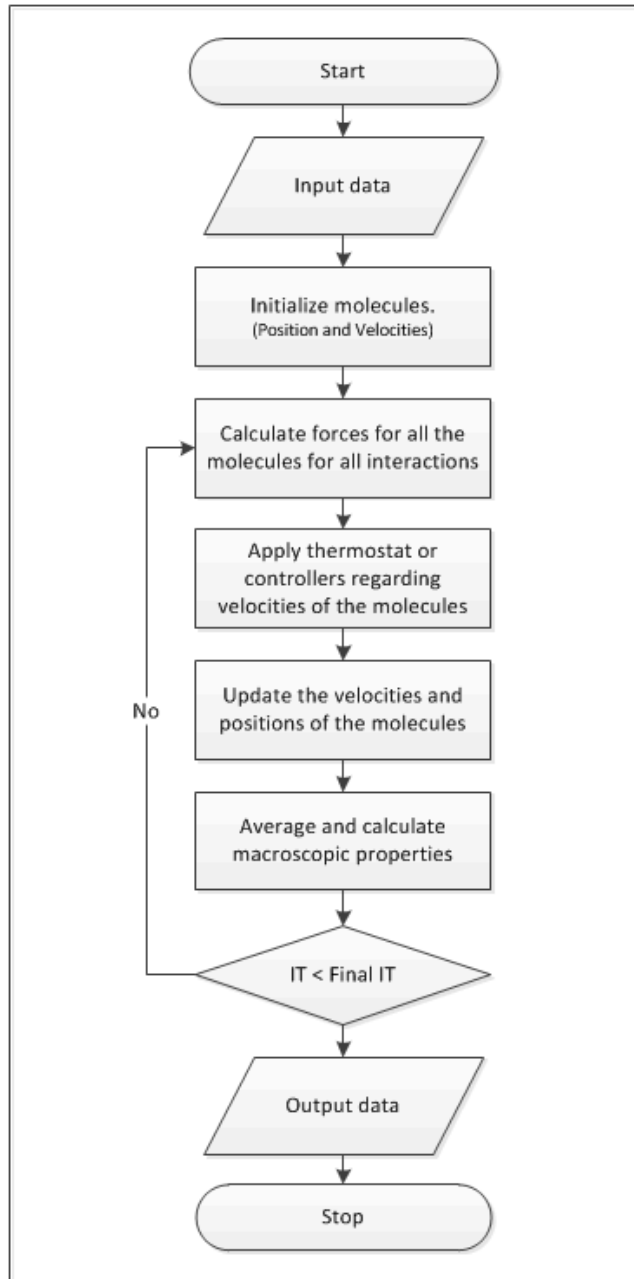


Figure 2.2: Flow chart for an MD method.

2. *Computation of the forces for all particles for all interactions.*

In the molecular simulation model, the particles (molecules or atoms) are modelled separately and they interact with each other by interaction potentials. They experience attractive and repulsive forces according to the distance r between them. The Lennard-Jones potential $\mathcal{U}(r_{ij})$ is defined by

$$\mathcal{U}(r_{ij}) = 4\epsilon \left(\left(\frac{\sigma}{r_{ij}} \right)^{12} - \left(\frac{\sigma}{r_{ij}} \right)^6 \right). \quad (2.1)$$

In this equation, r_{ij} is the distance between two particles. The Lennard-Jones potential parameter ϵ represents the energy well depth, and σ is a measure of the molecular diameter of the particles. In MD, the particles (or atoms) obey Newton's law of motion. The net force, F_i acting on any particle can be calculated as the spatial gradient of global potential acting on a molecule.

$$F_i = \sum_{j=1, j \neq i}^N \nabla \mathcal{U}_{ij} \quad (2.2)$$

3. *Apply the thermostat or controllers regarding velocities of the molecules.*

Flow controllers and temperature controllers are controllers regarding velocities of the molecules. Detailed information about the controllers that are implemented in PumMa will be discussed later in this chapter.

4. *Update the velocities and positions of the particles in time Δt .*

The particle positions and velocities are updated at every iteration step during an MD simulation. There is a number of algorithms available today to implement this scheme; the velocity Verlet^[167] is one of the commonly used algorithms.

$$v_i(t + \frac{1}{2}\Delta t) = v_i(t - \frac{1}{2}\Delta) + \Delta t [F_i(r_i(t))/m_i] \quad (2.3)$$

$$r_i(t + \Delta t) = r_i(t) + \Delta v_i(t + \frac{1}{2}\Delta) \quad (2.4)$$

The time step in MD is usually in the order of femto seconds ($1 \text{ fs} = 10^{-15} \text{ s}$). Such small time steps are needed to resolve the atomic vibrations having frequencies in the order of 10^{12} s^{-1} ^[111].

5. Calculation of macroscopic properties.

Calculation of macroscopic properties such as flow velocity, pressure, density and temperature are carried out in the last part of the MD simulation. Detailed numerical methods to calculate such properties will be discussed later in this chapter.

As can be seen in Figure 2.1, the interaction potential falls off very rapidly when the separation distance, r_{ij} , between two particles increases. To reduce the computational time of the simulation, the potential function is often truncated by a cutoff distance, r_c . This simple truncation of the potential creates a new problem though: whenever a particle pair crosses the cutoff distance, the energy makes a little jump. A large number of these events is likely to spoil energy conservation in a simulation. To avoid this problem, the potential is often shifted in order to vanish at the cutoff radius, r_c . The Lennard Jones equation (Equation 2.1) can be changed as follows:

$$\mathcal{U}(r_{ij}) = 4\epsilon \left(\left(\left(\frac{\sigma}{r_{ij}} \right)^{12} - \left(\frac{\sigma}{r_{ij}} \right)^6 \right) - \left(\left(\frac{\sigma}{r_c} \right)^{12} - \left(\frac{\sigma}{r_c} \right)^6 \right) \right) \quad (2.5)$$

This equation is only valid for $r < r_c$. The potential is set to zero when the intermolecular distance $r > r_c$.

If molecules are separated by distances greater than the cutoff-distance r_c , the program skips to the end of the inner loop, avoiding expensive calculations, and considers the next neighbour. In this method, the time to examine all pair separations is proportional to N^2 . Verlet^[167] suggested a technique for further improving the speed of a program by maintaining a list of neighbours of a particular molecule, which is only updated at specific intervals. Between the updates of the neighbour list, only the j molecules are checked. The number of pair separations explicitly considered is reduced. This saves time in looping through j , calculating distances between the particles, and checking against the cutoff, for all particles.

2.2.2 PumMa Molecular Dynamics

The PumMa Molecular Dynamics package has been developed by several people in the Computational Biology group of the Department of Biomedical Engineering at the Eindhoven University of Technology^[2].

Most of the simulations conducted with MD have applications in the field of biology and chemistry. PumMa has been also used to study applications in the field of biology, such as the forming of membranes^[145], the fusion^[145] and fission of vesicles^[110].

In recent years, with the newly developed features that are useful to study nanoflow and heat transfer (controller, boundary conditions, etc), PumMa has been used for researches in the area of nanoflows and heat transfer^[91,118,163].

The main advantage of PumMa compared to other open source MD packages is the full access of the source code. Other MD packages do not allow full access

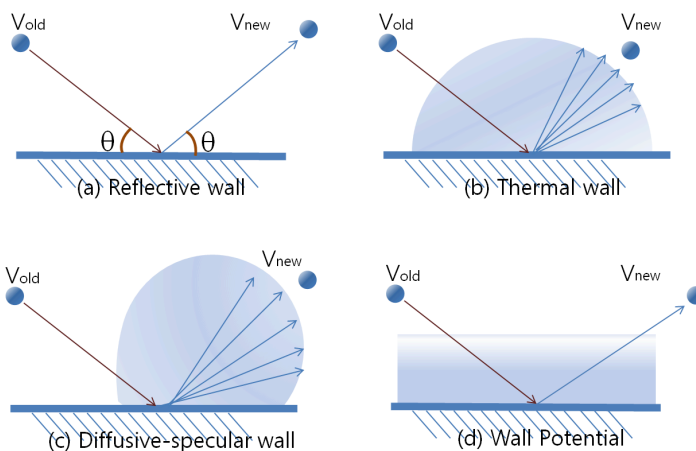


Figure 2.3: Implicit wall models.

of source code to the very low level. This allows easier implementation of new features to the existing MD code. Therefore we choose to use this MD package in our research.

2.2.3 Boundary conditions

In Molecular Dynamics simulations, the most common way to model the wall is to include all wall molecules in the simulation. This method is named the explicit wall boundary condition. The atoms in a solid are arranged in a lattice of minimal energy. In the explicit wall model, the wall particles attract the fluid particles, so it can be used to model two-phase systems. The explicit wall model is very detailed, but the drawback is that it is computationally costly: most of the calculation time is spent on the wall particles, which is not often the area of interest in nanoflows and heat transfer^[118,119,163].

Due to this drawback, implicit wall models are often used in particle-based methods. In this section, the most important implicit wall models are shortly presented (Figure 2.3).

- Reflective wall model
- Thermal wall model
- Diffusive-specular wall model
- Wall potential

For all four implicit wall models, a particle with velocity $v_{old} = (v_{old,x}, v_{old,y}, v_{old,z})$ and mass m , is interacting with a wall with temperature T_w . The wall

model should give a new particle velocity, $v_{new} = (v_{new,x}, v_{new,y}, v_{new,z})$ after the interaction (Figure 2.3).

Reflective wall boundary condition

If a particle reaches a reflective (or specular) wall, its velocity component normal to that wall, v_x , is reversed: the new velocity of the particle v_{new} is given as:

$$v_{new} = (-v_{old,x}, v_{old,y}, v_{old,z}). \quad (2.6)$$

Here the x -direction is normal to the wall. In this way, the energy of the particle is conserved. Therefore, the temperature of the wall has no influence on the particle since the magnitude of the velocity is not altered by the collision. The reflective wall is very easy to implement, and has the numerical advantage that the energy in the system remains constant. However, the disadvantage is that energy exchange between wall and particle is impossible. So it is impossible to use a reflective wall to model heat exchange between a gas and a microchannel wall. Also, there is no attraction between particles and the wall, so in a liquid-gas mixture, the liquid will not be attracted to the reflective wall. For this reason, the reflective wall should not be used in problems where the wall properties are important, such as the evaporation region close to a wall.

Thermal wall boundary condition

In a thermal wall, a particle that collides with the wall is assumed to have so many interactions with the wall, that the outgoing velocity is completely determined by the wall temperature T_w . This means that the new velocity v_{new} after the collision is drawn from a velocity distribution of an ideal gas particle that passes through a plane^[58],

$$f(v_{new}) = f_x(v_{new,x})f_y(v_{new,y})f_z(v_{new,z}) \quad (2.7)$$

where the velocity component normal to the wall has a Rayleigh distribution and the components parallel to the wall have a Maxwell distribution:

$$f_x(v_x) = \frac{mv_x}{k_B T_w} \exp\left(-\frac{mv_x^2}{2k_B T_w}\right), \quad (2.8a)$$

$$f_y(v_y) = \sqrt{\frac{m}{2\pi k_B T_w}} \exp\left(-\frac{mv_y^2}{2k_B T_w}\right), \quad (2.8b)$$

$$f_z(v_z) = \sqrt{\frac{m}{2\pi k_B T_w}} \exp\left(-\frac{mv_z^2}{2k_B T_w}\right), \quad (2.8c)$$

where the x -direction is normal to the wall. In this way, the particles after the collision have been completely accommodated to the wall temperature T_w . The old velocity v_{old} is not used, so the particle loses all information about its state before the collision. Similar to the reflective wall model, the thermal wall model

also ignores the attraction between a fluid particle and the wall, so in situations where this is important, the thermal wall should not be used.

Diffusive-specular wall boundary condition

A Maxwell-type boundary condition, also known as a diffusive-specular wall condition^[119,177], is the last implicit wall model introduced in this study. This is based on the assumption that a fraction $(1.0 - \alpha)$ of molecule is reflected specular from the surface and α is re-emitted diffusively with Maxwell distribution at wall condition. When an accommodation coefficient $\alpha = 1.0$, the boundary condition is fully diffusive.

The diffusive-specular wall model is computationally easy to use, and it has the advantage over the reflective wall model that the temperature of the particles partly accommodates to the wall temperature. The main advantage over the thermal wall model is that the accommodation rate can be specified in the form of an accommodation coefficient α . As a disadvantage, the accommodation coefficient α is not always known a priori, and depends on the temperature and materials. Because the diffusive-specular method is a combination between the reflective wall and the thermal wall, the diffusive-specular model is also not applicable in situations where the attraction between fluid and wall is important.

Wall potential boundary condition

A major drawback of the above models is that they do not carry any information of the underlying configuration of the solid wall. They also neglect the gas-surface force interaction effects which can be significant in nano-channel flows. Therefore, no distinction can be made between a hydrophilic and hydrophobic wall. To be able to include such information, the boundary condition has to be derived from the solid's point of view. In his pioneering work Lennard-Jones derived such relations for several types of crystals^[98]. Subsequently, Hove^[74] and Steele^[151] used these relations to derive potentials which describe the interaction between a gas molecule and a solid wall. Crucial in these derivations are the lattice sums using Fourier series to arrive at the proposed potential. Based on this work, Abraham^[6] proposed four types of wall potentials: the Lennard-Jones wall as given by Steele, the Lennard-Jones (10-4) wall, a Boltzmann weighted wall and a reflective wall. Both the Steele and 10-4 wall potential have been used extensively over the years. For instance, the Steele's potential has been used in studies of the solvent forces of dense fluids or the dynamics of liquid filled pores and the 10-4 potential has been used in work on the solid-fluid interface, the flow in micropores, or in work on the velocity auto-correlation function of confined fluids^[22,94,158]. The Steele's potential and 10-4 potential have the following forms:

$$U_{Steele}(z) = 2\pi\rho_s\sigma^2\epsilon\Delta \left[\frac{2}{5} \left(\frac{\sigma}{z}\right)^{10} - \left(\frac{\sigma}{z}\right)^4 - \frac{\sigma^4}{3\Delta(z + 0.61\Delta)^3} \right], \quad (2.9)$$

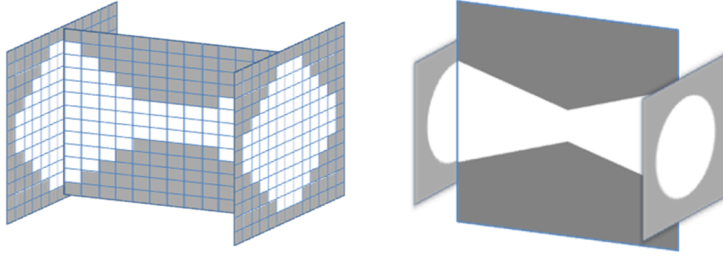


Figure 2.4: Grid model (left) and new mathematical function model(right)

$$\mathcal{U}_{10-4}(z) = 2\pi\rho_s\sigma^2\epsilon\Delta \left[\frac{2}{5} \left(\frac{\sigma}{z} \right)^{10} - \left(\frac{\sigma}{z} \right)^4 \right], \quad (2.10)$$

where σ and ϵ are the Lennard-Jones length and energy parameters for the interaction of fluid molecule with a single constituent particle of the solid, and z is the perpendicular distance between the fluid molecule and the wall surface. ρ_s is the number density of the solid wall surface. Δ is the spacing between basal planes. Lorentz-Berthelot mixing rules are often used for building the base interatomic potential function for wall potential^[143]. Lorentz-Berthelot mixing rules have the following forms:

$$\epsilon_{A-B} = \sqrt{\epsilon_A\epsilon_B}, \quad (2.11a)$$

$$\sigma_{A-B} = \frac{\sigma_A + \sigma_B}{2}. \quad (2.11b)$$

Although, Lorentz-Berthelot mixing rules are widely used because of its simplicity and the lack of a clear superior mixing rule^[179], it does not always give realistic values to all situations^[46].

Geometry of implicit walls

In the PumMa MD code, additional work is done to add different geometries to the implicit wall models. So far, most of the MD simulation codes have wall models that built its shape using grids(Figure 2.4, left). Each boundary condition for each grid is inputted manually. The disadvantage of this method is that you have to draw curved three dimensional objects. To solve this problem, implicit wall models (Figure 2.4, right) are described in mathematical functions (circular, linear, polynomial functions) rather than being described by a large number of grids. The Newton-Raphson method^[34] is used to calculate the collision point and collision time of a mathematical wall and a particle. The gradient of the mathematical function at the collision point is used to approximate the geometry locally as a flat wall (Figure 2.5, right). Figure 2.6 shows a snapshot of particles in a nanochannel flow. Boundary conditions of the nanochannel are given as simple sinusoidal functions in order to simulate the roughness effect on the gas flow.

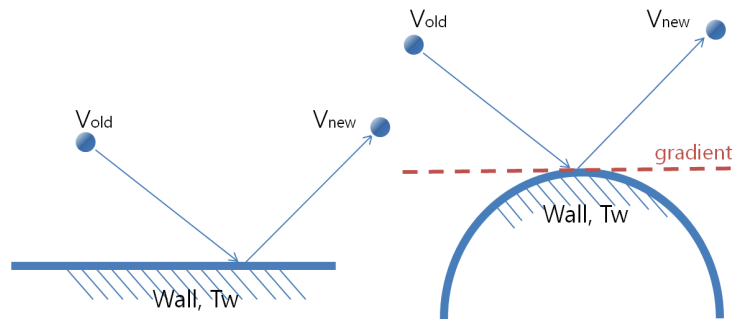


Figure 2.5: The standard configuration used in the wall models discussed here: flat wall(left) and curved wall(right).

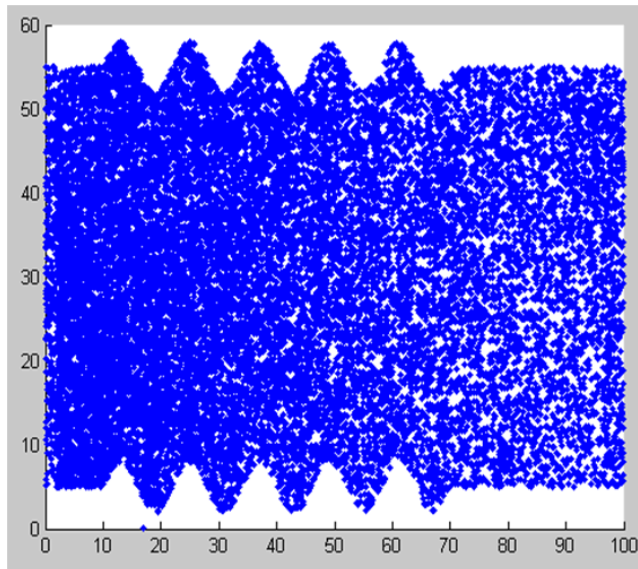


Figure 2.6: Snapshot of particles in a nanochannel described by sinusoidal functions and constant values.

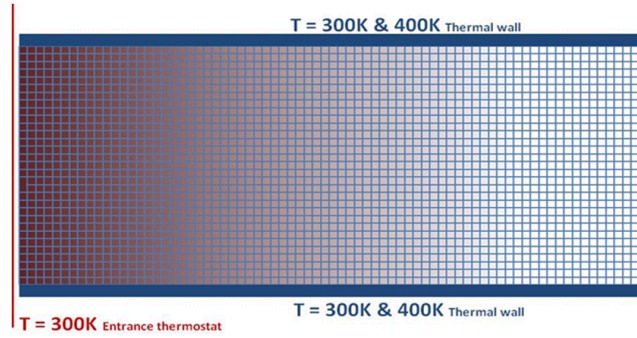


Figure 2.7: A system sliced into a large number of rectangular bins in the direction normal to the walls to calculate macroscopic properties.

2.2.4 Macroscopic properties

A binning technique is used to calculate the velocity, pressure, density and temperature contours. Therefore, the simulation box in the direction normal to the wall is sliced into a number of rectangular bins (parallel to the walls) as shown in Figure 2.7. For each bin the local streaming velocity is calculated.

For rarefied gas simulation, time averaging becomes more important due to the small number of molecules inside a sampling bin, and a longer time averaging is needed for an accurate solution. To store the data in an efficient way, PumMa internally calculates the average properties for each bin. The macroscopic properties are computed as follows.

Density

Calculating density from MD simulation is quite straight forward. In this study, the density ρ_b in each bin is:

$$\rho_b = m \cdot n_b. \quad (2.12)$$

where m is the atomic mass and n_b is the number density in a bin.

$$n_b = \frac{N_b}{V_b}. \quad (2.13)$$

N_b is the number of atoms inside the bin, and V_b is the control volume of the bin.

Velocity

For each bin the local streaming velocity is calculated by using the below equation, where m_i and v_i are the mass velocity of atom i inside the bin:

$$v_b = \frac{\sum_{i=1}^{N_b} m_i v_i}{\sum_{i=1}^{N_b} m_i}. \quad (2.14)$$

Temperature

For a static situation, the temperature T is calculated directly from the kinetic energy or velocity of atoms. The kinetic energy inside a bin, KE_b , can be written in terms of the velocity v_i of the particles as follows:

$$KE_b = \frac{\sum_{i=1}^{N_b} m_i v_i^2}{2}. \quad (2.15)$$

From the kinetic theory, the kinetic energy can also be written in terms of the temperature, T as follows:

$$KE = \frac{3}{2} N k_B T \quad (2.16)$$

where k_B is the Boltzmann constant. Combining Equation 2.15 and Equation 2.16, an expression for the temperature of a bin is obtained:

$$T_b = \frac{1}{3N_b k_B} \sum_{i=1}^{N_b} m_i v_i^2. \quad (2.17)$$

However, in order to calculate the temperature in a flow, the average velocity of each bin, v_b needs to be calculated first. Peculiar velocity of each particle, computed based on the average velocity of each bin, is then used to calculate the temperature of the bin:

$$T_b = \frac{1}{3N_b k_B} \langle \sum_{i=1}^{N_b} m_i (v_i - v_b)^2 \rangle. \quad (2.18)$$

Pressure

Local pressure is important in analysing micromechanical behaviour. The local pressure in the DSMC method may be evaluated from the ideal gas law (Equation 2.19) or by explicitly evaluating the pressure tensor for calculating the pressure near the wall:

$$P_{idealgas} = \frac{1}{V} \langle \sum_i^N m_i (v_k^i - v_k^{avg})(v_l^i - v_l^{avg}) \rangle. \quad (2.19)$$

The ideal-gas law is known to fail as the pressure increases. Next to the ideal-gas law, MD simulations can also predict a pressure by using the Irving-Kirkwood method^[76]. The Irving-Kirkwood method manages to predict the pressure with less than 10% difference from experimental results even for the liquid state, while the ideal-gas law gives an error larger than 100% near the liquid state^[14]. According to the Irving Kirkwood method the contribution of each particle to the pressure tensor consists of two parts, a kinetic part and a configuration part:

$$P_{kl} = \frac{1}{V} \langle \sum_{i=1}^N m_i (v_k^i - v_k^{avg})(v_l^i - v_l^{avg}) - W_{kl} \rangle \quad (2.20)$$

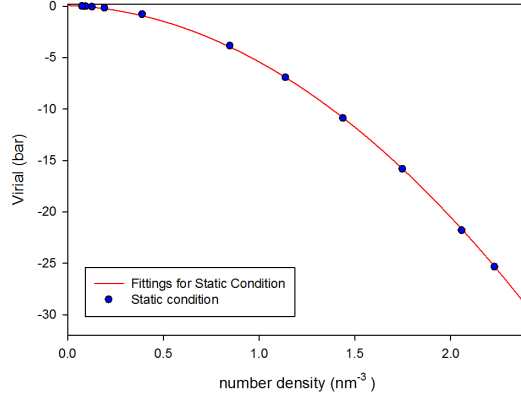


Figure 2.8: Virial component of the pressure as function of number density at $T = 121K$.

$$W_{kl} = \frac{1}{2} \sum_{i=1}^N \sum_{j=1, j \neq i}^N (r_k^j - r_k^i) f_l^{i,j} \quad (2.21)$$

where the first term on the right-hand side of Equation 2.20 represents the kinetic component and the term W_{kl} represents the virial component. In the kinetic part, m_i is the atomic mass of particle i , whereas subscripts k and l are the axes of the Cartesian coordinate system, v_k^i and v_l^i are the velocity component of particle i in the k and l directions, and v_k^{avg} and v_l^{avg} are the local average streaming velocities at the position of particle i , in the k and l directions, respectively. The term W_{kl} in Equation 2.21 is the k th component of the distance vector between particles i and j , and is the l th component of the intermolecular force exerted on particle i by particle j . The first term, $\frac{1}{V} \langle \sum_{i=1}^N m_i (v_k^i - v_k^{avg})(v_l^i - v_l^{avg}) \rangle$, in the Irving-Kirkwood expression is related to the ideal-gas law. It calculates the ideal gas pressure by considering the momentum resulting from the particle velocities. The second term, W_{kl} , corresponds to the virial component which corrects the ideal-gas law because of the interaction of particles with non-zero volumes and force field.

To validate our code regarding the Irving-Kirkwood method, argon gas is simulated in a static (no-flow) condition. Figure 2.8 shows the virial component for static situations. The 2nd order polynomial function was fitted through the data using Origin 8.5 Software^[4]:

$$W_{static} = 0.080 - 17.499n - 3108.418n^2 [bar] \quad (2.22)$$

where W_{static} is a virial component in the static(no-flow) condition, and n is a number density of the gas. Since the virial equation of state^[173] has a form of:

$$P_{static} = k_B T n - B_2(T) k_B T n^2, \quad (2.23)$$

Table 2.1: Comparison between Irving-Kirkwood method and the second virial coefficient at 121K. Coefficient C_2 in Equation 2.24 is compared.

My simulation	-3108.418 [$\sigma^6 bar$]
Experimental Results ^[99]	-3111.896 [$\sigma^6 bar$]
MD simulation by Leonhard ^[99]	-2972.592 [$\sigma^6 bar$]
MD simulation by Hloucha ^[72]	-3222.866 [$\sigma^6 bar$]

for certain temperature, virial expansion can be shown to be in the form of:

$$P_{static} = C_1 n - C_2 n^2 [bar] \quad (2.24)$$

where $C_1 = k_B T$ and $C_2 = B_2(T) k_B T$.

$B_2(T)$ is the second virial coefficient. Virial coefficients B_i appear as coefficients in the virial expansion of the pressure of a many-particle system in powers of the density, providing systematic corrections to the ideal gas law. They are characteristic for the interaction potential between the particles and in general depend on the temperature. The second virial coefficient B_2 depends only on the pair interaction between the particles^[71].

In Table 2.1, C_2 values are compared with other literature values^[72,99]. Our simulation results for static situation perfectly match with the literature values. This result validates our MD code and the use of the Irving-Kirkwood method.

2.2.5 Controllers

For micro heat transfer and flow, it is important to have local temperature and pressure controllers for specific zones. In order to control the temperature and density of specific zones, local temperature controller and density controller have been implemented in PumMa MD .

Temperature controller (thermostat)

An MD simulation generates positions and velocities of the molecules in the system for every time step. A collection of these positions and velocities is called a microstate. A collection of microstates that represents the same macrostate is called an ensemble.

The standard MD is performed in the microcanonical (NVE) ensemble, that means the number of particle (N), the volume of the system (V), and the total energy (E) are constant. However, the microcanonical ensemble does not correspond to the conditions under which most experiments are carried out. If one is interested in the behavior of the system at a specific temperature, an NVT simulation using a thermostat is required. For an NVT simulation, the total energy (E) is not specified, but the temperature is kept constant. This may be achieved by coupling with a thermostat.

An obvious way to alter the temperature of the system is velocity scaling. If the temperature at time t is $T(t)$, the simplest way to control the temperature is to multiply the velocities at each time step by a factor λ_{therm} ($v_{new} = \lambda_{therm}v_{old}$):

$$\lambda_{therm} = \sqrt{T_0/T(t)}. \quad (2.25)$$

$T(t)$ is the current temperature as calculated from the kinetic energy and T_0 is the desired temperature. A weaker formulation of this approach is the Berendsen thermostat^[18], which is the thermostat used in PUMMA MD. To maintain the temperature the system is coupled to a heat bath with fixed temperature T_0 . The velocities are scaled at each step, such that the rate of change of temperature is proportional to the difference in temperature:

$$\frac{dT(t)}{dt} = \frac{1}{\tau}(T_0 - T(t)) \quad (2.26)$$

where τ is the coupling parameter which determines how tightly the bath and the system are coupled together. This method gives an exponential decay of the system towards the desired temperature. The change in temperature between successive time steps is:

$$\Delta T = \frac{\Delta t}{\tau}(T_0 - T(t)) \quad (2.27)$$

Thus, the scaling factor for the velocities is:

$$\lambda_{therm} = \sqrt{1 + \frac{\Delta t}{\tau} \left(\frac{T_0}{T(t - \frac{\Delta t}{2})} - 1 \right)} \quad (2.28)$$

and is due to the fact that the called leap-frog algorithm^[144] is used for the time integration. In practice, τ is used as an empirical parameter to adjust the strength of the coupling. Its value has to be chosen with care. In the limit $\tau \rightarrow \infty$ the Berendsen thermostat is inactive and the run is sampling a microcanonical ensemble. The temperature fluctuations will grow until they reach the appropriate value of a microcanonical ensemble. However, they will never reach the appropriate value for a canonical ensemble. On the other hand, too small values of τ will cause unrealistically low temperature fluctuations.

Density controller

The density is controlled within an arbitrary controller zone by inserting molecules and deleting molecules such that the correct number density is enforced. At time t , a controller computes the number of molecules that needs to be inserted or to be deleted. Following steps are then carried out:

Inserting molecules

1. Search for an insertion site, r_i , that ensures non overlapping molecules. A site to insert a molecule is accepted if no molecule is present within the cutoff distance of the inserted molecule. If it is rejected, a new site will be tried with a random function. This can be done in one trial or in multiple trials. The site can be easily found when the system has a low density.
2. Create a molecule at r_i , and give an initial velocity v_i , which is sampled randomly from a Maxwell-Boltzmann distribution at the required temperature.

Deleting molecules

1. Initially, select a random candidate molecule i from the controller zone.
2. Delete molecule i from the controller zone.

Our controller is developed for rarefied gas simulations. It is necessary to include an iterative search algorithm of potential energy landscape in order to be used in liquid simulation. Density controllers for liquid simulation is described in the study of Borg et al.^[23].

Pressure controller

Ideal gas law ($P = nk_B T$) holds for gas simulations, and local pressure controller is built by combining a local density controller and temperature controller together. The objective density of the density controller is calculated by ideal gas law and temperature of the control zone.

Flow controller

Two types of flow controller are used in the PumMa MD package. Most obvious controller is created by using two pressure controllers placed at the inlet and outlet of the channel. The flow is enforced by the pressure difference over the inlet and the outlet. Another type is the gravity fed method. A same amount of acceleration is given to the particles for each time step. Due to its simplicity, this method is often preferred for liquid flows^[102], where it can replace the flow controlled by pressure controller. This gravity-fed method can be also divided into two types according to the domain where the gravity-like field is applied. The gravity-like field can be applied to the whole system or it can be applied to a buffer region which acts like a pump of the nanofluidic system^[102].

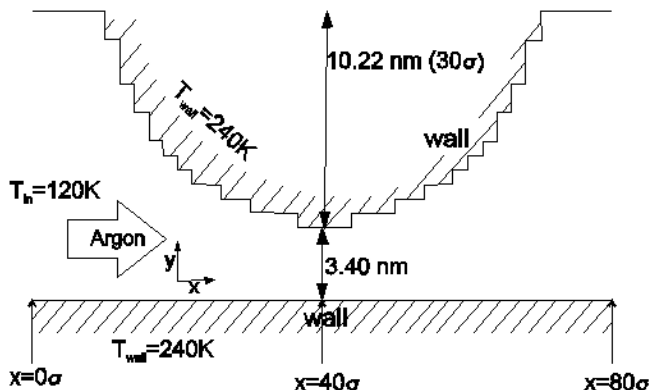


Figure 2.9: Test simulation for parallelization (van den Akker 2010^[162]).

Table 2.2: Execution times of the test simulation.

Number of processors	1	2	4
Execution time for 500,000 iterations (sec)	5670	3109	2949

2.2.6 Parallelization of the computations

For speeding up the MD simulation, the code was parallelized. The starting point is parallelization of an existing molecular dynamics code (based on PumMa) developed by van den Akker (2010)^[162,164]. The existing PumMa MD code for heat transfer and flow has been developed in sequential mode alone. Parallelization of the code has been carried out by parallel computation of interaction between the particles. The computation work load has been divided to the processors by spatially partitioning the system domain. The information of each domain is then shared after each iteration step. This work has been tested with 20581 argon particles, channel geometry, and given conditions shown in Figure 2.9.

In this test simulation, a gravity fed flow of an argon gas meets an obstacle with lower temperature. The walls have a temperature of 240K with a thermal wall boundary condition, while the gas enters the simulation at 120K. It is seen as a gas that is cooling a device. Initially, the gas temperature is set to 120K and equal pressure holds in the whole domain. In general, the execution time for multi processor simulations is known to show an inverse characteristic function^[127].

However, in the test simulation, an execution time for 4 processors is not following the characteristic function (Table 2.2). It is higher than expected. This is due to an uneven distribution of particles throughout the domain caused by the boundary conditions. The uneven distribution is caused by the temperature difference along the domain. Temperature of the gas is higher in the right side of the channel due to heating by the high temperature obstacle, and density

Table 2.3: Execution times (sec) of the test simulation for different iteration periods. The numbers in parentheses indicate the performance factor based on the performance of single processor execution.

Iteration Period	Number of Processors	1	2	4
0 to 10,000		90	41(2.2)	28(3.2)
10,000 to 20,000		101	41(2.2)	28(3.0)
20,000 to 30,000		107	41(1.9)	28(2.3)
30,000 to 40,000		112	41(1.8)	28(2.2)
40,000 to 50,000		114	41(1.7)	28(2.0)
50,000 to 60,000		115	41(1.8)	28(2.0)

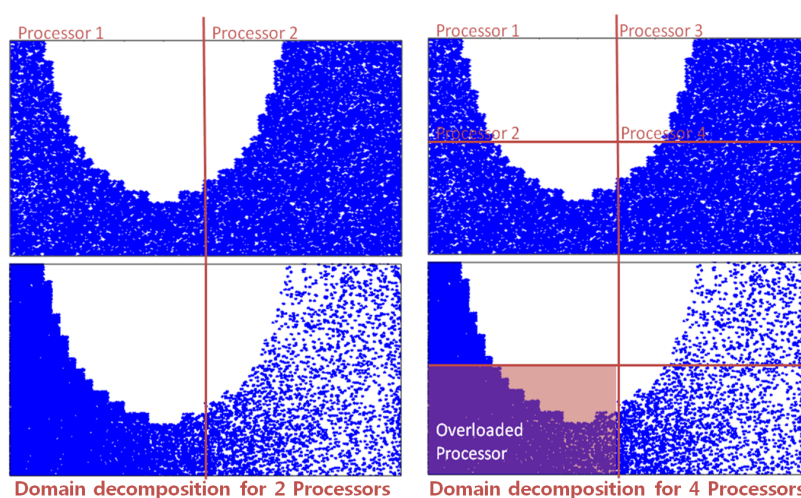


Figure 2.10: Particle distribution for an initial state (top) and after 500,000 iterations (bottom).

becomes lower at the right side compared to the left. In the initial state, the particles are more or less evenly distributed (Figure 2.10, top). In Table 2.3, the decline in the performance of the 4 processors is clearly shown for the higher iterations. In the higher iterations, particles are distributed more unevenly compared to the early states. In the test simulation with 4 processors (Figure 2.10, right), after 150,000 iterations, more than 50% of particles are decomposed on one specific processor alone and other processors have to wait for the overloaded processor to finish its task. Compared to the simulation with 2 processors (Figure 2.10, left), relative overloading of one specific processor is much higher in the simulation with 4 processors (Figure 2.10, right).

So far, most of the MD simulations based on PumMa have been working on homogeneous systems (system with uniform spatial density and negligible over time), thus static load balancer has been used. In our example, system is heterogeneous. Therefore, it is important to redesign the decomposition of

parallelization domains. Ideally, a dynamic repartitioning of the subdomains studied by Srinivasan et al.^[149], would be good method to maintain the acceptable load balance in MD simulation of flow and heat transfer.

2.3 ReaxFF

In this thesis, up-scaling techniques from more ab initio method to Molecular Dynamics will be investigated. ReaxFF method^[37] was used for the study. The ReaxFF method is an empirical force-field that allows fully reactive atomistic scale molecular dynamics simulations of chemical reactions. It allows to study more ab initio simulations compared to conventional Molecular Dynamics. In this method, the information about the reaction pathways are contained in the definition of the force fields itself. ReaxFF is a general purpose bond order dependent force field that provides accurate descriptions of bond breaking and bond formation. The main difference between non-reactive Molecular Dynamics and ReaxFF is that, in ReaxFF, the connectivity is determined by bond orders calculated from inter-atomic distances, which are updated at every MD time step. All the connected interactions are a function of the bond order. This allows for bonds to create and break dynamically during the simulation.

Non-bonded interactions such as van der Waals and Coulombic interactions are calculated between every pair of atoms, and the interactions due to bond formations (connected interactions) are introduced as perturbation terms depending on the bond order. All excessive close-range non-bonded interactions are avoided by the inclusion of shielding terms. Some of the main features of ReaxFF that makes this force field reactive are listed below.

- The bond order is calculated between every pair of atoms. The bond order defines the number of atomic orbitals involved in the formation of a chemical bond. Normally it takes values from 0 to 3. The strength of the bond is directly proportional to the bond order. The bond order is a function of distance between atoms. A fundamental difference between ReaxFF and most other force fields is that ReaxFF does not use fixed connectivity assignments for the chemical bonds. Instead the bond order, BO_{ij} , is calculated directly from the instantaneous interatomic distances r_{ij} as given in Equation 2.29.

$$\begin{aligned} BO_{ij} &= BO_{ij}^{\sigma} + BO_{ij}^{\pi} + BO_{ij}^{\pi\pi} \\ &= \exp\left[p_{bo1} \cdot \left(\frac{r_{ij}}{r_0^{\sigma}}\right)^{p_{bo2}}\right] + \exp\left[p_{bo3} \cdot \left(\frac{r_{ij}}{r_0^{\pi}}\right)^{p_{bo4}}\right] + \\ &\quad \exp\left[p_{bo5} \cdot \left(\frac{r_{ij}}{r_0^{\pi\pi}}\right)^{p_{bo6}}\right]. \end{aligned} \quad (2.29)$$

As the atoms come closer to each other, first the σ bond gets activated and the bond order starts to increase from 0 to 1, consequently reducing the bond energy between atoms. σ bonds are the strongest type of covalent

bonds due to the direct overlap of orbitals. At smaller separations π bonds get activated and eventually the double π bonds. π bonds are covalent chemical bonds where two lobes of one involved atomic orbital overlap two lobes of the other involved atomic orbital. π bonds are usually weaker than σ bonds. π bonds result from overlap of atomic orbitals that are in contact through two areas of overlap. π bonds are more diffuse bonds than the σ bonds. Thus the bond order takes any real value between 0 and 3 depending on the distance of separation and the type of atom pair.

- Every connected interaction (bond energy, valence angle energy etc.) are incorporated with the bond order, ensuring that its energy contributions disappear upon bond dissociation. When the atoms are sufficiently far apart from each other, energy contributions from chemical bonds terms go to zero upon dissociation.
- ReaxFF has no discontinuity in the potential energy surface. To avoid energy discontinuities when charged species move in and out of the non-bonded cut-off radius, ReaxFF employs a Taper correction term as developed by Vos Burchart^[44]. Each non-bonded energy and its derivative is multiplied by a Taper-term, which is taken from a distance dependent 7th order polynomial.

$$\begin{aligned} TAP &= TAP_7 \cdot r_{ij}^7 + TAP_6 \cdot r_{ij}^6 + TAP_5 \cdot r_{ij}^5 + TAP_4 \cdot r_{ij}^4 \\ &+ TAP_3 \cdot r_{ij}^3 + TAP_2 \cdot r_{ij}^2 + TAP_1 \cdot r_{ij}^1 + TAP_0. \end{aligned} \quad (2.30)$$

The terms in this polynomial are chosen to ensure that all 1st, 2nd and 3rd derivatives of the non-bonded interactions to the distance are continuous and go to zero at the cut-off boundary.

- Non-bonded interactions (van der Waals and Coulomb) are described between all atoms, irrespective of connectivity. A distance corrected Morse-potential is used to account for van der Waals interaction. By including a shielding term, excessive short-range repulsive/attractive nonbonded interactions are avoided; it is shielded at short range so that the Coulomb and van der Waals interactions become constant as $r_{ij} \rightarrow 0$ as shown in Figure 2.11.
- A shielded Coulombic potential is used to account for interaction between charged species. Atomic charges are calculated using the Electron Equilibrium Method (EEM)^[130]. EEM is a semi-empirical density-functional theory based method where atomic electronegativity and hardness are parameterized for the calculation of charge distribution in molecules^[116]. It allows calculation of geometry dependent charge distributions. Therefore,

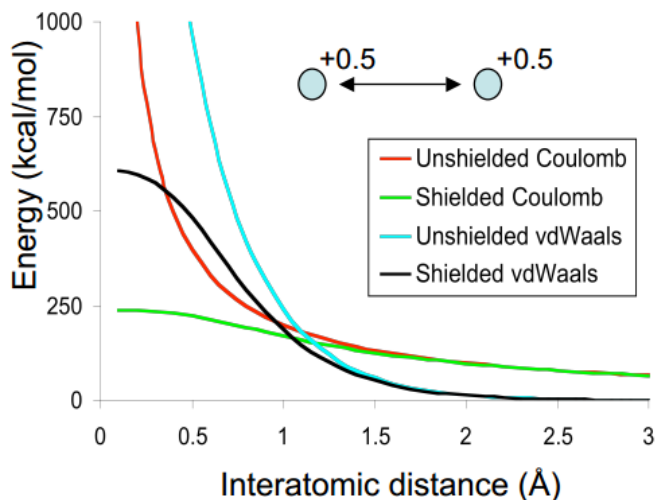


Figure 2.11: Non-bonded interactions with and without shielding^[37].

the charges are dynamically calculated upon bond breaking and formation.

The total potential energy in ReaxFF is a linear combination of various energy contributions as shown in Equation (2.31)^[37].

$$E_{\text{system}} = E_{\text{bond}} + E_{\text{lp}} + E_{\text{over}} + E_{\text{under}} + E_{\text{val}} + E_{\text{pen}} + E_{3\text{conj}} + E_{\text{tors}} + E_{4\text{conj}} + E_{\text{H-bond}} + E_{\text{vdWaaals}} + E_{\text{Coulomb}} \quad (2.31)$$

where E_{bond} represents the bond energy, E_{lp} is the energy due to the presence of lone pair, and E_{over} and E_{under} are the energies arising from over and under-coordination, of atoms with respect to their valency. The valence angle (three-body) energies are accounted for in the terms E_{val} and E_{tors} , respectively. E_{pen} is a penalty energy function to stabilize a three body system with the center atom having two double bonds connected to it. Conjugated chemical bonds are stabilized by adding corrections for three bodies, $E_{3\text{conj}}$, and four bodies, $E_{4\text{conj}}$, conjugation terms to the respective systems. $E_{\text{H-bond}}$ represents the hydrogen bond interactions. The long-range interactions such as van der Waals interactions, E_{vdWaaals} , and Coulombic interactions, E_{Coulomb} , are accounted for between every pair of atoms irrespective of the presence of chemical bonds^[80].

Different energy contributions are defined by various interaction potentials, and it is seen that every energy term in Equation (2.31) involves several parameters. All these parameters have to be optimised appropriately in order to reproduce a real physical system. Parameter optimisation of the force field is an important step before modelling any system. The parameters used in the

ReaxFF method are usually derived by fitting against a training set comprising both quantum mechanics and experimental data.

2.4 Direct Simulation Monte Carlo

Another popular particle-based technique, other than MD, often used for simulating the gaseous micro channel flows, is Direct Simulation Monte Carlo (DSMC). As mentioned earlier, DSMC is often preferred for gas flows as it is computationally faster than MD. DSMC is approximately linearly dependent on the number of particles^[62], while MD is approximately dependent on the square of the number of the particles.

The Direct Simulation Monte Carlo method has been first developed by G. Bird^[20]. It can be considered as a Monte Carlo approximation of the time-dependent non-linear Boltzmann equation^[168]. The Boltzmann equation describes the evolution of a dilute gas at the level of the single particle distribution function:

$$\frac{\partial f}{\partial t} + v \cdot \nabla = \Omega(f, f) \quad (2.32)$$

where f is the particle density and v is the particle velocity. $\Omega(f, f)$ is the collision integral which describes the collisions between particles inside a cell.

In most classical DSMC methods, the molecules are modeled as hard sphere particles, and collisions between particles are stochastic. The stochastic collisions make the method significantly faster than Molecular Dynamics method. The sizes of the particles are not taken into account unlike MD.

The variable soft sphere model (VSS) was developed by Koura and Matsumoto^[93]. It is used instead of a hard sphere model for computing a correct diffusion coefficient in gas mixtures since it allows non-isotropic scattering. However, as long as the system does not accommodate a large temperature gradient, the hard sphere model will provide similar result as the VSS model. For an isothermal micro and nanoflow simulations, the hard sphere model is acceptable.

In the DSMC method, the domain is subdivided into cells with dimensions proportional to the mean free path length λ . The average cell size is chosen to be $\Delta x_{cell} \simeq \lambda/3$ ^[122].

In Figure 2.12, typical steps for a DSMC are described by a flow chart. The following five steps are important elements of Bird's DSMC method:

1. *Computation of the motion of the particles in time Δt .*

The particles move as if they do not interact with each other. So, unlike MD, the particles can move through each other. When particle position is r_i and its velocity v_i , the new positions are determined by

$$r_i^{t+\Delta t} = r_i^t + v_i^t \Delta t. \quad (2.33)$$

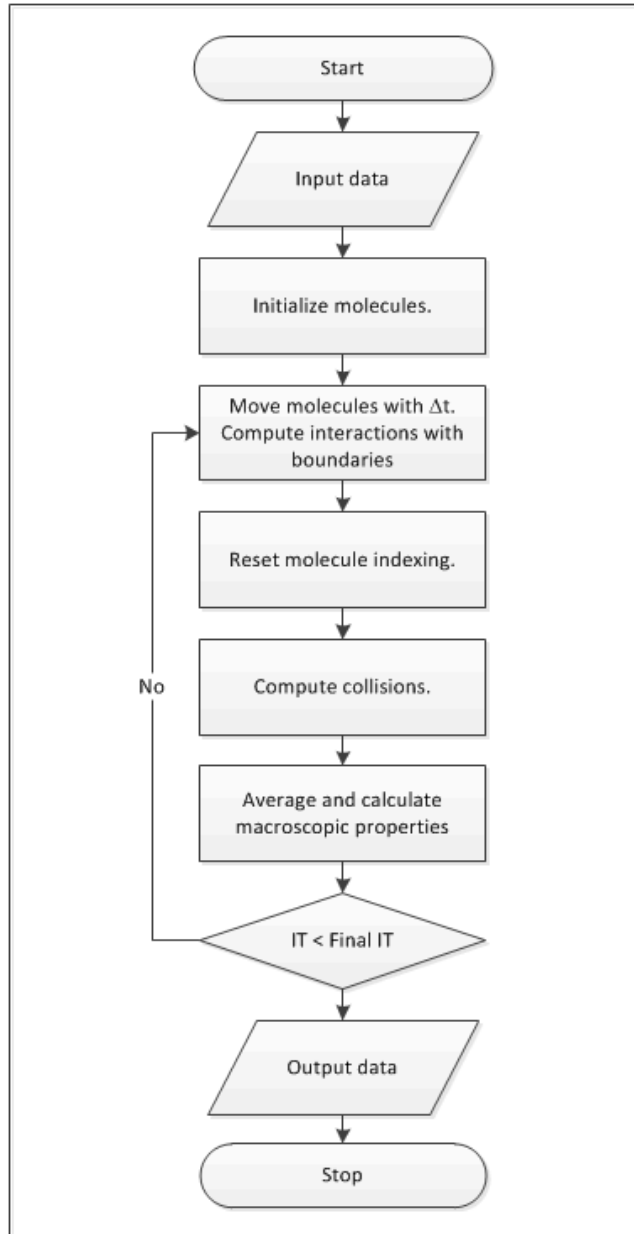


Figure 2.12: Flow chart for a DSMC method.

The boundary conditions must be enforced at this level to ensure the molecules stay in the computational domain.

2. *Indexing and cross-referencing of the particles into the cells.*

The particles are sorted into the spatial cells. Only the new positions $r_i^{t+\Delta t}$ are considered in the indexing.

3. *Simulation of the collision.*

It is assumed that only particles in the same cell can collide. Random pair of particles are selected among the particles within the cell for the collision. Only the magnitude of relative velocity between particles is used to determine the collision probability. No information on the particle position is used here. The collision probability for a pair of hard spheres, i and j , is determined by

$$P_{coll}(i, j) = \frac{|v_i - v_j|}{\sum_{m=1}^{N_c} \sum_{n=1}^{m-1} |v_i - v_j|} \quad (2.34)$$

where N_c is the number of particles in the cell. Since double summation in the denominator is expensive, it is approximated by

$$P_{coll}(i, j) = \frac{|v_i - v_j|}{v_{r,max}} \quad (2.35)$$

where $v_{r,max}$ is an estimation of the maximum relative speed in the cell. A pair of potential collision partners is chosen at random from particles within a cell, and the collisions are accepted if $\frac{|v_i - v_j|}{v_{r,max}} > r$ where r is a random number between 0 and 1. Even particles that move away from each other may ‘collide’ in the DSMC method. Unlike the Molecular Dynamics approach, no Newtonian trajectories are computed. This works well as long as the dimension of a cell is not larger than the mean free path^[8].

4. *Calculation of the positions after collision.*

Assuming that all molecules are hard spheres with the same mass and taking the conservation of linear momentum and energy into account, the new velocities v'_i and v'_j are

$$v'_i = v_{cm} + 0.5v'_r, \quad (2.36a)$$

$$v'_j = v_{cm} - 0.5v'_r \quad (2.36b)$$

where the center-of-mass velocity $v_{cm} = 0.5(v_i + v_j)$ and the relative velocity $v'_r = |v_i - v_j|[(\sin\theta\cos\phi)\hat{x} + (\sin\theta\sin\phi)\hat{y} + \cos\theta\hat{z}]$, and the angles are chosen such that they are uniformly distributed over the sphere.

5. *Calculation of the number of collisions that should occur during a time step Δt .*

The last step of the collision process is to determine the number of collisions that should occur in a cell during a time step Δt . The number of candidate collision partners (per unit time per unit volume), including those rejected, is taken to be $\frac{1}{2}n^2\pi\sigma^2v_{r,max}$ ^[61].

The DSMC method does not calculate exactly the collisions as in Molecular Dynamics, but generates collisions stochastically with scattering rates and post-collision velocity distributions determined from the kinetic theory of a dilute gas. In order to simulate dense gas, Frezzotti^[58] extended the DSMC version solving the Enskog equation,

$$\frac{\partial f}{\partial t} + v \cdot \nabla = J_E(f, f). \quad (2.37)$$

The collision integral $J_E(f, f)$ describes the collisions between particles inside and between cells, instead of only the collisions inside the cells as in the Boltzmann equation. The collision integral is defined by

$$J_E(f, f) = a^2 \int (Y[n(r + \frac{a}{2}\hat{k}, t)]f(r + a\hat{k}, v'_1, t)f(r, v'_2) - Y[n(r - \frac{a}{2}\hat{k}, t)]f(r - a\hat{k}, v_1, t)f(r, v_2) \times H(v_r \cdot \hat{k})(v_r \cdot \hat{k})dv_1d^2\hat{k},$$

where $Y(n)$ is the pair correlation function at contact, which depends on the density n . a is the particle diameter, \hat{k} is a unit vector which specifies the relative position of the particles at the time of impact, H is the Heaviside function, and $v_r = v_1 - v_2$ is the relative velocity of two colliding particles. The velocity v' denotes a velocity after collision.

Frezzotti's DSMC method allows the gas to be characterized by the particle positions, velocities, mass, and diameter unlike Bird's method. Also in Frezzotti's method, the collisions take place not only inside a cell, such as in the DSMC method by Bird, but also in the neighboring cells. Because of the interaction between the particles of neighbouring cells, the collisions can not be solved independently as in DSMC approximation of the Boltzmann equation. An advantage of the Enskog equation is that in the case that the number of particles is equal to the number of molecules, the method gives the same stochastic results as the exact molecular dynamics equation for hard spheres, but is more efficient^[58].

The following three steps are important elements of Frezzotti's DSMC:

1. *Simulation of the collision.*

The probability for a particle to have a collision is found from the contribution of that particle to the total number of collisions. Particle i contributes to the number of collision N_{coll} with the term $2\pi\sigma^2 A_i C_i$, so the probability $P_{coll}(i)$ that particle is selected for a collision is

$$P_{coll}(i) = \frac{2\pi\sigma^2 A_i C_i}{N_{coll}}. \quad (2.38)$$

A_i , C_i and N_{coll} are described as,

$$A_i \geq n_m Y\left(n\left(r - \frac{\sigma}{2}\hat{k}, t\right)\right), \quad (2.39a)$$

$$C_i \geq \|v_{m,j} - v_i\|, \quad (2.39b)$$

$$N_{coll} = \frac{1}{2} \left\langle \sum_{i=1}^N 4\pi\sigma^2 A_i C_i \right\rangle. \quad (2.39c)$$

2. *Select collision partner in neighboring cell.*

In Frezzotti's DSMC method, collisions with neighboring cell m , are also taken into account:

$$P_{coll}(m, i) = \frac{1}{4\pi} \int_{S(m,i)} d\hat{k}. \quad (2.40)$$

The cell of the collision partner for particle i is selected by drawing a random vector from the position of particle i . If cell m is chosen in that way, a particle j is chosen from that cell with probability

$$P_{coll,i}(m, j) = \frac{1}{N_m}. \quad (2.41)$$

This shows that every particle j in cell m has equal probability to be selected as a collision partner of particle i .

3. *Simulation of a collision.*

Because the probability that particle i and j are selected for collision include false collision, the probability of a real collision should be determined by probability $\phi(\hat{k})$. This probability $\phi(\hat{k})$ is given by

$$\phi(\hat{k}) = \frac{n_m Y\left(n\left(r - \frac{\sigma}{2}\hat{k}, t\right)\right) H(v \cdot \hat{k})(v \cdot \hat{k})}{A_i C_i}, \quad (2.42)$$

where $Y(n)$ is the pair correlation function at contact and a is the particle diameter. \hat{k} is a unit vector which specifies the relative position of the particles at the time of impact. H is the Heaviside function.

Assuming that all molecules are hard spheres with the same mass and taking the conservation of linear momentum and energy into account, the new velocities v'_i and v'_j are

$$v'_i = v_i + (v_r \cdot \hat{k})v_r, \quad (2.43a)$$

$$v'_j = v_j + (v_r \cdot \hat{k})v_r. \quad (2.43b)$$

PumMa DSMC was built based on Enskog equation. It was developed and validated by van der Akker^[162] with Frezzotti's DSMC code.

2.5 Conclusion

In this chapter, we described the theory and the numerical methodologies for simulating liquid and gas micro flows at the atomistic level. First, we presented the Molecular Dynamics (MD) method, a deterministic approach suitable for micro-nano system. Numerical measurement techniques, boundary conditions, and controllers are discussed for flow and heat transfer simulation. We then gave an overview of ReaxFF, describing the details of reactive empirical force field method. We also presented the Direct Simulation Monte Carlo (DSMC) method, a stochastic approach that is used often to simulate gases in micro-nano systems.

3

Geometry effects on rarefied nanochannel flows

A three dimensional Molecular Dynamics method has been used to study the effect of different geometries for rarefied gas flows in nanochannels. Argon molecules are used. The velocity profiles in the channel are obtained and analyzed with three different channel geometries: a circular, a rectangular (square), and a slit channel. A channel width of $50nm$ is used for the simulation. It is found that when using the same driving force, the maximum velocity of the flow increases when the geometry changes in the order from circular to rectangular to slit geometry, where the latter becomes 2~2.5 times as large compared with either the rectangular or circular channel. For Kn larger than 1.0, the rectangular channel shows a similar maximum and slip velocity as the circular channel while the velocity profile is qualitatively similar to the slit channel. The effect of different Knudsen numbers on the velocity profiles is also investigated. We found that for Kn larger than 2~3, the Knudsen number has a relatively small influence on the slip velocity for circular channels and rectangular channels. The effect of the accommodation coefficient on the average flow velocity for all three geometries is studied and expressed as an allometric equation model.

3.1 Introduction

Gas flows at micro and nano scale have recently gained interest due to the rapid developments in MEMS and NEMS. In the process of miniaturizing these components, surface effects dominate the fluid flows in these devices due to the large surface to volume ratio. On micro and nano scale, the viscous forces are of

Parts of this chapter are described in:

Kim, J., Frijns, A. J. H., Nedeia, S. V., and van Steenhoven, A. A. Geometry effects on rarefied nanochannel flows. *Microfluidics and Nanofluidics*, 15(5): 661-673, 2013.

the same order of magnitude as inertial forces contrary to a macro-scale vessel where viscous forces are usually negligible compared to inertial forces^[59,65].

The rarefaction effect is one of the most important characteristics of gaseous nanochannel flows, as the molecular mean free path is comparable to the channel's characteristic dimension. The effect can be characterized by the Knudsen number, Kn , which is defined by the ratio of the molecular mean free path λ to the characteristic length of the duct H . The Knudsen number is very small for continuum flows, $Kn < 0.1$ and is increasing as the gas mean free path λ becomes comparable with the characteristic length of the channels (e.g. in small channels and/or, dilute gases). For $Kn > 10.0$ it is considered to be a free molecular flow. Our interest is in studying the rarefaction effects in the different channel geometries for flows going from transition to the free molecular regime. Important experimental studies of gaseous flows in micro channel for different flow regimes have been performed by many researchers^[38,52,63]. However, experimental investigations of nanochannel flows still have many difficulties due to the scale limitation of current experimental devices, and therefore, several numerical methods and simulations have been widely used to study the nano channel flow behaviours^[118,119,177].

A variety of researchers attempted to develop second-order slip models that can be used in the transition regime^[13,49,83,134]. However, there are large variations in the second-order slip coefficients. Jeong et al.^[83] and Jang et al.^[82] focused their study on gaseous slip flow in rectangular microchannels. The effects of the aspect ratio of the channel and the outlet Knudsen number on pressure nonlinearity slip velocity, and the mass flow rate are investigated. Their results of the extreme wide rectangular geometry cases agree well with the results of slit microchannels. Barber and Emerson^[13] conducted an investigation of gaseous slip flow at the entrance of circular and parallel plate microchannels using a two-dimensional Navier-Stokes solver. They indicated that the Knudsen number has a significant effect on the hydrodynamic entrance length in the case of parallel plates.

Recently Duan et al.^[50] studied a slip flow in the hydrodynamic entrance region ($0.001 < Kn < 0.1$) of circular and noncircular micro-channels (rectangular and parallel plate channels). Graur et al.^[64] studied a non-isothermal rarefied gas flow along a tube with an elliptical cross section due to pressure and temperature gradients. This flow behavior is studied using the S-model kinetic equation in the whole range of the Knudsen number covering both free molecular regime and hydrodynamic one. However, in all these papers, there is no comparison on the slip flow of three different geometries for the transition and free molecular regime. In 2011, Rykov et al.^[134] presented the results of independent studies of Poiseuille flow in a channel of an elliptical cross-section and a rectangular channel for the transition and free molecular regime. However, in Rykov's work, the main results are focusing only on the behavior of the flow rate using the BGK model. Other characteristics like slip velocity of fluids are not included.

To account for an accurate description of slip velocity and profiles in very small channels with different geometries, we use molecular dynamics simula-

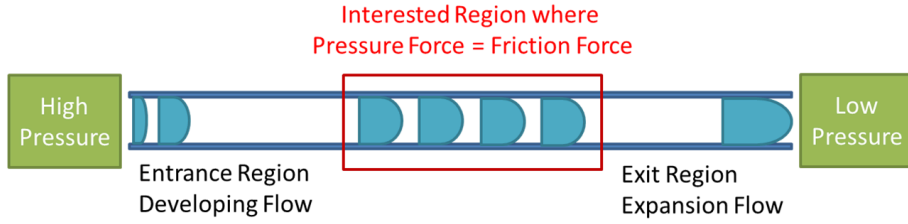


Figure 3.1: Developing flow inside a very long channel and the fully developed region, the region of interest.

tions. To understand this flow in nanochannels, the rarefied gas flow has been studied extensively as a two dimensional problem using molecular dynamics^[27,153]. But the solution of this two dimensional study cannot describe the difference between the flows inside circular, rectangular and slit channel. Therefore, we will use a three dimensional MD simulation method to analyse the geometry effects.

The goal of this chapter is to study the effect of different geometries on the fully developed gas flow in the nanochannels covering the transition to the free molecular regime ($0.2 \leq Kn \leq 10.0$). The effect on velocity profile, slip velocity, maximum velocity, and the effect of different accommodation coefficient on the normalized average flow velocity will be studied.

3.2 Method

3.2.1 Methods outline

For the analysis the Molecular Dynamics Code PumMa^[2] is used here. It has been used for researches in the area of nano flow and heat transfer^[118]. Other simulation methods (more advanced versions of DSMC, or Lattice-Boltzmann method) can also be used here instead of Molecular Dynamics. However, we have chosen MD as our main simulation method to simulate outgassing of water inside a silica nanopore. MD is used here instead of other methods since this chapter is a building bridge to reach the final chapter.

To study the effect of different geometries on the gas flow in the nanochannels, we are interested in a fully developed flow in a very long nanochannel as shown in Figure 5.2. Inside a very long channel ($L \gg H$), the pressure in a cross-sectioned area becomes uniform and the pressure difference over a segment, multiplied by the cross-sectional area (denoted as pressure force), is equal to the friction force of the wall to the gas (friction force). Then the gas will develop to a certain velocity profile which does not change anymore. In this study, we use gravity-fed method and periodic system to simulate this problem.

Gravity-fed flow is one of the main methods in Non-Equilibrium Molecular Dynamics simulation to prescribe pressure driven flows^[67]. The idea of the

Table 3.1: Molecular Dynamics properties for argon (Ar)^[118]

Argon Particles	
Molecular diameter, σ_{Ar}	0.340nm
Mass, m_{Ar}	$6.63 \cdot 10^{-26} kg$
Energy well depth, ϵ_{Ar}/k_B	121K
Cut-off Radius, r_c	$2.5\sigma_{Ar}$

gravity fed flow here is to replace the pressure gradient with an external field when the Knudsen number is high enough. In this research, a Poiseuille flow is induced by subjecting the gas molecules to an external driving field $g_x = 3.68 \times 10^{10} m/s^2$ in the whole domain assuming the local pressure gradient to be small. The external driving field is chosen so that it gives large enough flow velocity to maximize the accuracy, and low enough to avoid viscous heating. By placing an initializing buffer in the beginning of the system box, a developing flow starting from macroscopic initial velocity $U_x = 0m/s$ is modeled. This buffer is soon removed to have a fully periodic system. Boundary layers will develop along the walls and the velocity is gradually redistributed due to the viscosity. Since the system is fully periodic, velocity will keep on increasing, and eventually the fluid will reach a velocity where the friction force is equal to the gravitational force. In this case the velocity is independent of the axial direction, and under such condition the flow can be considered as a fully developed flow.

Our molecular dynamics simulations consider a 3D system of N argon molecules confined in a nanochannel. The walls are modeled by a thermal wall condition^[119,177]. In a thermal wall(also known as a diffusive wall), a particle that collides with the wall is assumed to have so much interaction with the wall, that the outgoing velocity is completely determined by the wall temperature. This means that the new velocity of a particle after the collision is drawn from the Maxwell velocity distribution. This boundary condition is widely used in other simulation techniques like DSMC and lattice Boltzmann.

The interaction between two argon molecules is described by truncated and shifted Lennard-Jones potential \mathcal{U} ^[118], with parameters as shown in Table 1:

$$\mathcal{U}(r_{ij}) = 4\epsilon \left(\left(\left(\frac{\sigma}{r_{ij}} \right)^{12} - \left(\frac{\sigma}{r_{ij}} \right)^6 \right) - \left(\left(\frac{\sigma}{r_c} \right)^{12} - \left(\frac{\sigma}{r_c} \right)^6 \right) \right). \quad (3.1)$$

In this equation, r_{ij} is the distance between two particles, and r_c is the cut-off radius. The Lennard-Jones potential parameter ϵ represents the energy well depth of untruncated Lennard-Jones potential, and σ represents the molecular diameter of the particles. This equation is only valid for $r < r_c$. The potential is set to zero when the intermolecular distance $r > r_c$.

Three different cross-section geometries (a channel with a circular, rectangular, and a slit) are simulated (Figure 4.1). The simulated characteristic length, i.e.: the separation distance between the plates for the slit channel, the diameter of the circular channel, and the height of the rectangular

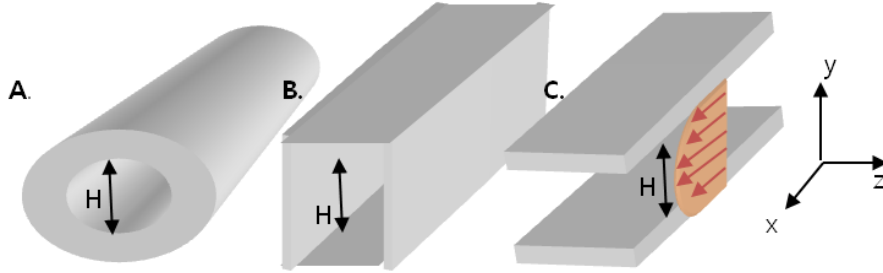


Figure 3.2: Three different nano-channels; A. Circular Channel, B. Rectangular Channel, C. Slit

channel, is $H = 50nm$, which is comparable with the characteristic size of NEMS(Nanoelectromechanical systems) devices in engineering situations^[65]. In the flow direction, the x directional length is $100nm$.

The Knudsen number of the whole system is chosen to be 0.2, 0.3, 0.4, 0.5, 1.0, 5.0 and 10.0. The walls are kept at a constant temperature $T_w = 300K$. Different numbers of particles are considered depending on the Kn of the geometries. The number of particles varies from 1910 ($Kn = 10.0$, Circular Channel) to 121593 ($Kn = 0.2$, Slit and Rectangular Channel). Knudsen number is defined as $Kn = \lambda/H$. Mean free-path λ is defined as:

$$\lambda = \frac{1}{\pi\sqrt{2}\sigma^2n} \quad (3.2)$$

where number density, $n = \frac{N}{V}$. N is number of particles and V is the volume of the channel in the given system.

A thermal boundary condition is applied as a boundary condition in this research. Since an accommodation coefficient α for most experimental situations is positioned between 0.95 and 1.0 (thermal wall)^[139], and the study is focused on the geometry effect rather than the wall-gas interaction, this boundary condition covers our interest. A periodic boundary condition is applied for the lateral sides of the slit channel.

92 sampling cells along the channel diameter are used to sample the velocity profile. Cells with a radial cross section are used for the sampling of circular geometry, while cells with a rectangular cross section are used for rectangular and slit geometry. The cell size of rectangular channel is smaller than the cell size of slit because the sampling of rectangular geometry only took place in the center part of the channel.

To reach a steady flow state, a typical computation in our simulations requires 5,000,000 time steps for flows with $Kn \leq 0.5$, and 10,000,000 time steps for flows with $Kn \geq 1.0$. For computing the averaged macroscopic properties: flow velocity, maximum velocity, etc., we spent about 20,000,000 additional time steps for flows with $Kn \leq 0.5$, and 40,000,000 additional time steps for flows with $Kn \geq 1.0$.

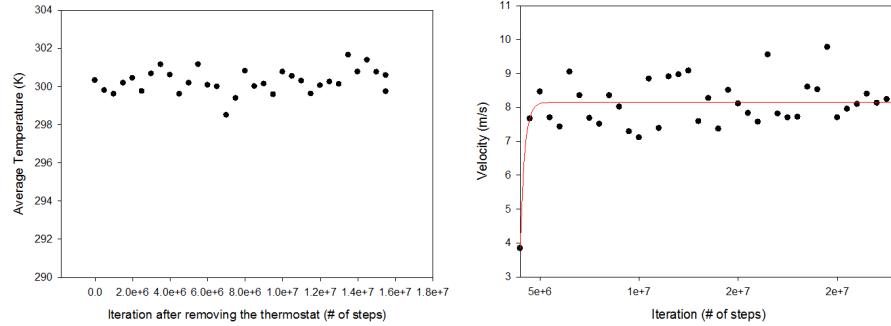


Figure 3.3: Average temperature (left) and average velocity (right) for the slit geometry (at $Kn = 0.5$, $H = 50nm$, $g_x = 3.68 \times 10^{10} m/s^2$) as a function of the number of iteration steps.

3.2.2 Validation of the method

In 2010, To et al.^[156] have introduced a new slip model for micro/nano gas flows induced by the body force. A particular case is studied where a gas flow with viscosity, μ , is induced by a constant body force along one direction x . However, the paper does not specify the situation whether the method can replace a pressure driven flow. Here we will validate the body force induced method and will determine the situations where this method is valid.

Validation of the method is performed in three different aspects. First, it is checked whether the gaseous system went into a steady state even though the body force is applied to the fully periodic system. Temperature and average velocity are shown in Figure 3.3 as a function of the number of iteration steps. For this test simulation, a slit channel with $Kn = 0.5$ is used. In the graph, the temperature is maintained constant without any additional thermostat; acceleration is chosen to be low enough to avoid the viscous heating. The thermal boundary wall condition ($T = 300K$) acted like a quasi-thermostat. The average velocity initially increased due to the acceleration, but it went into a steady state when the body force and friction force matched each other.

In the second part of the validation, it is checked whether the use of a body force resembles the real rarefied gaseous flows. First the pressure distribution along a channel is examined. In continuum flow, when Mach number is below 0.1, it is considered as an incompressible flow. Here all velocities are below Mach number of 0.036. Therefore the flow is considered to be incompressible.

The experimental results in Liu et al.^[105], showed a nonlinear pressure distribution for gaseous flows. But it also showed that for the rarefied flow, the curvature is more pronounced for high pressure ratios. For cases with $P_{in}/P_{out} < 1.2$, the pressure drop is practically linear, resembling an incompressible flow. This indicates that when dP/dx is low enough, the flow can also be assumed to be incompressible. For the flow, where the channel length is $100nm$ and gravity

field $g_x < 12 \times 10^{10} m/s^2$, it is found that it resembles an incompressible flow. Here, the gravity is chosen as $g_x = 3.68 \times 10^{10} m/s^2$ which is in the range of linear pressure drop.

However, for rarefied gas flow, rarefaction effect is the biggest reason which allows to use the gravity fed flow method. It is shown in the air flow simulations for different Knudsen numbers^[125], that the stronger the rarefaction effect, the smaller the deviation is from the linear pressure distribution. In Pong's experiment^[125], it was shown that for $Kn \geq 0.3$ the deviation was minimal. In this research the flow in the range from Kn of 0.2 to 10.0 is studied. This is the range where the deviation from the linear pressure distribution is small. So we can neglect the effect of compressibility effect in the pressure distribution for this research. We performed a developing flow MD simulation with a pressure controller in the inlet and outlet. Our simulation shows that for $Kn \geq 0.2$ we have a linear pressure drop even for P_{in}/P_{out} ratio out of the range of Liu et al.^[105].

The last part of the validation contains the study of the independence in flow profile on dP/dx . Four different accelerations are applied to the system for three different Kn numbers. For different accelerations, it gives nearly an identical profile. Four different acceleration fields are tested here; $3.7 \times 10^{10} m/s^2$, $0.7 \times 10^{10} m/s^2$, $0.4 \times 10^{10} m/s^2$, and $0.2 \times 10^{10} m/s^2$ (Figure 3.4). Not all colors are visible in the Figure 3.4 due to overlap. The study shows that the flow profile is independent on dP/dx but only dependent on the Kn .

These simulations show that this method can be used to study the geometric effect and Knudsen effect on the velocity profile in a given system.

3.3 Results and discussion

In our simulations, we divide the whole channel into 100 bins to compute space and time averaged velocities. The segmental width of each bin is $0.5nm$. The velocity profiles in x direction obtained by our simulations are shown in Figure 3.5. In case of rectangular geometry the sampling is done in the middle part of the channel. So it does not represent the whole velocity profile but only the center part.

3.3.1 Data and error analysis

Usually, second order polynomial is used in order to compare the velocity profile predicted by MD and Navier-Stokes^[180]. In this study, the time averaged simulation results are fitted also by a 2nd order polynomial equation. MD simulation results for a slit flow and its fitting for each Knudsen number are shown in Figure 3.6.

As shown in Figure 3.7, the noise level of the circular channel increases near the centerline. It goes up to 10% of fitted polynomial curve due to the decrease of sampling area and therefore a decrease in the number of molecules. However, noise near the centerline has a minor influence to overall fitted curve

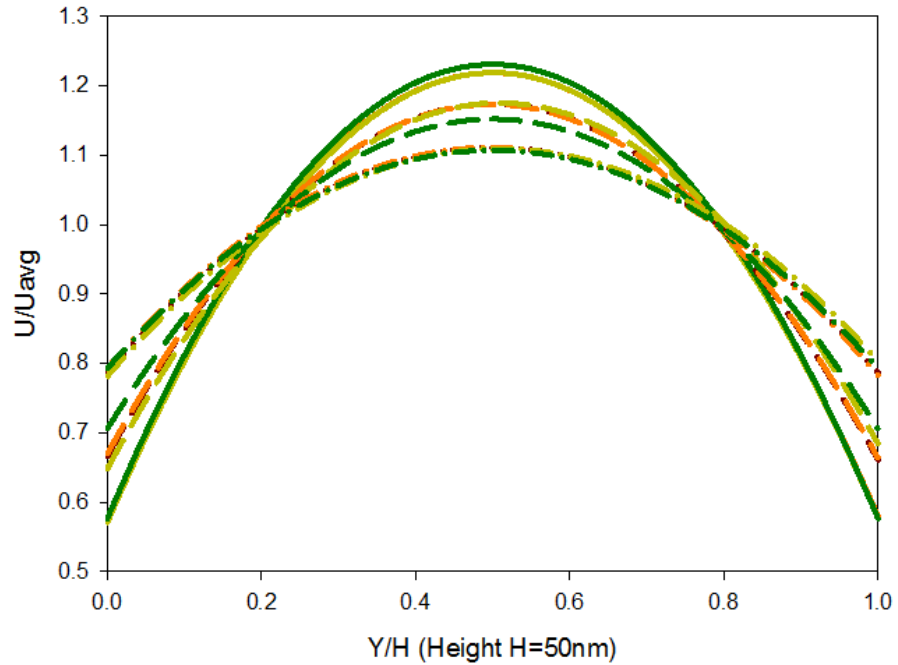


Figure 3.4: Velocity profile in 50nm slit channel for four different accelerations (Red: acceleration $3.7 \times 10^{10} m/s^2$, Orange: $0.7 \times 10^{10} m/s^2$, Light Green: $0.4 \times 10^{10} m/s^2$, Green: $0.2 \times 10^{10} m/s^2$) and for three different Knudsen numbers (Solid line: $Kn = 0.5$, Dash line: $Kn = 1.0$, Dash-dot line: $Kn = 5.0$)

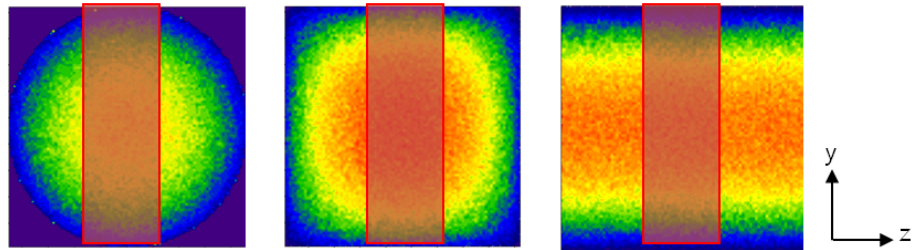


Figure 3.5: Contour velocity profile of 3 different geometries: circular, rectangular, slit channel. Red box indicates region where the velocity profile is determined. Velocity scale ranges in the order of red(high), yellow(Medium), blue(low), but the geometries have different values for each color.

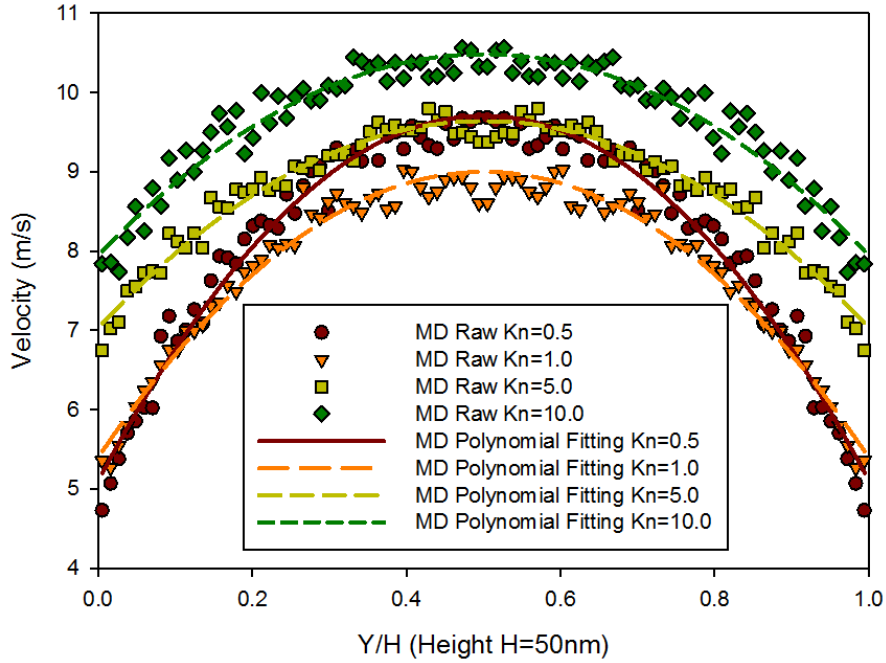


Figure 3.6: MD results and polynomial fittings in 50nm slit channel for several Knudsen numbers, in case of a thermal wall boundary condition.

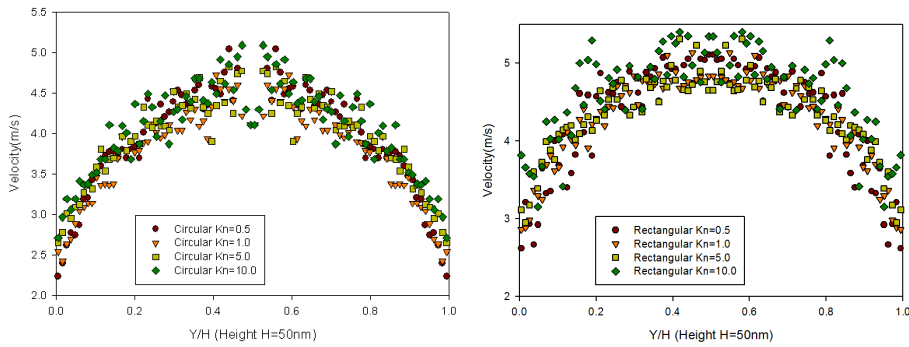


Figure 3.7: MD results in 50nm circular and rectangular channel for several Knudsen numbers, in case of a thermal wall boundary condition.

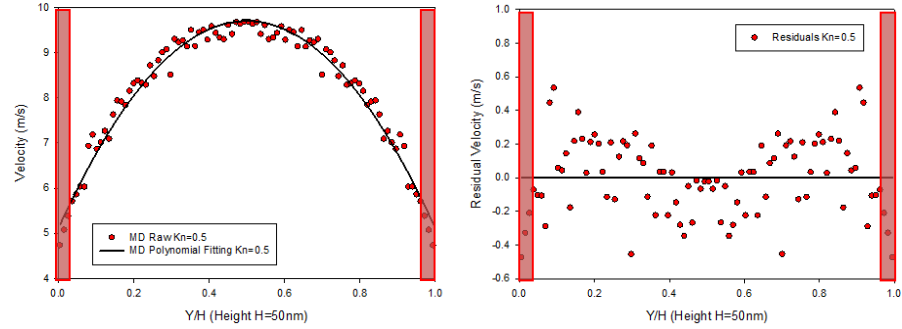


Figure 3.8: Velocity profile in 50nm slit channel at $Kn = 0.5$. Comparison between actual MD results and 2nd order polynomial fitting.

line; the fitting is mostly dependent on the outer region, because they contain more particles. The noise level of the rectangular channel is higher compared to slit geometries since the profile is only sampled in the center part of the channel and therefore also less molecules are used in the averaging procedure.

The error for each position and for each geometry, are calculated through Origin 8.5 Software^[4]. The difference between the MD results and polynomial fitting for slit geometry is shown in Figure 3.8. Residual velocity is a subtraction from the polynomial fitting value to the MD simulation result value. For all geometries and for all Knudsen numbers, residuals show a similar trend: the velocity near by the wall boundary is overestimated. It suggests that the 2nd order polynomial equation is not good enough to fully describe the velocity near the wall border in the nanochannel flow situation. The slip velocity calculated by molecular dynamics give approximately 90% value of the slip velocity by polynomial fitting regardless of geometry and Knudsen number. Adjusted RMS (Root Mean Squared) value of the simulations varies from 0.97 to 0.85. It shows a decrease in adjusted RMS value when Knudsen number increases.

3.3.2 Velocity profile

The maximum velocity of the flow increases when the geometry changes in the order from circular geometry to rectangular geometry to slit geometry (Figure 3.9a). The latter becomes 2 ~ 2.5 times as large compared to either the circular or rectangular channel. This is largely influenced by the smaller boundary area/volume ratio (circular : rectangular: slit = 1 : 1 : 2) and therefore relatively low gas-wall interactions. While the absolute value of the velocity profiles shows a distinct difference according to the different geometries, geometry effect on the shape of the velocity profile also shows an interesting feature: the slit channel has a flatter profile compared to the other two channels (Figure 3.9b). The maximum velocity of a circular channel and a rectangular channel are close (Figure 3.9a) while there is a relatively large difference in the normalize slip

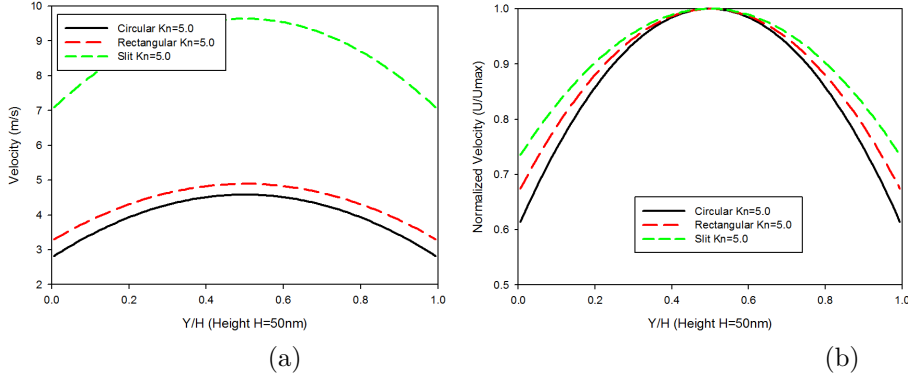


Figure 3.9: (a) Velocity profile for different geometries with $Kn = 5.0$, and thermal wall boundary condition ($T = 300\text{K}$). (b) Normalized velocity (U/U_{max}) profile for different geometries with $Kn = 5.0$, and thermal wall boundary condition.

velocity (Figure 3.9b).

Figure 3.10 shows that the Knudsen number has a positive impact on the maximum flow velocity for the slit geometry for $Kn > 1.0$. The Knudsen point where the profile changes is comparable to the Knudsen minimum (the Knudsen regime where flow rate goes to minimum). The Knudsen minimum for slit channel is known to be lying near $Kn \simeq 1.0$. For the circular and rectangular geometry, it is found that the Knudsen number has a comparably small influence on the maximum velocity while the slip velocity is increasing with the increasing Knudsen number (Figure 3.11). The simulation with a larger cutoff radius ($r_c = 4.0 \sigma$) is also carried out to check the effect of the cut-off radius. However, it gave less than 3 % difference in the velocity profile and less than 0.1 % difference in the density profile with more than 10 times larger simulation time than previous simulations with $r_c = 2.5 \sigma$.

3.3.3 Slip velocity for different Knudsen numbers

For the case of $0.01 \leq Kn \leq 0.1$ in smooth nano channels, the gas slip velocity is clearly dependent on the Knudsen number (Figure 3.12). This is the consequence of the non-equilibrium phenomena arising from infrequent collisions of gas particles by rarefied gas dynamics^[135]. However, our results in Figure 3.12 also show a different behavior for $Kn \geq 1.0$. The normalized slip velocity (slip velocity to maximum velocity ratio) approaches an asymptotic value. It is found that the Knudsen number has a comparably small influence on the slip flow velocity for circular channel and rectangular channel for the region for $Kn \geq 1.0$. Figure 3.12 shows that the normalized slip velocity increases when the geometry changes from the circular channel to the rectangular channel and to the slit channel.

A high normalized slip velocity for the rectangular channel compared to the

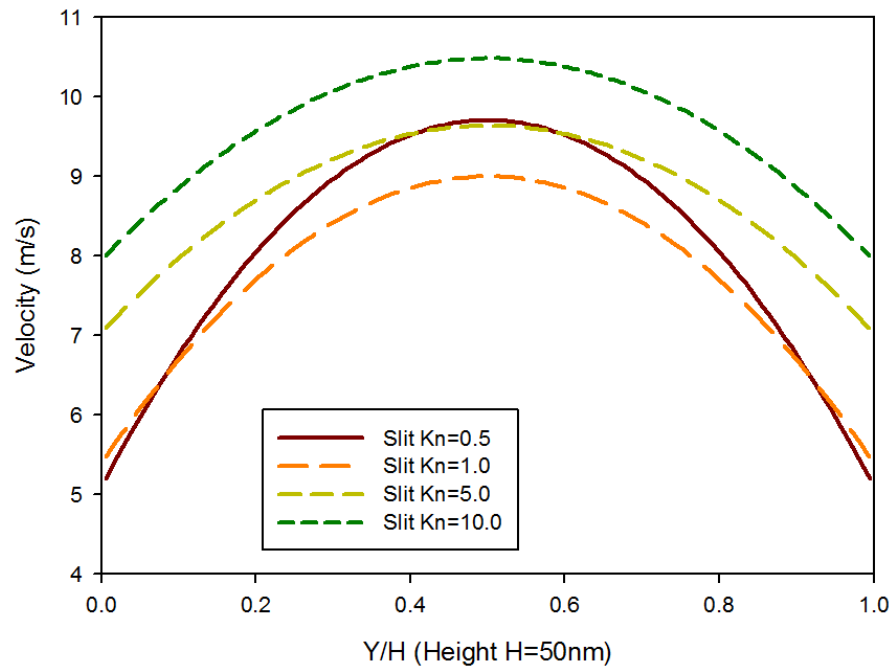


Figure 3.10: Velocity profile in 50nm slit channel for several Knudsen numbers, in case of a thermal wall boundary condition.

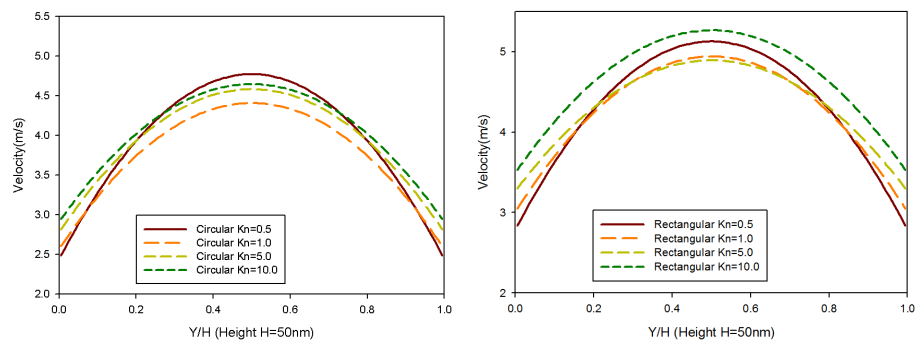


Figure 3.11: Velocity profile in 50nm circular and rectangular channel for several Knudsen numbers, in case of a thermal wall boundary condition.

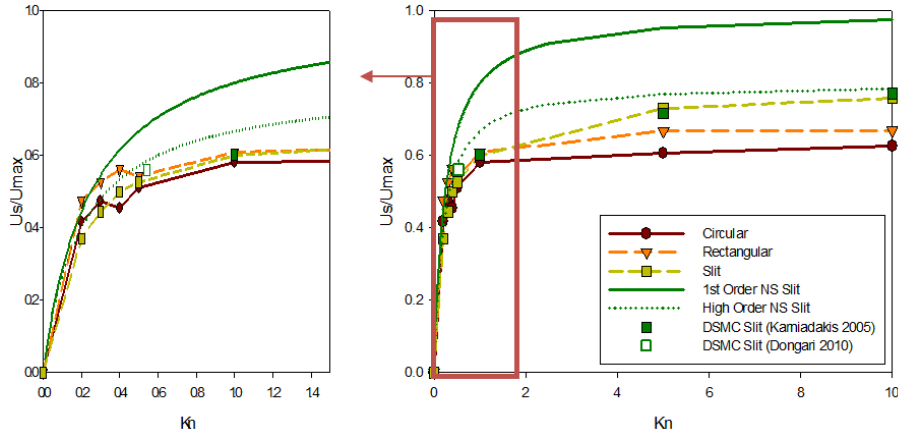


Figure 3.12: Normalized slip velocity (U_s/U_{max}) as function of Knudsen numbers. MD simulations are performed for $0.2 \leq Kn \leq 10.0$, in case of a thermal wall boundary condition. The first order and high order approximation based on NS equations lines indicate the results from equation 3.3 and 3.4.

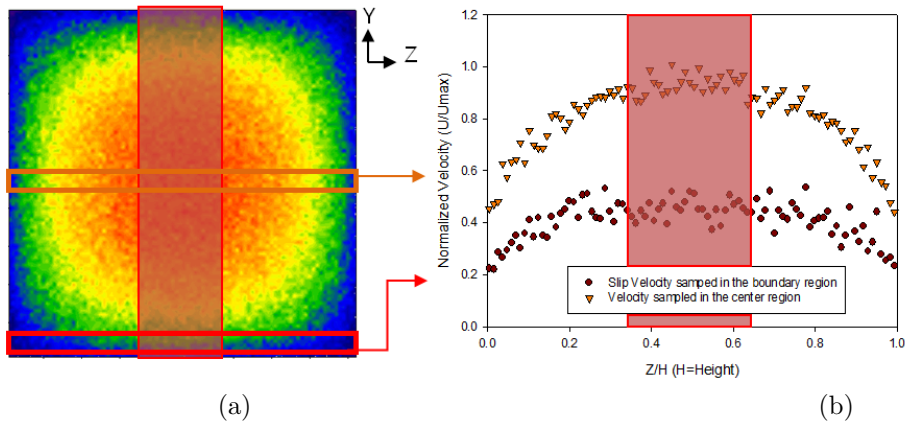


Figure 3.13: (a) Contour velocity profile of rectangular channel at $Kn = 0.2$. Orange box shows a velocity in the center region and red box shows a slip velocity. (b) Slip velocity and center velocity profile. Sampling region of rectangular flow is shown as a red translucent box for both Figures

other two channels can be observed when $Kn < 0.5$. As mentioned earlier, in case of a rectangular channel the sampling is done in the middle part of the channel. Therefore, the high normalized slip velocity is due to the high slip velocity in the center part of the surface boundary which is shown in Figure 3.13. The orange scattering points represent the center velocity along the z -axis, and the red scattering points are the slip velocity along the z -axis. A low normalized slip velocity will be obtained, if we sample the velocity diagonally from one corner to the other corner of the channel.

However, the normalized slip velocity in the rectangular geometry gets an intermediate value between the circular channel and the slit channel in the region $Kn > 1.0$. The geometric effect due to the four corners of rectangular channel decreases when the gas is rarefied. Difference in the minimum normalized volumetric flow rate as a function of Knudsen (known as Knudsen minimum or Knudsen's paradox) for different geometries is also the reason for the different trend for rectangular channel. Sharipov^[117,138] also showed the difference in the Knudsen minimum in the transition regime for rectangular channel and slit channel.

In case of the circular and the slit channel, a similar increase is found in normalized slip velocity for $Kn < 0.5$. In this region, the continuum regime is valid and the profile resembles the Navier-Stokes profile. In Figure 3.12, the analytical results from the first and high order approximation based on Navier-Stokes equations are plotted against MD results for the normalized slip velocity. The first (Equation 3.3) and high order approximation equations (Equation 3.4) are as follow:

$$\frac{U_{slip}}{U_{max}} = Kn / \left(\frac{1}{4} + Kn \right) \quad (3.3)$$

$$\frac{U_{slip}}{U_{max}} = \frac{Kn}{1 + Kn} / \left(\frac{1}{4} + \frac{Kn}{1 + Kn} \right) \quad (3.4)$$

Equation 3.3 is obtained by using the first order slip wall condition proposed by Maxwell and equation 3.4 by using a high order condition^[19]. The difference between the first order and the high order approximation becomes more apparent for high Knudsen number values. In fact, Figure 3.12 shows increasing differences between the approximations and simulation results when Kn is increasing. The difference between the approximations is even larger for the circular channel than for the slit channel since the normalized slip velocity start to deviate from the region where $Kn > 0.5$. When Kn goes to infinity, the first order approximation and the high order approximation give values of 1.0 and 0.8 respectively, while our simulation results give estimated asymptotic values of 0.77 for slit, 0.67 for rectangular, and 0.63 for circular channel. DSMC results of Karniadakis et al.^[89] and Dongari et al.^[47] are also compared. In case of DMSC, the results agree well with our MD results.

The MD results can be compared with other studies of the slip velocity in the form of slip coefficients. Deissler^[45] derived a second-order slip boundary condition based on the concept of mean free-path for momentum and energy transfer, which can be generalized as:

Table 3.2: C_1 and C_2 value for Deissler's second-order slip boundary model^[45]

Kn	Circular Channel		Rectangular Channel		Slit Channel	
	C_1	C_2	C_1	C_2	C_1	C_2
0.2-0.5	1.133147	0.743039	1.446186	0.939876	0.903013	0.527649
0.5-1.0	0.841374	0.246943	0.943002	0.277233	0.890677	0.257824
1.0-5.0	0.433313	0.035644	0.507648	0.040729	0.536285	0.040136
5.0-10.0	0.117025	0.003756	0.150169	0.005050	0.201995	0.006179

$$\hat{U}_{slip} = C_1 Kn \left(\frac{d\hat{U}_x}{d\hat{y}} \right)_w - C_2 Kn^2 \left(\frac{d^2\hat{U}_x}{d\hat{y}^2} \right)_w \quad (3.5)$$

where \hat{U}_{slip} is the nondimensional slip velocity at the fluid-surface interface which is non-dimensionalized with a reference length and velocity scale. w indicates a quantity evaluated at the surface. While there is no general consensus on the slip coefficients C_1 and C_2 , C_1 is set to 1 by many authors and C_2 has a wide range from -0.5 to $5\pi/12$ ^[131]. Cercignani^[32] proposed C_2 to be 0.9756 and Hadjiconstantinou^[66] corrected C_2 to be 0.31.

In our MD simulation, C_1 and C_2 start to deviate from the constant value when $Kn > 0.5$. It shows a decrease with the increase in Kn . When Kn goes to infinity, C_1 and C_2 goes to 0. The values of C_2 for the slit geometry are smaller than the values of C_2 for the rectangular and slit while the difference in C_2 coefficients becomes smaller when $Kn > 0.5$. Overall, it can be concluded that Deissler's model (Equation 3.5) is good up to the beginning of transition regime ($Kn < 0.5$), but cannot predict the slip velocity of whole transition regime with a fixed C_1 and C_2 value. Our C_1 values have an error of approximately 3% ~ 5% error, while the C_2 values have an error of approximately 9% ~ 17% error. These errors are calculated by using the approximate solution of an overdetermined system. The multiple sets of the coefficients of the polynomial fittings of the MD results are used as an input. From our MD simulation, it is observed that $\frac{d\hat{U}_x}{d\hat{y}}$ and $\frac{d^2\hat{U}_x}{d\hat{y}^2}$ change with Kn . It is necessary to have a flow model, that describes the velocity profile accurately even for high Kn regimes, as an input in order to use this boundary condition for high Kn .

The advantage of using the normalized velocities is that they are independent on the channel size. For these simulations, we have checked the effect of the channel height on the simulation results. The simulation are performed by changing the size from $H = 10nm$ to $H = 100nm$. The results show an independence when the height is larger than $30nm$. The results are also valid for other monatomic gases since we used a Molecular Dynamics method with reduced units for computation and dimensionless parameters.

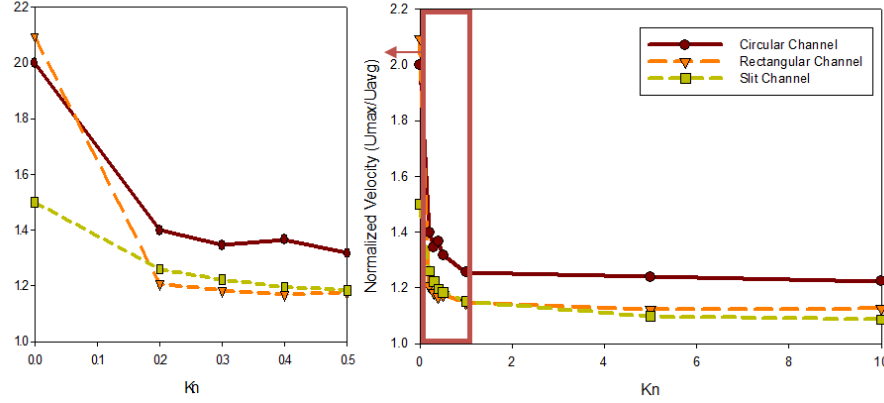


Figure 3.14: Normalized maximum velocity ($U_{max}/U_{average}$) as function of Knudsen numbers, in case of thermal wall boundary condition.

3.3.4 Maximum and average velocity

Normalized maximum velocity as function of Knudsen numbers is shown in Figure 3.14. In the continuum region, it is known to have a U_{max}/U_{avg} ratio of 2.0 for circular channel flow^[57], 2.1 for rectangular channel, and 1.5 for slit channel flow^[147]. To calculate U_{max}/U_{avg} ratios for high Knudsen numbers, U_{avg} values are sampled from whole channel areas for all three geometries. Our MD results for $Kn = 0.2 \sim 0.5$ show that this ratio also goes to these values that are calculated by continuum dynamics^[57,147] in the limit situation, where $Kn = 0$. High Kn flows are also simulated. The U_{max}/U_{avg} ratios for circular channel flows are around 1.2, while they are around 1.1 for slit channel flows. The simulation result also shows a decrease of the U_{max}/U_{avg} ratio as Kn increases. The U_{max}/U_{avg} ratios of rectangular flows are close to the ratios of slit flows. The U_{max}/U_{avg} ratio of slit and rectangular channels started with different values in the low Kn regime, but the ratio get close to each other when it goes into transition regime.

3.3.5 Flow rates in 2D(slit) and 3D(circular and rectangular) geometries

Going from the transition regime to the free molecular regime ($0.2 \leq Kn \leq 10$), the flow through circular and rectangular channels can be approximated using the results of 2D simulation (flow through slit) with a given flow rate, since the 2D results can be corrected using the effects of the ratios U_{max}/U_{avg} , and U_{slip}/U_{max} shown before. Figure 3.15 shows a correction factor of approximately 1.5 times bigger for a rectangular channel compared to a circular channel. This difference is mainly caused by the fact that the cross sectional area for the circular channel (with diameter H) and rectangular channel (with height

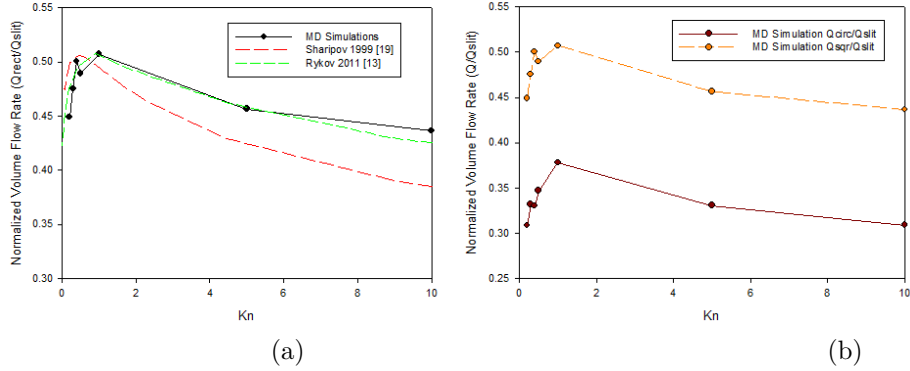


Figure 3.15: (a) Volume flow rate of rectangular(square) channel/volume flow rate of slit. (b) Volume flow rate of circular/rectangular(square) channel/volume flow rate of slit. Thermal wall boundary condition is used.

and width H) are about a factor 1.3 different.

3.3.6 Effects of the accommodation coefficient on the average velocity

For a rarefied gas, the accommodation coefficient α plays a bigger role for the flow rate than for a dense gas. In this research, the effects of the channel geometry on the effective accommodation coefficient will be studied. In Figure 3.16, the velocities are normalized with the maximum velocity. For all three geometries, the velocity profile in case of thermal wall condition gives narrower shape profile compared to diffusive- specular wall condition. Thermal wall condition represents a diffusive-specular wall with a tangential momentum accommodation coefficient of 1.0. Vice versa, reflective wall condition is a diffusive-specular wall condition with an accommodation coefficient of 0. Diffusive-specular wall condition with an accommodation coefficient of 0.5 can be interpreted as an intermediate point between flat profile and narrow profile as resulted by thermal wall condition. Absolute velocity and slip velocity show comparable differences between the two wall conditions. Diffusive-specular wall condition has higher velocity as half of the tangential momentum is conserved. The difference in velocity profile between the two conditions is larger in case of $50nm$ diameter channel compared to $100nm$, as the boundary effect has a bigger effect on the system when the channel size is small.

The average flow velocity (directly proportional to the gas volume flow rate) at $Kn = 5.0$ for nanochannels with height $H = 50nm$ is plotted as a function of the accommodation coefficient in Figure 3.17. The computations are performed for three different geometries: circular, rectangular, and slit channels. The results are fitted with allometric equations with a reduced Chi-Squared value all less than 1.01 for the three geometries. They are derived using Origin 8.5

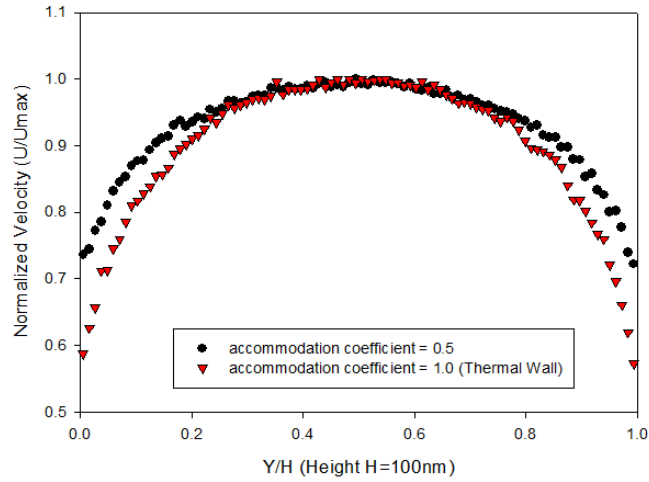


Figure 3.16: Velocity profile in a slit channel with height $H = 100nm$ and $Kn = 5.0$, in case of diffusive-specular (accommodation coefficient=0.5) and thermal wall boundary condition.

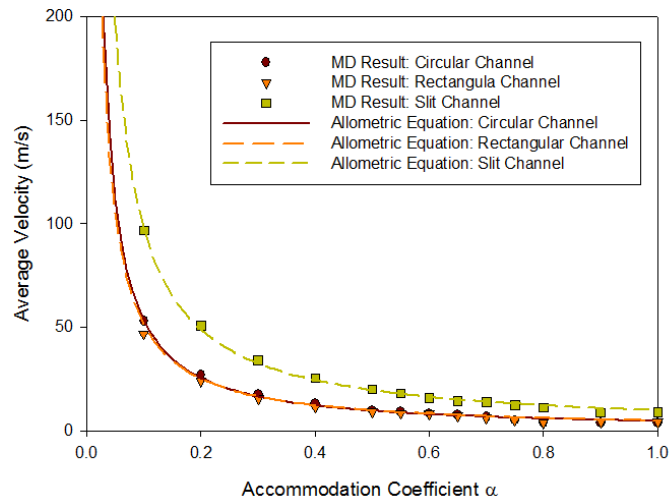


Figure 3.17: Average flow velocity as function of accommodation coefficient α at $Kn = 5.0$

Software^[4]. The allometric equations are as follow:

$$U_{avg,circular} = 4.079 \times \alpha^{-1.168} \quad (3.6)$$

$$U_{avg,rectangular} = 4.520 \times \alpha^{-1.017} \quad (3.7)$$

$$U_{avg,slit} = 9.9152 \times \alpha^{-0.992} \quad (3.8)$$

It is seen that the values for the constant and scaling exponent for rectangular channel is in between the values of circular and slit channel. The scaling exponents represent the sensitivity of an average velocity to accommodation coefficient. Among the three channels, the circular channel is the most sensitive to the accommodation coefficient while the slit is the least sensitive. This result is understandable considering the fact that surface to volume ratio of a circular channel is the largest. As it did for U_{max}/U_{avg} ratio, scaling exponent of rectangular flow and slit flow are much closer compared to circular flow.

To verify our MD simulation results, solutions from Bhatnagar-Gross-Krook (BGK) model are used for comparison. Suetin et al.^[152] analyzed, for a circular Poiseuille flow, the limiting cases of free molecular nondimensional volume flow rate Q . The following non-dimensional gas volume flow rates are obtained:

$$Q = \frac{2 - \alpha}{\alpha} \frac{8}{3\pi^{1/2}}. \quad (3.9)$$

Sharipov^[139] proposed the following equation based on the recent study of BGK model and diffuse-specular kernel:

$$Q = \frac{\pi^{1/2}}{2} \frac{2 - \alpha}{\alpha} (1 + 0.3166\alpha). \quad (3.10)$$

A formula for the non-dimensional gas volume flow rate has also been obtained by Cercignani & Pagani^[31]:

$$Q(\alpha) = Q(1) + \frac{\pi^{1/2}(1 - \alpha)}{\alpha}. \quad (3.11)$$

In order to compare the results from the MD simulation and BGK equations, normalized average velocities are calculated. Since volume flow rate is simply division of an average flow velocity by area, average velocity of our MD simulations can be compared with the BGK equations stated above. In Figure 3.18, the average velocity is normalized with the average velocity when accommodation coefficient $\alpha = 1.0$. Also the allometric equations and BGK equations are shown. Figure 3.18 shows that the fittings by all the models generally matches well with the MD simulation results. Among the BGK equations, Cercignani & Pagani model shows the best fit which give the smallest reduced Chi-squared value (1.15).

The allometric equation which we have used to compare three geometries gives a better fitting than the BGK equations when accommodation coefficient is lower than 0.70. However, it is not as accurate as the BGK equations for

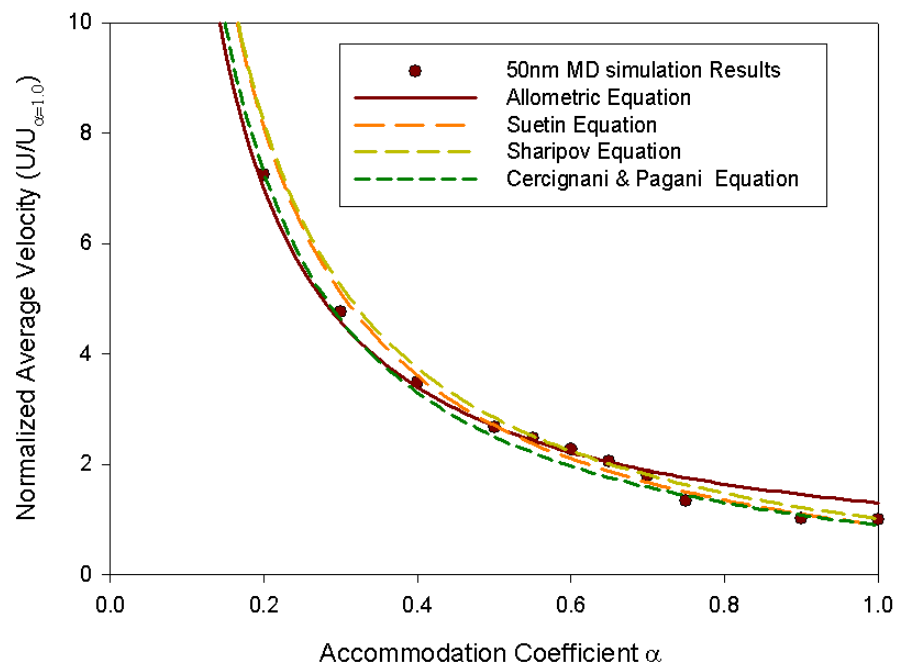


Figure 3.18: Normalized average velocity as function of accommodation coefficient α at $Kn = 5.0$ for a circular channel geometry

the region where accommodation is higher than 0.75. Overall it has a smaller reduced-Chi squared value (0.78) than the BGK equations. If we consider accommodation coefficient α , a model parameter varying in the range between 0 and 1, we find that the exponent of the allometric equation can describe the sensitivity on α of the flow rate for each geometry.

3.4 Conclusion

In this chapter, a gravity fed flow method has been validated for the simulation of rarefied gas flow. By this method, the slip velocity of rarefied gas flow inside nano channels with different cross section geometries has been calculated for fully developed flows. The numerical data of fully developed flows covers a whole range of Knudsen numbers varying from the free molecular regime to the transition one. An analysis of the numerical data shows that (i) the velocity of the slit geometry shows 2 ~ 2.5 times higher maximum velocity compared to other two geometries; (ii) when Kn goes to infinity, our MD simulation results give estimated U_{slip}/U_{max} asymptotic values of 0.77 for slit, 0.67 for rectangular, and 0.64 for circular channel; (iii) the U_{max}/U_{avg} ratios for circular channel flows are around 1.2, while they are around 1.1 for slit and rectangular channel at high Kn ($Kn > 10.0$); (iv) 2D to 3D correction factor for the volume flow rate is 1.5 times bigger for a rectangular channel compared to a circular channel; (v) the effect of the accommodation coefficient on the average flow velocity for all three geometries can be expressed as an allometric equation model; (vi) the scaling exponent, which shows the sensitivity to accommodation coefficient, of rectangular channel is in between the two other channel types (vii) the sensitivity of circular channel is larger than for the other two geometries.

4

Geometry effects on choked subsonic nanochannel flows in the transition regime

A three dimensional Molecular Dynamics method is used to study the effect of different geometries for choked subsonic flows in nanochannels. Argon molecules are used. The study focuses on the transition regime and goes up to free molecular regime. The flow is driven by a pressure difference between the inlet and the outlet. The expansion flow at the outlet of the channel is accompanied by a temperature drop and a sudden increase in velocity. Causes behind the differences between the three different geometries (circular, rectangular and slit) and the two different situations (isothermal condition and heated wall condition) are analyzed and studied. The calculated velocity slip and temperature distribution are compared with analytical solutions derived from the Navier-Stokes equations, and with the results from Direct Simulation Monte Carlo (DSMC) simulations. The study shows that the channel geometry has an influence on the fluid dynamics and on the heat transfer behavior of the choked subsonic flows in nanochannels. It also shows that DSMC method can accurately predict both flow and heat transport phenomena in $50nm$ nano channel in the transition regime, with a smaller cell size than the typical cell size. There is some deviation between MD and DSMC near the inlet region and near the outlet region where the gradient is large.

Parts of this chapter are described in:

Kim, J., Frijns, A. J. H., Nedeá, S. V., and van Steenhoven, A. A. Effects of expansion flow in nanochannels. *Proceedings of the 3rd European Conference on Microfluidics (μ Flu'12), Heidelberg, Germany*, 182: 1-10, 2012.

and

Kim, J., Frijns, A. J. H., Nedeá, S. V., and van Steenhoven, A. A. Pressure calculations in nanochannel gas flows. *Journal of Physics: Conference Series - Proceedings of 1st European Conference on Gas MicroFlows (GASMEMS2012)*, 362:012020, 2012.

4.1 Introduction

Micro- and nanochannels are commonly encountered in micro- and nano electro mechanical systems (MEMS/NEMS). To enhance the design and the performance of such system it is required to achieve a deeper understanding of their flow and heat transfer behaviours. The gas flow characteristics at the macro and micro levels are not the same and the features of micromechanics require additional basic and applied research work. On micro and nano scale, the viscous forces are of the same order of magnitude as the inertial forces opposed to a macro-scale vessel where viscous forces are usually negligible compared to inertial forces. Therefore many phenomena such as velocity slip and temperature jumps have been observed^[65].

In practice, next to the fully developed case, in small nanochannels and nanopores, a developing flow condition is also observed. To understand the developing flow in a nanochannel, the rarefied gas flow in two dimensional geometries has been studied extensively using MD and DSMC^[53,104,132]. However, as we have found in the preceding chapter for fully developed flows, the solution of two dimensional models cannot fully describe the difference between the flows inside circular, rectangular and slit channels. Therefore, also in this section, we will consider a three dimensional MD simulation method to analyze these geometry effects on developing flows. Moreover, the DSMC studies^[53,104,132] focus on the slip regime, while our work covers from the transition regime to the free molecular regime.

For developing flows, we have chosen choked subsonic nanochannel flows in the transition regime to cover nanochannel simulations at the same size scale and conditions as used in nano hole experiments in the vacuum industry^[55,75]. To our knowledge, MD simulation of gas flows in such large flow domain is not common^[16]. An additional goal of this chapter is to see whether DSMC is applicable to nano scale and how the choices in cell parameters are needed to be made. In order to validate the DSMC method, MD is used as a reference method for comparison.

This chapter describes several geometric effects in a developing nanochannel flow. Firstly, we study the effect of geometry on the flow properties in case of an isothermal condition. Secondly, we elaborate on the heat transfer more deeply by applying a higher temperature to the boundary walls in order to compare the heat transfer effect on the flows inside the different geometries. Finally, we compare our MD simulations with a high order approximation, based on Navier-Stokes equations and DSMC simulations.

4.2 Methods

In this chapter, two different sets of simulation will be carried out. The first simulation set(section 4.3) will be focused on the nanochannel gas flow in the isothermal situation and the second simulation set(section 4.4) will be focused on the heat transfer situation with an elevated wall temperature.

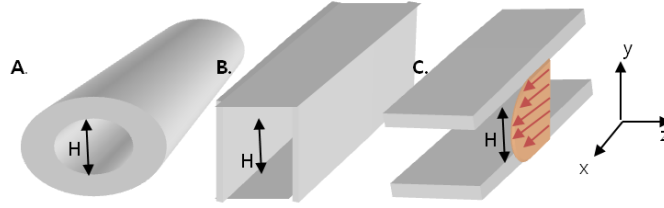


Figure 4.1: Three different nano-channels; A. Circular Channel, B. Rectangular Channel, C. Slit

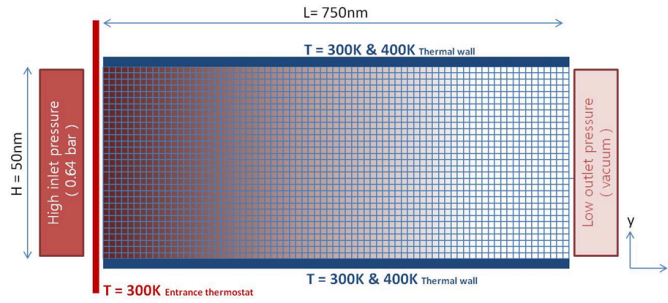


Figure 4.2: Developing nanochannel flow induced by the pressure difference.

For the two simulation sets, two simulation method are considered: Molecular Dynamics (MD) and Direct Simulation Monte Carlo (DSMC).

4.2.1 Molecular Dynamics

The Molecular Dynamics code PumMa^[2] is used here to study a developing flow inside the same three different channel geometries as for the fully developed simulations: a channel with a square or a circular cross section and a system with two parallel plates (slit geometry). The height or diameter H of the channel is $50nm$ (Figure 4.1). The characteristic length of this system is the separation distance H . It is comparable with the characteristic size of NEMS(Nanoelectromechanical systems) devices in engineering situations. In the flow direction (x direction), the channel length is kept at constant length $L = 750nm$.

Initially the Maxwell-Boltzmann velocity distribution at $300K$ is given to the molecules at the inlet. The channel walls are kept at a constant temperature $T_w = 300K$ for the isothermal simulation and at an elevated temperature of $T_w = 400K$ for the heat transfer simulation.

A thermal wall boundary condition is also applied as boundary condition in this research^[119,177]. For most experimental situations, the accommodation coefficient α is positioned between 0.95 and 1.0 (thermal wall)^[139]. In Chapter

3, it is shown that the normalized average flow velocities are hardly dependent on the accommodation coefficient in this range. Since this section is focused on the geometry effect rather than on the wall-gas interaction, thermal wall boundary condition ($\alpha = 1.0$) is used. A periodic boundary condition is applied in the Z direction in case of the slit geometry.

The simulation box domain in the XY plane is divided in a 100×100 grid. 10000 bins are extended across the Z direction. The local properties are calculated in each bin.

Flow is induced by a pressure difference between the inlet and the outlet (Figure 4.2). The pressure of both inlet and outlet is controlled by the number of particles in the buffer region. The length of the buffer regions are $20nm$ each. The pressure in the inlet is set as $0.64bar$ and the outlet is set to be vacuum. Pressure is controlled by controlling the number of particles and temperature inside such buffer region. Outlet buffer is controlled to have a vacuum condition. For the inlet buffer, a thermostat is used to control the temperature. The number of particles is controlled by gradually increasing the number of particles to the inlet buffer until it reached the density for target pressure.

The time step is fixed to $\Delta t = 6.43fs$. A typical computation in our simulations requires 5,000,000 time steps to reach a steady flow. We needed about 55,000,000 additional time steps for computing the averaged macroscopic properties: flow velocity, pressure, temperature, etc.

4.2.2 Direct Simulation Monte Carlo

For comparison we have also studied the developing flow by the DSMC. Most studies on microchannel flow with a compressibility effect used the DSMC method^[53,104,132]. Using the Puma DSMC code described in Chapter 2, DSMC simulations are performed for two geometries: the circular and the slit geometry, since the circular and rectangular channels show a similar behavior. These results are compared with our MD simulation results for the transition regime.

In our DSMC code, the molecules are modeled with hard sphere particles, and collision between particles are stochastic. Because attracting forces between molecules are neglected, only gases can be simulated. The stochastic collisions however make the method significantly faster than Molecular Dynamics.

DSMC is a good method for the high Knudsen number regime. However, it is not widely used for nanochannel flows but often used for microchannel flows. For micro channel flows, there have been several studies regarding the DSMC parameters (mean molecular number per cell and the cell size regarding mean free path). The recommended minimum molecular number per cell, $N_{c,min}$, is between 4 and 30^[87,92]. It is necessary to ensure that the cell size is less than $1/3$ of molecular mean free path in areas where the gradient is large, and less than $1/2$ in other areas^[154]. Two different cell dimensions that satisfy these recommendations are tested in order to check these recommended parameters are still applicable to the nanochannel.

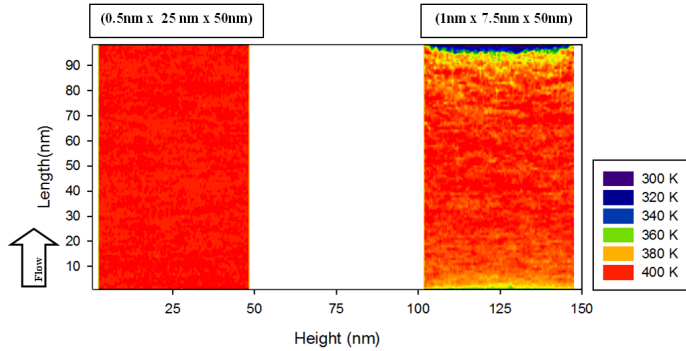


Figure 4.3: DSMC simulation (slit geometry) for heat transfer case with two different cell sizes: left ($0.5\text{nm} \times 25\text{nm} \times 50\text{nm}$) and right ($1\text{nm} \times 7.5\text{nm} \times 50\text{nm}$).

In principle, it is possible to simulate whole range of weighting factor (ratio of real and simulated particles), smaller than 1.0 and larger than 1.0, with DSMC. However, there is a practical problem. PumMa DSMC is developed such that weighting factor ≥ 1.0 . In this case, it is hard to find a good cell dimension in nanochannel to satisfy both molecular number per cell and mean free path. Often the cell size becomes larger than the recommended size ($1/3$ of molecular mean free path) to match the minimum particle per cell (4 to 30). In case of a microchannel, these limiting parameters do not cause any problem since it has enough space compared to nanochannel.

For the slit geometry, two different cell dimensions ($\Delta x, \Delta y, \Delta z$) are tried: ($0.5\text{nm} \times 25\text{nm} \times 50\text{nm}$) and ($1\text{nm} \times 7.5\text{nm} \times 50\text{nm}$). Both cell dimensions are in the scope of Sun's recommendation^[154]. However, the results (Figure 4.3) are very different: the simulation with the first cell dimension ($0.5\text{nm} \times 25\text{nm} \times 50\text{nm}$) does not show any temperature change in the gas while the simulation with the second cell dimension ($1\text{nm} \times 7.5\text{nm} \times 50\text{nm}$) works well. Since the gradient in the nanochannel is much larger than in most of the DSMC studies, the ratio of cell size to mean free path should be taken much smaller than for a microchannel. ($1\text{nm} \times 7.5\text{nm} \times 50\text{nm}$) cell dimension is chosen for our study. For the circular geometry, a cell dimension ($\Delta x, \Delta r$) of ($0.5\text{nm} \times 7.5\text{nm}$) is used. With this cell dimension, the number of molecules per cell in most cells is within the recommended minimum molecular number per cell (4 to 30)^[87,92]. However, PumMa is using a uniform grid system and some cells near the outlet have less than 3 molecules in a cell for our DSMC simulations.

A thermal wall condition ($\alpha = 1.0$) is used as boundary condition for DSMC simulations. This is the same as for the MD simulations. A periodic boundary condition is applied in the Z direction in case of the slit geometry.

The initial configuration of DSMC particles is taken from the MD simulations to speed up the DSMC calculation. The time step is fixed to $\Delta t = 6.43\text{fs}$. The time step is chosen to be smaller than the mean collision time. A typical computation in our simulations required 10,000,000 time steps to reach a steady

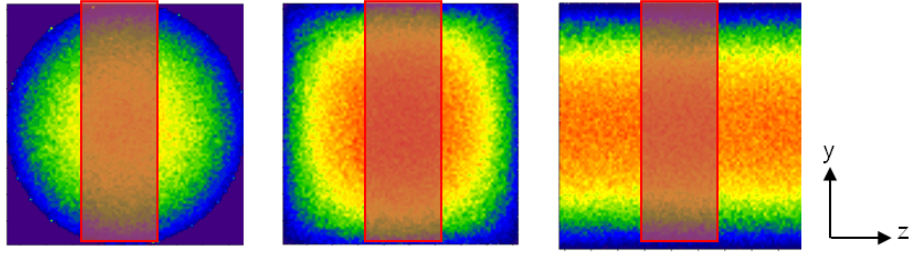


Figure 4.4: Contour velocity profile of 3 different geometries: circular, rectangular, slit channel. Red box indicates region where the velocity profile is determined. Velocity scale ranges in the order of red(high), yellow(Medium), blue(low), but the geometries have different values for each color.

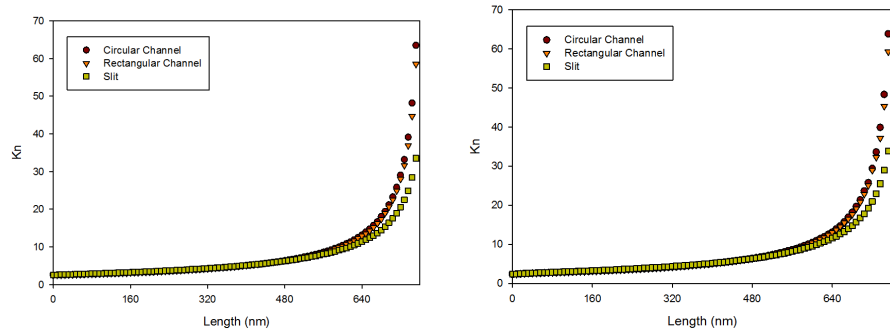


Figure 4.5: Knudsen numbers for different geometries along the channel length. Simulations with a wall temperature of $300K$ (left) and a wall temperature of $400K$ (right)

flow. We needed about 40,000,000 additional time steps for computing the averaged macroscopic properties: flow velocity, pressure, temperature, etc.

4.2.3 Sampling

In our simulations on developing flows, we have divided the whole channel height into 100 bins to compute space and time averaged velocities in x -axis. The segmental width of each bin is $0.5nm$. The velocity profiles in x direction, obtained by our simulations, are shown in Figure 4.4. In case of rectangular geometry the sampling only took place in the center part of the channel (Figure 4.4) as it is also done for the fully developed flow study. So it does not represent the whole velocity profile but only the center part.

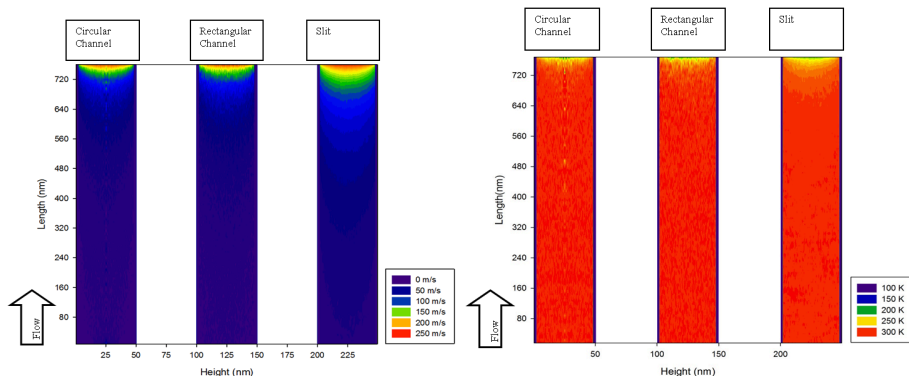


Figure 4.6: Velocity contour(left) and temperature contour(right) using MD for different geometries in isothermal flow(wall temperature $300K$). $H = 50nm$.

4.3 Expansion flow with an isothermal wall condition (wall temperature $300K$)

Firstly, the isothermal case is studied. The wall temperature and inlet flow temperature is kept at a constant value of $300K$. Inlet pressure is set at $0.64bar$ while the outlet pressure is near vacuum. Figure 4.5 shows that the flows for different geometries cover the transition regime and the free molecular regime. Figure 4.6 shows the contours of the stream wise mean velocity magnitude(left) and temperature profile(right) for all geometries which are analyzed with MD.

4.3.1 Pressure

As mentioned in Chapter 2, the pressure calculation in MD is mostly done by using the Irving-Kirkwood method^[76]. However, for rarefied gas situation, the effect of virial component becomes negligible (see Appendix A). Since the Irving-Kirkwood method requires a high cut-off radius simulation which is computationally very heavy, we suggest to use an equation of state(Virial equation of state, Peng-Robinson equation, Van der Waals equation etc.) or the ideal-gas law to calculate the pressure in this regime.

The virial equation of state (see Equation 2.23) is used here in the study. Second virial coefficient ($B_2 = -2972.592 [\sigma^6 bar]$) is taken from the work of Leonhard et al.^[99].

In the pressure calculation, also the boundary effect needs to be taken into account. As we use an implicit boundary condition, no material is modelled beyond this boundary. Therefore an artificial vacuum lies outside the channel boundary. This is one of the main causes of a smaller absolute virial component value compared to static MD simulation results. However, for the rarefied gas situation in a $50nm$ nanochannel, this effect is negligible and the use of the virial equation of state is acceptable (see Appendix A).

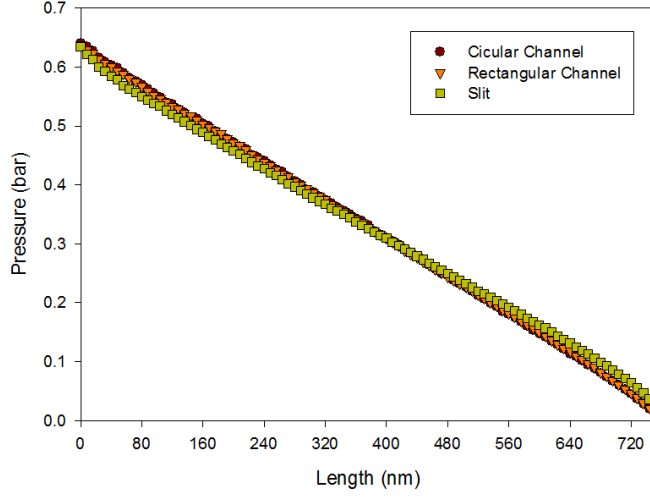


Figure 4.7: Pressure profile along the channel for different geometries using MD for isothermal condition along the channel length. $H = 50nm$.

A nonlinear pressure distribution along the channel is a well known characteristic of compressible microchannel flow. However, the curvature is more pronounced for the no-slip compressible flows than for rarefied flows. This is for example shown in the experiment of Pong^[125] and other DSMC simulations^[140,176]. In our MD simulation, all three geometries show a practically linear distribution along the channel. Figure 4.7 shows the evolution of the calculated pressure along the channel. However, while the circular channel and rectangular channel show a linear pressure profile over the whole channel length, the slit geometry shows a nonlinearity in the entrance region and exit region.

4.3.2 Velocity

The velocity results of isothermal case are shown in Figure 4.6 (left). The flow velocity increases as it develops downstream. Partly due to the high-pressure gradient the flow speed at the exit shows a sudden increase near the outlet. Figure 4.8 shows the variations of the gas velocity along the centerline(left) and the gas slip-velocity along the wall(right). It is seen that the slip-velocity increases as the flow develops downstream. The centerline velocity and the slip velocity are the largest in the slit while they are similar in the rectangular channel and circular channel.

Based on this result, the ratio between the slip velocity and the centerline velocity for three geometries is calculated. Linear fitting is done for the MD results from $50nm$ to $650nm$ length where inlet and outlet effect is minimal. Figure 4.9 (left) shows that the ratio is the biggest for the slit, and the lowest

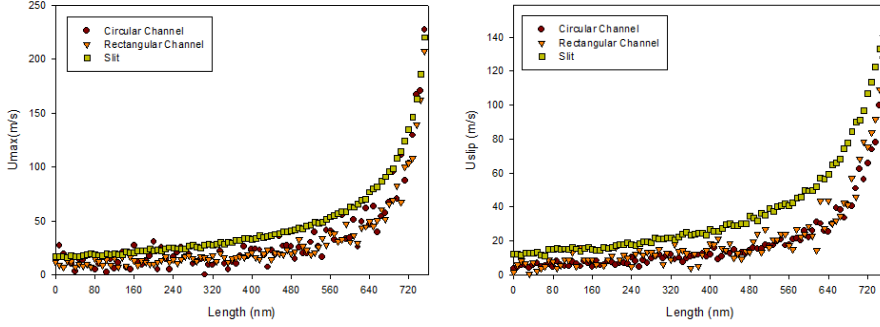


Figure 4.8: Centerline velocity (left) and slip velocity(right) of different geometries along the channel length, using MD. $H = 50nm$. Speed of sound for argon gas at $300K$ is $323m/s$.

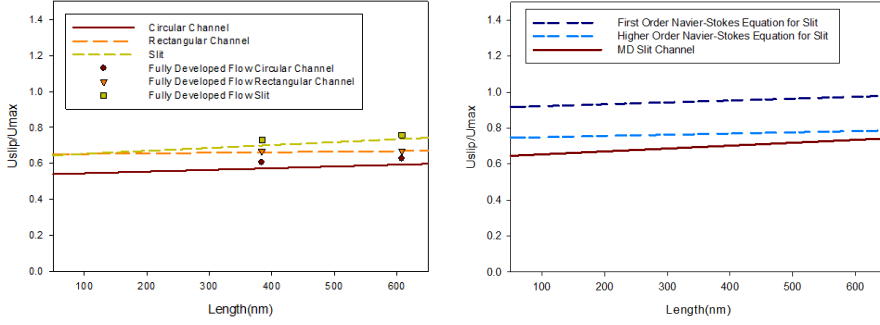


Figure 4.9: Ratio between slip and maximum velocity for 3 different geometries using MD(left), and Navier-Stokes models with first and high order slip velocities in a slit flow(right). $H = 50nm$.

for the circular channel. The velocity ratio of circular channel and rectangular channel is close to each other. This is similar to the observations made in a fully developed flow. The results of our fully developed flow in Chapter 3 show slightly higher ratios compared to the results for a developing flow. This slight difference can be explained from the slip velocity as was found in the fully developed flow chapter (Chapter 3) which is calculated based on the 2nd order polynomial fitting. In the fully developed flow study, the slip velocity calculated by molecular dynamics gives approximately 90% value of the slip velocity found by a polynomial fitting regardless of geometry and Knudsen number. In this chapter on developing flow, the slip velocity is not fitted, but directly taken from molecular dynamics calculation.

In Figure 4.9 (right), the wall-slip velocity as given by equation 3.3 and equation 3.4 are compared with the MD simulation results for a slit. The Knudsen

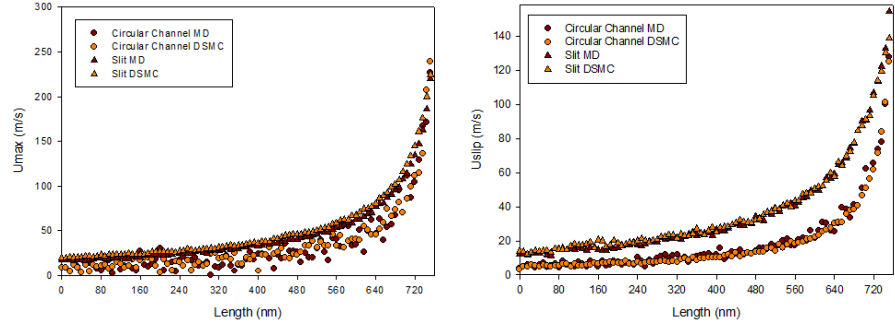


Figure 4.10: Centerline velocity (left) and slip velocity(right) along the channel length, for isothermal case for MD and DSMC. $H = 50nm$.

number of the slit increases from 2.5 (in the entrance region) to 33.5 (in the exit region) as shown in Figure 4.5. Since the local Knudsen numbers in the entire nanochannel are large, the Navier-Stokes based analytical values did not agree well with the MD results. In fact, Figure 4.9 (right) shows that the first order approximation is no longer valid, producing a velocity slip significantly higher than both the MD result and the high order analysis.

DSMC simulations are also performed for slit and circular channels. It is found that the centerline velocity of DSMC is slightly higher than MD, while slip velocity is nearly identical to each other. Therefore U_{slip}/U_{max} ratio is slightly lower for DSMC compared to MD.

By Chapman-Enskog theory, the dynamic viscosity, μ , of a pure monatomic gas of molecular weight, m , may be written in terms of the Lennard-Jones parameter as

$$\mu = \frac{5}{16} \frac{\sqrt{\pi m k T}}{\pi \sigma^2 \Omega_\mu} \quad (4.1)$$

where Ω_μ is dependent of epsilon value of the Lennard-Jones parameter^[21]. Therefore MD and DSMC molecular models have different viscosity values, which cause different slip velocities. It often causes a large difference in the simulated velocity calculated by MD and by DSMC, when a flow inside a small nanochannel with a large friction is simulated. However, it is found that MD and DSMC give a nearly identical slip velocity (Figure 4.10) in the transition regime when a channel of $50nm$ diameter is used.

4.3.3 Temperature

In order to calculate the temperature, the average velocity of each bin is calculated first as explained in chapter 2. The temperature of the bin is calculated by using the peculiar velocity of each particle that is computed based on the average velocity of each bin.

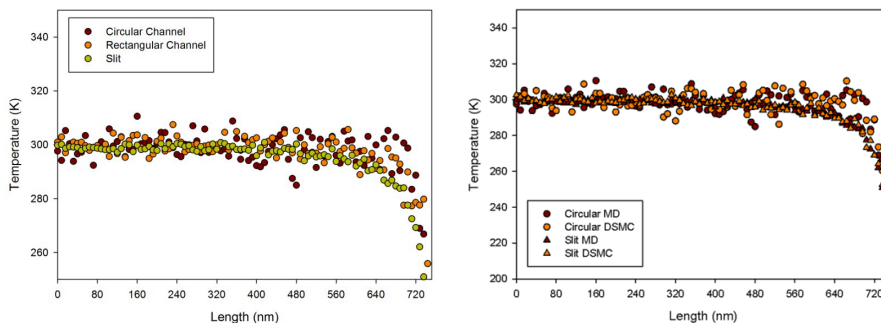


Figure 4.11: Centerline temperature of 3 different geometries along the channel length using MD(left), and centerline temperatures along the channel length using MD and DSMC(right). $H = 50nm$.

The temperatures in the different geometries are shown in Figure 4.6 (right). For all three geometries, there is a large decrease in temperature as the flow develops towards the exit. This is due to the strong expansion occurring at the channel outlet. Since the acceleration is more pronounced at the channel centerline, the temperature reduces there more rapidly. In the same manner temperature reduces the most in the slit channel consistent with the velocity results shown in Figure 4.6 (left).

Figure 4.11 (left) shows the centerline temperatures in the three different geometries. Temperature drop starts the earliest in the slit around $x = 620nm$, while it starts the last in the circular channel around $x = 700nm$. Figure 4.11 (right) shows a comparison between MD and DSMC for the temperature prediction. The results are nearly identical to each other even near the outlet region, where temperature drop starts.

4.4 Expansion flow with heated walls (wall temperature $400K$)

For the heat transfer simulation, the inlet flow temperature is kept at a constant value of $300K$. The channels are kept at a higher temperature at $400K$ with a thermal wall boundary condition.

As the results for velocity and pressure are similar to the previous section, those results are shown in Appendix B. Here we will focus on, in particular, temperatures close to the wall and corresponding heat fluxes.

The flows, with a higher wall temperature ($T_w = 400K$), are seen to have an increase of temperature as flow develops near the inlet of the channel. This is likely to be caused by the temperature difference between the wall and the flow. However, the contours (Figure 4.12) show a subsequent decrease of temperature in the downstream half of the nanochannel which is also shown in the isothermal

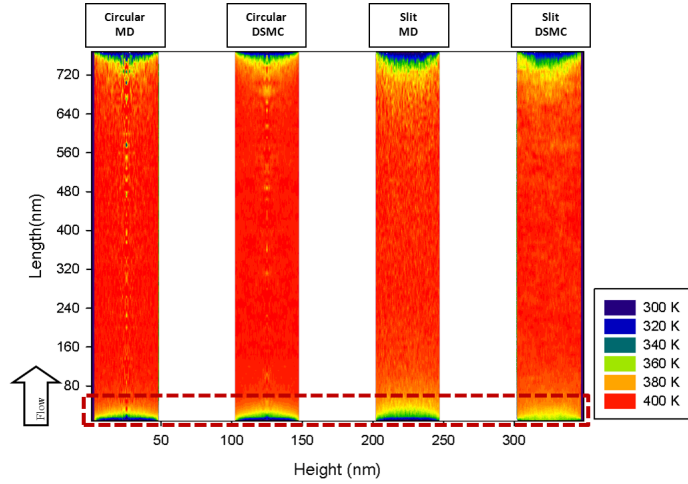


Figure 4.12: Temperature contour for circular channel and slit in heat transfer flow (wall temperature $400K$) using MD and DSMC. $H = 50nm$.

situation.

The centerline temperature along the channel is given in Figure 4.13 (left). The noise level in the circular channel is higher than in the other two geometries near the centerline, due to the decrease of sampling area and therefore a decrease in the number of molecules. The difference between T_w , the wall temperature, and T_g , the gas temperature near the wall, also called temperature-jump, for three different geometries are given in Figure 4.13 (right). For all three cases, there is a gradual decrease of the heat transfer from the wall to the fluid due to an increase in the gas temperature and thereby decreasing the convective heat transfer. In the second half of the channel, the temperature-jump (gas-wall) shows a significant increase in absolute value as the flow develops towards the exit. This is probably caused by a decrease in gas temperature due to the expansion flow.

The difference between MD and DSMC simulation results can be observed near the inlet region (red dashed box in Figure 4.12) for the heat transfer flow. Figure 4.12 shows the temperature contour for circular channel and slit in heat transfer case (wall temperature $400K$) using MD and DSMC. It is not possible to observe a gas temperature of $300K$ near the inlet region of the slit channel which is calculated by DSMC, while it is observable in the result by MD. However, a deviation has been found for gas temperature distribution at the inlet of the circular channel between MD and DSMC. This is probably because the cell sizes in x direction of DSMC method are different in slit geometry ($1nm$) and in circular geometry ($0.5nm$). The differences are more evident in Figure 4.14. This figure shows a comparison between MD and DSMC simulation results for centerline temperatures. It shows a higher DSMC/MD ratio near the entrance region compared to the other regions.

Geometry effects on choked subsonic nanochannel flows in the transition regime

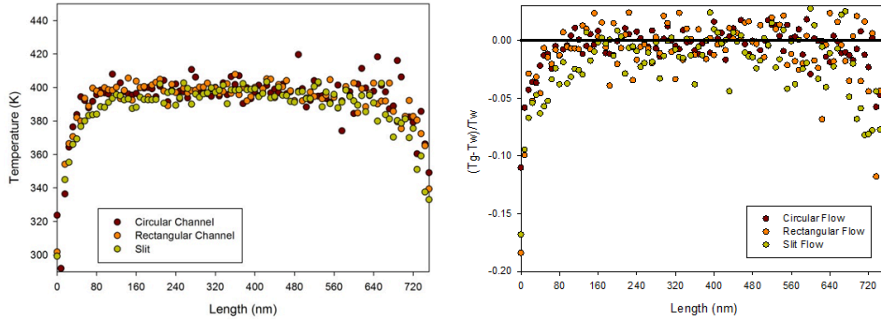


Figure 4.13: Centerline temperature along the channel length for 3 different geometries(left), Non-dimensional gas-wall temperature difference(right) using MD. $H = 50nm$.

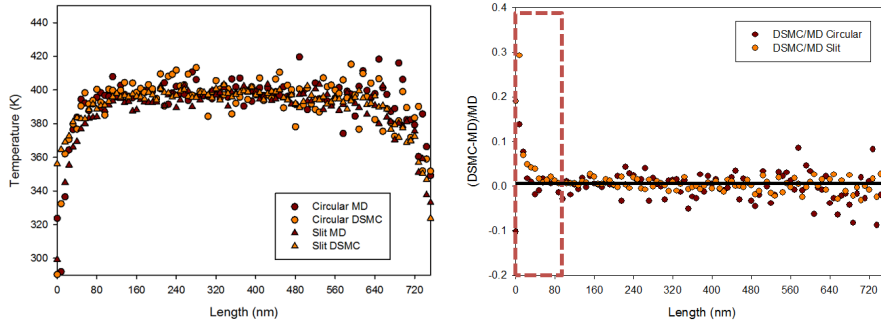


Figure 4.14: Centerline temperatures along the channel length using MD/DSMC(left)and relative DSMC-MD difference for centerline temperatures along the channel length(right). $H = 50nm$.

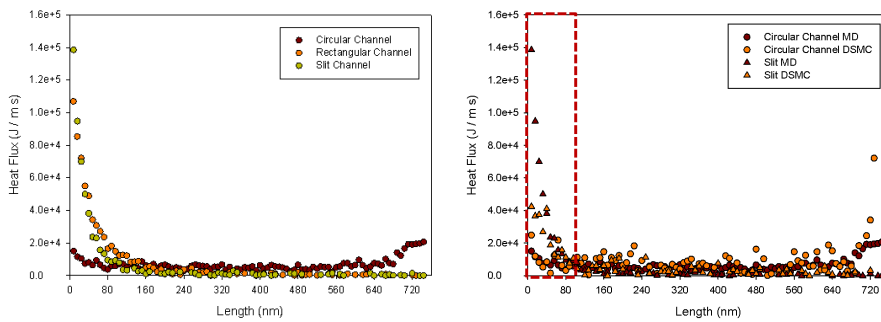


Figure 4.15: Heat flux along the channel length using MD(left) and heat flux of MD/DSMC(right). $H = 50nm$.

The heat flux at the wall is shown in Figure 4.15. The heat flux is calculated from

$$q_w = \frac{\sum \epsilon^i - \sum \epsilon^r}{A\Delta t}, \quad (4.2)$$

where $\sum \epsilon$ is the sum of the averaged molecular energies, A is the area, Δt is the interaction time and i and r stand for the incidence and reflected molecules respectively^[132]. Since argon is a monatomic gas, only the kinetic energy of the particle is considered for the calculation of molecular energy. Whole channel boundary is taken for the heat flux calculation.

Near the entrance region, there is significant transfer of heat from the wall for all three cases due to the high wall temperature. The heat flux decreases the fastest for a circular channel and the slowest for a slit. As the flow develops downstream the wall heat transfer diminishes and the difference between the geometries falls within the statistical error. The results suggest that the flow expansion observed near the channel exit is nearly adiabatic for all geometries, despite the finite temperature-jump at the wall. This is particularly true for the slit and the rectangular channel. Recall that the gas temperature near the exit for slit is lower than that for other geometries. It suggests that, for the slit and rectangular channel, the large temperature difference between the wall and the flow is not accompanied by any significant amount of wall heat transfer.

In case of circular channel, a small heat flux near the outlet is seen, due to the higher heat transfer rate corresponding to its highest boundary surface to volume ratio, while an increase in heat flux for the other two geometries is hardly seen.

Figure 4.15 (right) shows the comparison of the heat flux calculation by MD and by DSMC. As for temperature distribution, DSMC results of the circular channel agree more closely with MD than slit near the inlet of the channels (red dashed box in Figure 4.15). But, even with a smaller bin size in x direction, circular geometry shows a deviation in outlet region, where expansion flow occurs.

However, there is no clear difference between MD and DSMC calculations for centerline temperatures near the outlet region. A deviation in MD and DSMC calculations is found in the temperature profile near the outlet region (Figure 4.16). This figure shows a polynomial fitting of the temperature along the channel height. It shows that the temperature is similar in the center but different near the wall.

4.5 Conclusion

In this chapter, we have used MD to simulate developing flows in nanochannels. We have investigated a subsonic flow with choking in nanochannels that are subject to two different wall temperature boundary conditions. For the isothermal case ($T_w = T_{inletgas} = 300K$), it is observed that the slit channel is more sensitive to the outlet effects compared to the other geometries with a circular

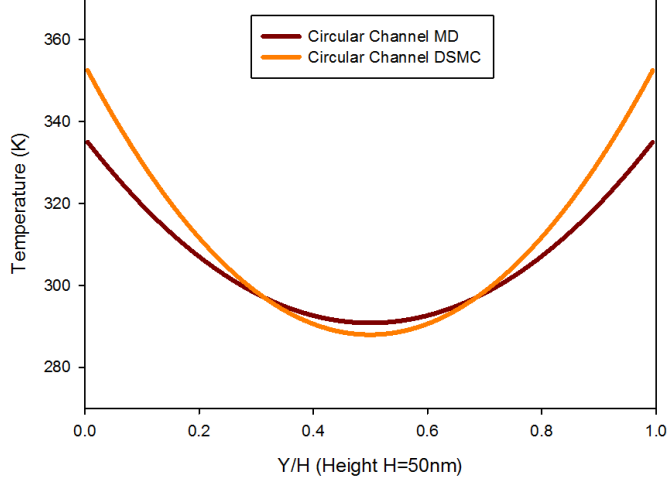


Figure 4.16: Temperature profile for circular channel along the height of the channel near the outlet region ($x = 745nm$) in heat transfer flow (wall temperature $400K$) using MD and DSMC. $H = 50nm$.

or rectangular cross-section. The low surface to volume ratio augments the non-linearity in axial pressure distribution. It is also observed that slip to maximum velocity ratios of three geometries is the largest for the slit, and the lowest for circular channel.

For the heating case ($T_w = 400K$ and $T_{inletgas} = 300K$) in developing flows, it is observed that gas heating increases the inlet and outlet effects in the channel. The hot wall enhances the degree of rarefaction and strengthens the influence of the entrance and outlet effect which confirms the findings of Tzeng et al.^[161].

It is shown that the DSMC method can accurately predict both flow and heat transport phenomena in a $50nm$ nano channel in the transition regime. However, it is found that the cell size should be chosen much smaller than the typical cell size ($1/3$ of molecular mean free path in areas where the gradient is large and less than $1/2$ in other areas for microchannels) to calculate accurate results. This is because the gradient inside the nanochannel is often much smaller than in a typical microchannel. As found for $50nm$ channel, there is some deviation between MD near the inlet region and outlet region where the gradient is large. In our simulations, this deviations are more clear for temperature than velocity.

5

Optimization of flexible three site water models

Molecular dynamics simulations of modified TIP3P models and a ReaxFF based tabulated water model are performed using the PumMa molecular simulation package. All simulations are carried out in the NVT ensemble. The characteristic liquid density ρ_l , self-diffusion coefficient D , oxygen-oxygen radial distribution function g_{OO} , oxygen-hydrogen radial distribution function g_{OH} , and hydrogen-hydrogen radial distribution function g_{HH} are determined and compared to experimental data. Modified TIP3P models are studied with different van der Waals cutoff radii and Columbic cutoff radii in order to optimize the physical parameters based on experimental data of liquid density for the temperature range of $300K$ to $600K$. Our new tabulated water model provides faster simulations than the other three site water models, and at the same time it provides a comparable liquid density and self-diffusion coefficient.

5.1 Introduction

In preceding chapters, the modeling of atoms and molecules is limited to non-polar cases, for instance, noble substance argon, where the Lennard-Jones potential can be applied reliably. However, for more practical applications (e.g. cooling, outgassing, etc), a study on more complex molecules like water is required. Water is the most widely used solvent in industry, and it has many special and unusual properties. Many of these special properties are due to hydrogen bonding^[81]. Theoretical methods are continuously being developed to describe the properties of water, especially for Molecular Dynamics. However, because of the mentioned complexity of the behavior of water and the accompanied difficulty of modeling this together with the required computational time, additional trade-offs are required. Many different potential functions for water have been developed over the last 30 years. Roughly speaking, the different models in use today can be distinguished by the number of sites (points of

charges or atoms) that are included in the model and the inclusion of flexible bonds : the water monomer can be treated as rigid or as flexible, allowing all degrees of freedom for the O-H bonds and HOH bond angle.

The simplest model has three sites, where the interaction sites correspond to the relative positions of the oxygen atom and the hydrogen atoms. All atoms have a charge, but only the oxygen atom has Lennard-Jones parameters. The most commonly used three sites models include SPC (simple point charge)^[18], SPC/E (extended simple point charge)^[17], and TIP3P (transferable intermolecular potential 3P) models^[85]. The difference between these models are the Lennard-Jones parameters that are used, the O-H bond length, and the HOH bond angle. Consequently the models predict different bulk properties and have different phase diagrams. There are also several models that use more than three interaction sites. The models that use four and five interaction sites introduce dummy atoms that carry the charge of the O-atom away from the O-atom itself. In doing so, the electrostatic distribution around the water molecule can be modelled more accurately. However, with the added sites the computational effort increases. The most popular four sites models are the TIP4P/2005^[5] or the TIP4P/Ew^[73]. TIP5P^[107] is the most popular model for the five sites model. All these models mentioned above put constraints on the length of the bonds and/or angles between the atoms. There are a couple of advantages doing so. The main obvious advantage is the maximum allowed time step size for the accurate integration of the equations of motion. The fastest motions in the water molecule are bond vibrations. Taking away this motion, by fixing the bond-length, allows an increase in the time step size. In these rigid models, the *SHAKE* algorithm^[133] is generally used to constrain the bond length. Despite their great simplicity, many properties of bulk water (e.g. liquid density, viscosity, diffusion coefficient, etc.), especially under normal conditions (300 K and 1 atm), are well reproduced by these models.

However, several studies also describe the advantages of flexible water models over rigid models in many aspects. The introduction of bond flexibility is a promising alternative strategy for providing models that allow for accurate simultaneous prediction of different properties, especially in non-ambient situation. The early work of Dang and Pettitt^[40] or Toukan and Rahman^[157] showed that flexible versions of three-site water models accurately reproduced certain aspects of the vibrational motions of neat water. Lopez-Lemus et al.^[115] have incorporated flexibility in the SPC/E model and demonstrated that the calculated surface tension and coexisting density of water predicted by the flexible model are closer to the experimental data than those of the rigid model. The flexible SPC/Fw model reported by Wu et al.^[175] has resulted in a noticeable improvement in the accuracy of the viscosity, diffusion coefficient, and dielectric constant predicted at ambient conditions compared to the rigid SPC model. Raabe and Sadus^[128,129] have adequately predicted the saturation density, diffusion coefficient at both ambient and supercritical temperatures over a wide range of pressures by using SPC/Fw model.

A final goal of the thesis is to simulate outgassing of water from a nanopore (see Chapter 7). The outgassing of especially water is a significant problem

in the creation and maintenance of ultra-high vacuum in the semiconductor industry^[86]. Simulating the outgassing rate with different parameters (material, structure) could improve the design and reduce the turnaround time for outgassing. Desorption and diffusion are two most important processes in outgassing. Liquid density and diffusion coefficient are the parameters that are directly related to these two processes. Outgassing is often carried out near the supercritical temperature over a wide range of pressures. Based on the advantages of flexible bonding mentioned above, we decided to use flexible water models for our study.

In this work, two different types of flexible three sites water models are studied. One is the flexible water model modified based on well-known TIP3P model which is optimized for temperature range from 300K to 600K, and the other is a tabulated water models which are optimized at one specific temperature. Our interest in this work concentrates on the self-diffusion coefficient D , and the liquid density of the water. As an extra property, the radial distribution functions of these models are also compared with the radial distribution functions of different existing three site models.

5.2 Simulation method

5.2.1 PumMa Molecular Dynamics

Simulation programs used for this study are PumMa^[2] and ReaxFF^[165,166]. PumMa is a conventional molecular dynamics simulation software, and ReaxFF is a reactive empirical force field simulation software. ReaxFF lies between conventional molecular dynamics and quantum mechanics. While conventional molecular dynamics simulates interaction of molecules described by an interaction potential with atoms constituting molecules through static bonds, in ReaxFF each atom is treated as a separate entity whose bond structure is updated at every time step. This dynamic bonding scheme together with charge redistribution is the strength of ReaxFF. Here ReaxFF is used for the calculation of the potential energy table for the tabulated water models which is used in PumMa.

PumMa has been used for researches in the area of nanoflow and heat transfer^[91,118]. It has several advantageous features for flow and heat transfer: it offers several controllers, and boundary conditions that are necessary for flow and heat transfer simulation. However, it also lacks some functions that are needed to retrieve the bulk properties of water. It does not offer Ewald summation^[51] that is important to calculated diffusion coefficient with periodic boundary conditions. PumMa also does not offer a constraint method. The lack of the constraint method in PumMa is one of the reasons to choose a flexible water model instead of a rigid water model for our study.

Our primary selection criterion for an appropriate water model is that it has the same degrees of freedom and employ the same potential form as used for the other macromolecules used in PumMa. Without such underlying con-

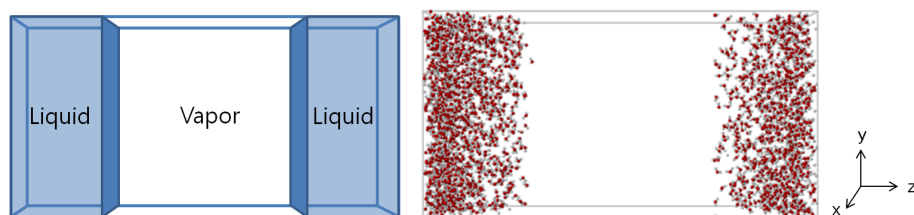


Figure 5.1: Liquid density simulation setup at start(left), and simulation snapshot for 300K (right).

sistency, unexpected and undetected systematic errors could be introduced into the simulations^[100].

5.2.2 Liquid density

As stated in the introduction, our main interested properties are the liquid density and the self-diffusion coefficient D of the water. In order to calculate liquid density, a rectangular box is used for the simulation domain as was studied by Shi et al.^[142]. Its dimensions are $3.2nm$, $3.2nm$, and $6.4nm$, respectively. The x , y , and z boundary conditions are set periodically. Initially a liquid slab is placed at the two sides of the simulation domain as shown in Figure 5.1. 800 water molecules are placed in the liquid region using a cubic crystal structure. The initial velocities of molecules are set to correspond the system temperature. No external force field is applied.

The cutoff radius of van der Waal's interaction and Coulombic interaction is fixed at $2.5nm$ for the tabulated water model, while they are varied for modified TIP3P models. 100 mesh points are used for the calculation of the liquid density. The simulations are carried out in an NVT ensemble. The system is equilibrated at a desired temperature for 100,000 time steps by velocity re-scaling. To calculate a liquid density, an additional 100,000 time steps are simulated. The density is calculated every 10 steps for averaging.

5.2.3 Self-diffusion coefficient

The self-diffusion coefficient of water is a time dependent parameter describing how well the water particles can mix among themselves. As a result of the force fields from nearby particles, particles will show random movements. These random movements of molecules through a fluid are called Brownian motion. Early work done by Albert Einstein yielded a correlation between Brownian motion and the self-diffusion coefficient D . The relevant formula is called the Einstein Relation^[9]:

$$\langle r^2(t) \rangle = 6Dt \quad (5.1)$$

Table 5.1: Simulation set for self-diffusion coefficient .

Temperature (K)	298	398	498
Density (kg/m^3)	997	939	829

where $\langle r^2(t) \rangle = \langle |r(t) - r(0)|^2 \rangle$, the squared displacement over time t . Rewritten this formula more directly states:

$$D = \frac{1}{6t} \langle |r(t) - r(0)|^2 \rangle. \quad (5.2)$$

Due to the randomness of the particle paths the diffusion coefficient is not constant but tends to fluctuate around a certain value. Self-diffusion coefficient is calculated from the mean square displacement (MSD) of atoms using the Einstein relation as the diffusion coefficient is a single particle property. The self-diffusion coefficient is estimated from the slope of the linear part at long times of the mean square displacements vs. time plot.

All different water models are compared using identical NVT simulations. The number of molecules is chosen such that the box is completely filled with liquid water. As the temperature increases, it becomes necessary to adjust the density to ensure that the pressure remains reasonable. We used the same set of densities and temperatures used by Levitt et al.^[100] for comparison. The simulation set for the self-diffusion coefficient calculation is shown in Table 5.1.

5.3 Water models

A water molecule consists of an oxygen atom bonded with two hydrogen atoms. For Molecular Dynamics simulations the bond length and the bond angle are two basic parameters that are required to describe the molecule (Figure 5.2). The atoms themselves can be regarded as point charges, with interacting forces resulting from the potentials (Table 5.2).

5.3.1 Modified TIP3P models

Introduction

First, flexible models, that are modified based on the TIP3P model, are studied. Two water models are studied and simulated. The first model was developed by Neria et al.^[120]. The second model, we developed, resembles in all respect except for the molecular diameter of oxygen atom, r_0^{OO} . We use the same diameter that is used for the original TIP3P model. Parameters for the models are shown in Table 5.3.

In this section, we compare calculated bulk properties for the modified TIP3P water models for the temperature between $300K$ and $600K$. All simulations are performed under exactly the same conditions and using the same

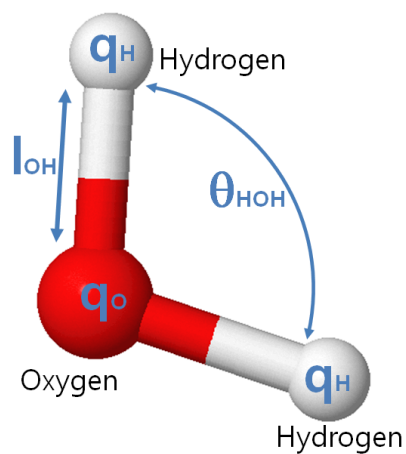


Figure 5.2: Flexible three site water model.

Table 5.2: Parameters of three-point water models(See Fig. 5.2) .

Parameter	Units
Molecular diameter r_0^{OO}	(nm)
Energy well depth ϵ^{OO}	(kcalmol ⁻¹)
Molecular diameter r_0^{HH}	(nm)
Energy well depth ϵ^{HH}	(kcalmol ⁻¹)
Molecular diameter r_0^{OH}	(nm)
Energy well depth ϵ^{OH}	(kcal mol ⁻¹)
Charge q^O	(e units)
Charge q^H	(e units)
Bond length l_0^{OH}	(nm)
HOH angle θ_0^{HOH}	(deg)
Bond spring constant K_l	(kcal mol ⁻¹ Å ⁻²)
HOH angle spring constant K_θ	(kcal mol ⁻¹ rad ⁻²)

Table 5.3: Nonbonded parameters, geometry and electrostatic properties of the modified three-point water models.

Parameter and unit	Original TIP3P	Mod. TIP3P Neria ^[120]	Mod. TIP3P Kim
r_0^{OO} (nm)	0.31506	0.315365	0.31506
ϵ_{OO}^O (kcal mol ⁻¹)	0.1521	0.1521	0.1521
r_0^{HH} (nm)	0	0.0449	0.0449
ϵ_{HH}^H (kcal mol ⁻¹)	0	0.046	0.046
r_0^{OH} (nm)	0	0.1993	0.1993
ϵ_{OH}^O (kcal mol ⁻¹)	0	0.084	0.084
q^O (e units)	-0.834	-0.834	-0.834
q^H (e units)	-0.417	-0.417	-0.417
l_0^{OH} (nm)	0.09572	0.09572	0.09572
θ_0^{HOH} (deg)	104.52	104.52	104.52
K_l (kcal mol ⁻¹ Å ⁻²)	-	450	450
K_θ (kcal mol ⁻¹ rad ⁻²)	-	55	55

system size. The system size is defined large enough to be used also in future simulations of micro and nano flow and heat transfer (e.g. outgassing of water from the nanopores). The nonbonded interactions are treated in two ways: Lennard-Jones, and truncated Lennard-Jones using force shifting, where the calculated forces and energies are smoothly shifted to zero at the cutoff distance. In this section, we will call Lennard-Jones as non-truncated Lennard-Jones in order to make a clear distinction with truncated Lennard-Jones. The cutoff radii are varied and tested to give similar structural and dynamic properties for bulk water when the water models are used in PumMa molecular dynamics package. We will compare the numerical results to the experimental data of Washburn et al.^[169], Krynicki et al.^[95], and Soper et al.^[146].

Cutoff radius

A number of studies^[109] have demonstrated the importance of long range electrostatic interactions. Inclusion of the longer range electrostatic interactions in a molecular dynamics simulation can be done by simply increasing the cutoff radius. In this section, the effect of cutoff radii is studied in order to optimize the modified TIP3P models for PumMa molecular dynamics package.

The effect of the van der Waal's cutoff radius is tested by comparing the simulation result of the non-truncated Lennard-Jones potential and the truncated Lennard-Jones potential with cutoff of 2.5σ . Three different Coulombic cutoff radii (1.0 nm, 1.5 nm, 2.0nm) are used here to test the effect of Coulombic cutoff. As shown in Figure 5.3 and Figure 5.4, both van der Waal's cutoff radius and Coulombic cutoff radius have big influences on liquid density and self-diffusion coefficient of water.

By increasing the van der Waal's cutoff radius, liquid density increases, while there is a minimal effect on the diffusion coefficient as shown in Figure 5.4(compare left figure with right figure). Opposite to van der Waal's cutoff, liquid density decreases by increasing the Coulombic cutoff radius. Simulation results show that diffusion coefficient is mainly influenced by the Coulombic

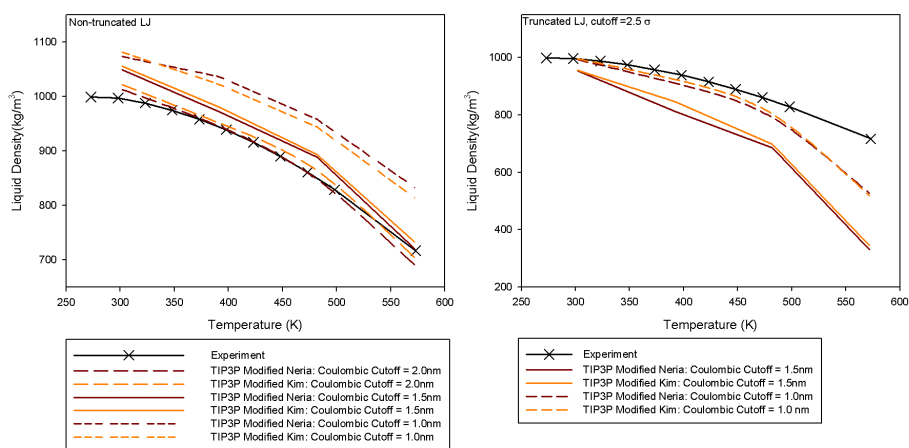


Figure 5.3: Liquid densities of water: Non-truncated Lennard-Jones(left) and truncated Lennard-Jones with cutoff= 2.5σ (right). Experimental values are from ref. ^[169]

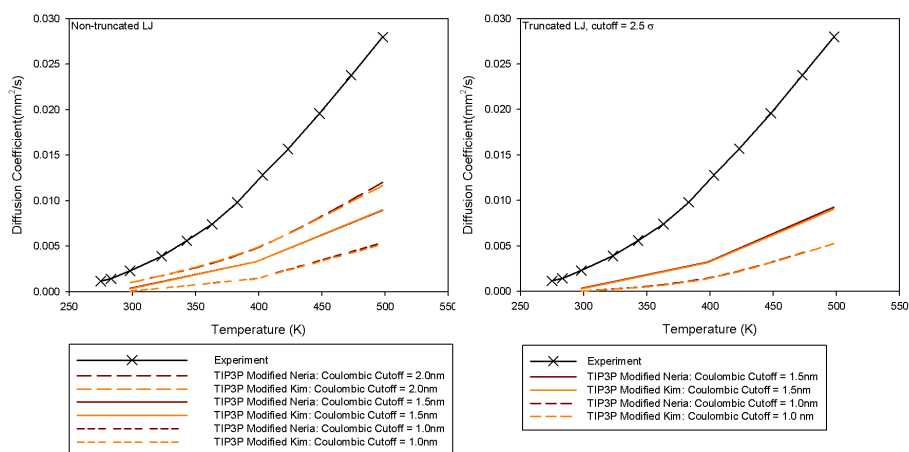


Figure 5.4: Self-diffusion coefficient of water: Non-truncated Lennard-Jones(left) and truncated Lennard-Jones with cutoff= 2.5σ (right). Experimental values are from ref. ^[95]

Table 5.4: Computation time to simulate 10 *ps* self-diffusion coefficient simulation at 300K on 1 CPU.

Model Type	van der Waal's cutoff	Coulombic cutoff	CPU time
Mod. TIP3P Neria	Non-truncated LJ	2.0nm	148053.09 s
Mod. TIP3P Neria	Non-truncated LJ	1.5nm	62563.34 s
Mod. TIP3P Neria	Non-truncated LJ	1.0nm	18348.48 s
Mod. TIP3P Neria	Truncated LJ 2.5 σ	1.5nm	61007.50 s
Mod. TIP3P Neria	Truncated LJ 2.5 σ	1.0nm	18600.64 s
Mod. TIP3P Kim	Non-truncated LJ	2.0nm	147244.89 s
Mod. TIP3P Kim	Non-truncated LJ	1.5nm	62563.34 s
Mod. TIP3P Kim	Non-truncated LJ	1.0nm	18749.28 s
Mod. TIP3P Kim	Truncated LJ 2.5 σ	1.5nm	62224.38 s
Mod. TIP3P Kim	Truncated LJ 2.5 σ	1.0nm	18469.57 s

cutoff radius. By increasing the Coulombic cutoff radius, the self-diffusion coefficient increases and gets closer to the experimental value by Krynicki et al.^[95]. This experimental values was measured by the proton spin echo method.

However, increasing the cutoff distance can dramatically raise the computational cost. Table 5.4 shows that when Coulombic cutoff radius is increased from 1.0nm to 2.0nm, computation time is increased nearly 10 times. In the temperature range from 300K to 500K, a truncated model with 1.0nm Coulombic radius can be a better model to use for a simulation when the liquid density is the most important value. The model provides as good as the non-truncated Lennard-Jones potential and the 2.0nm Coulombic cutoff radius model and 10 times faster in same time. However, it is still recommended to use 2.0nm Coulombic cutoff radius model when diffusion coefficient is concerned.

Discussions on the modified water model

With the non-truncated Lennard-Jones potential and 2.0nm Coulombic cutoff radius, the liquid density values agree well with experimental results as shown in Figure 5.5. TIP3P modified by Neria gives better results near 300K compared to our modified TIP3P model. However, in the region near the critical temperature, the density of the liquid from simulation is lower than that of our model and the experimental data^[169]. The figure shows that both modified TIP3P models are not very accurate for the both ends of the temperature range: near 300K and 600K. However, the TIP3P model modified by Neria provides a reasonable temperature-density curve between 350K and 500K. Our modified TIP3P model can be used instead for the simulation with a temperature higher than 500K. Both model provides results within 5% error to the experimental data^[169].

Non-truncated Lennard-Jones potential and 2.0nm Coulombic cutoff radius provides the best self-diffusion coefficient values among different combinations of cutoff radii. However, as shown in Figure 5.6, both modified models do not

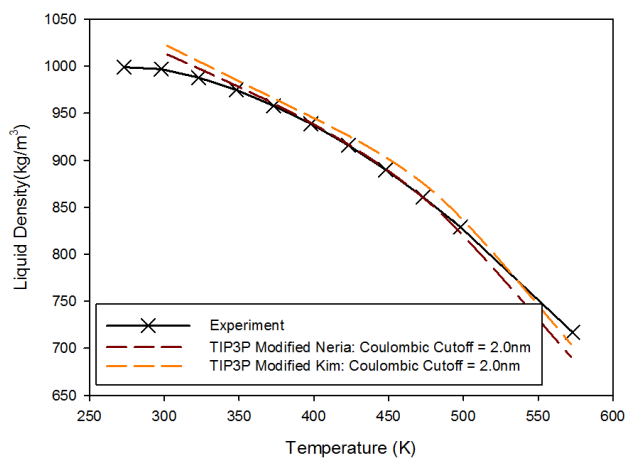


Figure 5.5: Liquid densities of modified TIP3P models: Non-truncated Lennard-Jones potential and $2.0nm$ Coulombic cutoff radius. Experimental values are from ref. ^[169]

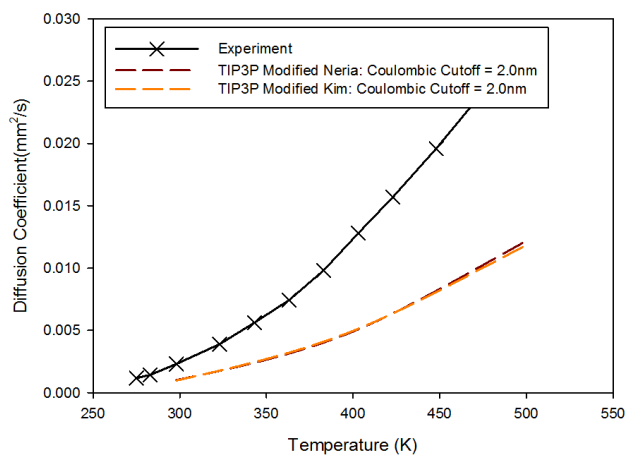


Figure 5.6: Self-diffusion coefficient of modified TIP3P models: Non-truncated Lennard-Jones potential and $2.0nm$ Coulombic cutoff radius. Experimental values are from ref. ^[95]

give an accurate diffusion coefficient at high temperature. Diffusion coefficients of modified TIP3P models are approximately half the experimental values^[95].

The Radial Distribution Functions of the modified TIP3P models, g_{OO} , g_{OH} , and g_{HH} are compared with experimental data^[146] in Figure 5.7. The Radial Distribution Functions are commonly used when the structure of the liquid water is studied. It describes how density varies as a function of distance from a reference particle. Our calculated radial distribution functions are overall in good agreement with the experimental data determined from neutron diffraction data by Soper et al.^[146].

Our modified TIP3P model gives closer agreement with experiment for g_{OO} than Neria’s model, but the second minimum and the third peak position occurs at slight further distance when compared with experiment. Both modified models have similar first peak position and overall structure as the experimental data, but the height of the peak is too high for the first peak and slightly lower for the other peaks. Both Neria and our modified model have very similar peak positions, overall structure, and peak height for g_{OH} . The first and the second peak occur much steeper when compared with experiment. Both models have higher first peak, and slightly higher second peak to experiment. Our modified TIP3P model again gives better agreement with experiment for g_{HH} . Both models have similar peak positions, but the overall peak height agrees better between our modified model and experimental data. Again, the first peak is much steeper and is much higher compared to the experiment. Both models agree well with the experimental data after the first minimum. As summary, the Radial Distribution Functions of both models have good agreement with the experimental data, but in overall our model gives a slightly better result.

5.3.2 Tabulated potential water model

It is shown in Table 5.4 that large computational times are required to simulate water molecules with a large Coulombic radius. Heat transfer and flow simulations often require much larger systems compared to the simulations of bulk properties of materials. Thus the computational time is even more important. In this section, we study whether we can develop a water model that could speed up the simulation further.

Tabulation process

A tabulated potential^[174] is often used to describe intermolecular interaction functions that are different from the usual Lennard-Jones or Buckingham type potential. Here in this study, we use the Reactive empirical force field (ReaxFF) method to derive the nonbonded interaction potential between the water atoms: H-H, O-O, and O-H to build a tabulated water model. Our tabulated potential model includes not only the van der Waals interaction but also the Coulombic charge interaction. Since all interactions can be calculated in one single reading of an interaction table, it can be faster than conventional models.

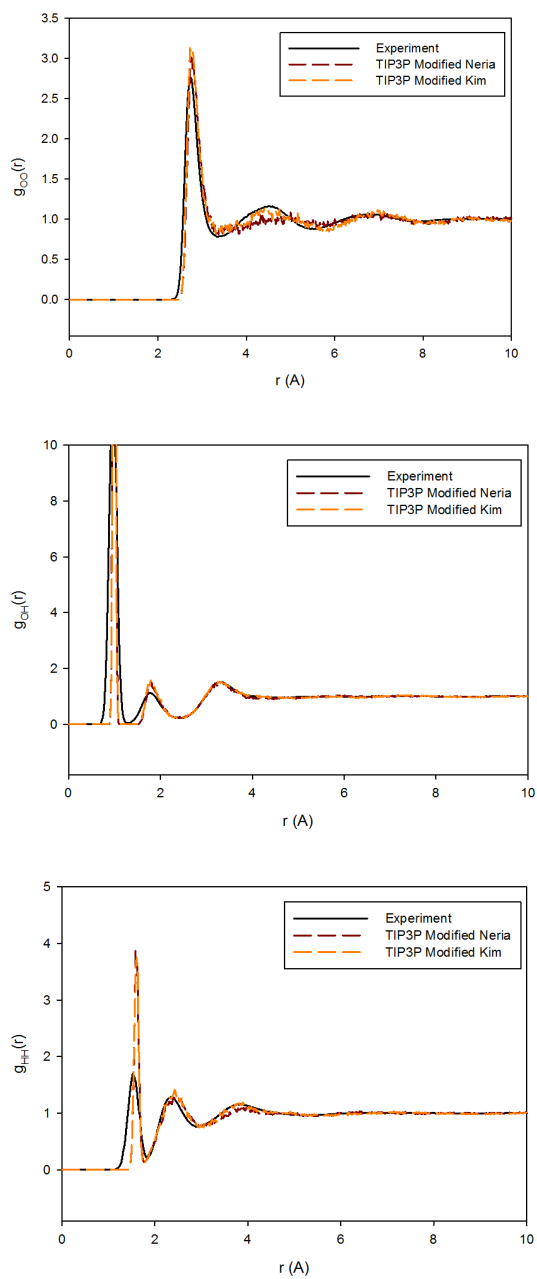


Figure 5.7: Radial distribution function of modified TIP3P models at $T = 298$ K (Liquid density = 998 kg/m^3): Non-truncated Lennard-Jones potential and $2.0nm$ Coulombic cutoff radius. Experimental values are from ref. ^[146]

Assume a water atom is at distance r from another water atom. In ReaxFF, energy of such system is calculated with the following parameters:

$$E_{system} = E_{bond} + E_{lp} + E_{over} + E_{under} + E_{val} + E_{pen} + E_{3conj} + E_{tors} + E_{4conj} + E_{H-bond} + E_{vdWaals} + E_{Coulomb} \quad (5.3)$$

where E_{bond} represents the bond energy, E_{lp} is the energy due to the presence of lone pair, and E_{over} and E_{under} are the energies arising from over and under-coordination, respectively, of atoms with respect to their valency. The valence angle (three-body) energies are accounted for in the terms E_{val} and E_{tors} , respectively. E_{pen} is a penalty energy to stabilize a three body system with the center atom having two double bonds connected to it. Conjugated chemical bonds are stabilized by adding corrections for three body, E_{3conj} , and four body, E_{4conj} , conjugation terms to the respective systems. E_{H-bond} represents the hydrogen bond interactions. The long-range interactions such as the van der Waals interactions, $E_{vdWaals}$, and the Coulombic interactions, $E_{Coulomb}$, are accounted for between every pair of atoms irrespective of the presence of chemical bonds^[80].

However, it is important to note that reaction parameter(E_{bond}) is not included when the interaction energy is calculated by ReaxFF for our water model, since we do not want to model chemical reactions, i.e. creating or breaking bonds. The distance between two atoms, r , is varied from 0 to the cutoff radius $2.5nm$. Potential energies at 1281 points within this cutoff range are calculated. Same process is repeated for different combination of atom types.

A fixed charge is used in the ReaxFF tabulation process. Tabulated water model is then built with this tabulated potential energy table, H-O bond length, HOH angle, and spring coefficients. The spring coefficients are taken from the modified TIP3P model developed by Neria et al.^[120]: $K_b = 450 \text{ kcal mol}^{-1} \text{ \AA}^{-2}$, $K_\theta = 55 \text{ kcal mol}^{-1} \text{ rad}^{-2}$. This tabulated potential energy table, produced through ReaxFF, is then put into PumMa as an input potential energy for each interaction.

Optimization by bond length

A bond length is the average distance between nuclei of two atoms in a molecule; in this case oxygen and hydrogen. A commonly observed bond length in three site water model for O-H bonds is $0.9572nm$ ^[108].

The bond length is changed to a set of values within the range of $0.07nm$ to $0.11nm$, which is still within the range of literature values. By increasing the bond length, liquid density increases as shown in Figure 5.8. This could be the result coming from more optimal packing by changing the dipole moment.

Increasing the bond length also reduces the temperature dependency of the density. The slope of the liquid density versus the temperature is clearly lower for the higher bond lengths.

The overall diffusion coefficient drops by increasing the bond length. However for higher temperatures, it shows that the maximum diffusion coefficient

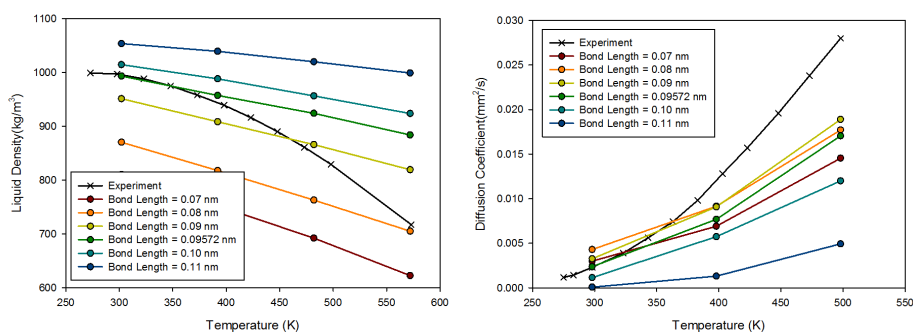


Figure 5.8: Liquid densities (left) and self-diffusion coefficients (right) of water models by varying the bond length. Experimental values for liquid density are from ref. [169]. Self-diffusion coefficients are from ref. [95].

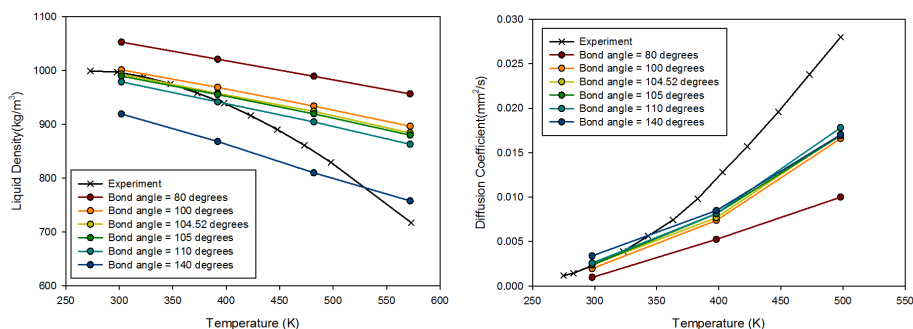


Figure 5.9: Liquid densities (left) and self-diffusion coefficients (right) of water models by varying the HOH angle. Experimental values for liquid density are from ref. [169]. Self-diffusion coefficients are from ref. [95].

happens with 0.9 angstrom bond length. The overall decrease in diffusion coefficient might be due to the increased density which reduces the movement of the molecules.

Optimization by bond angle

The two O-H bonds in water have an angle. Due to the higher repulsive force of the electron pairs on the far oxygen side, the angle between these bonds is lower than found in similar tetrahedral bonds: around 105° instead of around 109.5° . A commonly observed bond angle for the H-O-H bonds is 104.52° , and is an often used bond angle in MD simulations (e.g. in the TIP3P model).

Increasing the bond angle lowers the liquid density as shown in Figure 5.9. This could be caused by the increasing repulsion from the two more separated hydrogen atoms towards other hydrogen atoms. However, the influence is con-

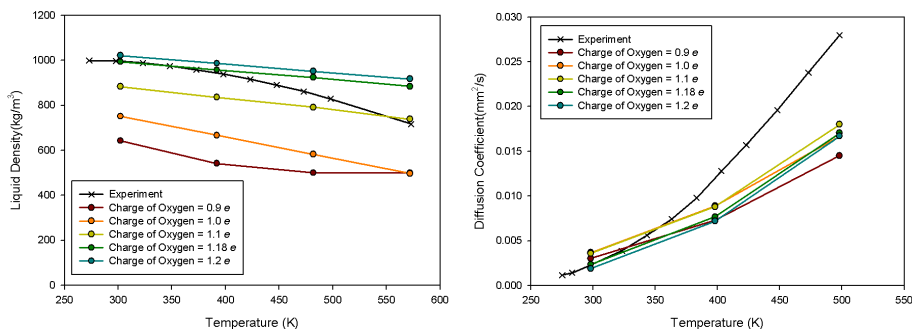


Figure 5.10: Liquid densities (left) and self-diffusion coefficients (right) of water models by varying the water atom charges. Experimental values for liquid density are from ref. [169]. Self-diffusion coefficients are from ref. [95].

siderably smaller than the change in bond length.

Changing the bond angle does not seem to have any effect on the diffusion coefficient, except for an extremely acute bond angle of 80 degrees. This could be caused by the increased local density preventing the movements, similar to the results seen from the increase in bond length

Optimization by charge

In water, the different charges of hydrogen and oxygen will result in an attraction between the two. Likewise, the Coulombic H-H and O-O interactions are repulsive.

The electric forces acting on a point charge, when in the presence of another point charge, is given by Coulomb's law:

$$F = k \frac{q_1 q_2}{r^2} \quad (5.4)$$

where k is the Coulombic constant, q_n is the individual point charge and r is the distance between two charges. From this formula it can be seen that charges with the same sign will result in a positive, repulsive force. Similarly, charges with different signs will result in a negative, attractive force.

In water, the Coulombic force is a dominant force and responsible for nearly all attractive forces. The Van der Waals and Hydrogen bonding contribute only a small part of the attraction as compared to the Coulombic force. Only at very close range, the Van der Waals force prevents atoms from colliding.

The Coulombic charges are scaled to a range of values (within 25% of literature values) from the standard model. The range of values for Coulombic charge is shown in Figure 5.10. Only the Coulombic charges have been altered, the Van der Waals potentials remain the same.

In Figure 5.10, it is shown that increasing the charges results in higher densities. As the Coulombic charges are the main source of intermolecular attrac-

Table 5.5: Parameters for the tabulated water model optimized for $T = 300K$.

Bond length l_{OH} (nm)	0.09572
Bond Spring Constant K_l ($kcal\ mol^{-1}\ \text{\AA}^{-2}$)	450
HOH angle θ_{HOH} (degree)	104.52
Angle constant K_θ ($kcal\ mol^{-1}\ rad^{-2}$)	55
Charge q_O (e)	1.18
Charge q_H (e)	-0.59

Table 5.6: Diffusion coefficient and liquid density for different water models and an experimental study at 300K.

	Our model	TIP3P ^[108]	Experiment ^[126]
Liquid density	991 kg/m^3 (302K)	1001 kg/m^3 (301K)	996 kg/m^3 (300K)
Diffusion coefficient	0.023 mm^2/s	0.057 mm^2/s	0.025 mm^2/s

tions, increasing these charges results in a net increase in attractive forces. The reverse is also valid: non-truncated, lower Coulombic charges significantly lower the density. The slope of the liquid density versus the temperature increases with lower charges. It appears that lower charges increase the temperature sensitivity of the density.

Changes in the Coulombic charges do not seem to influence diffusion coefficient at higher temperatures as much as they influence the liquid densities. Changes in the Coulombic charges have little effect on the high-temperature diffusion coefficient. Compared to the effects of changing the bond length, the diffusion coefficient is barely affected.

Discussions on tabulated potential water model

From our simulation sets it can be concluded that the density and diffusion coefficient are differently affected by the parameter setting for the water molecule. However it is not possible to find parameters that works for the whole range of temperatures. But we still could develop a tabulated water model that is optimized with respect to the diffusion coefficient and liquid density at one specific temperature. In order to develop a silicon/silica-water interaction wall in the next chapter, we choose to optimize for $T = 300K$.

Detailed parameters of the tabulated water model are shown in Table 5.5 and Figure 5.11.

The numerical results are compared to experimental data^[126] at 300K and with results of the TIP3P model^[108], and are shown in Table 5.6. Our water model predicts the self-diffusion coefficient at 300K better than TIP3P water model^[108]. At the same time it provides a comparable result with respect to the liquid density.

In addition to liquid density and self-diffusion coefficient, radial distribution function are determined for the final model. The radial distribution functions,

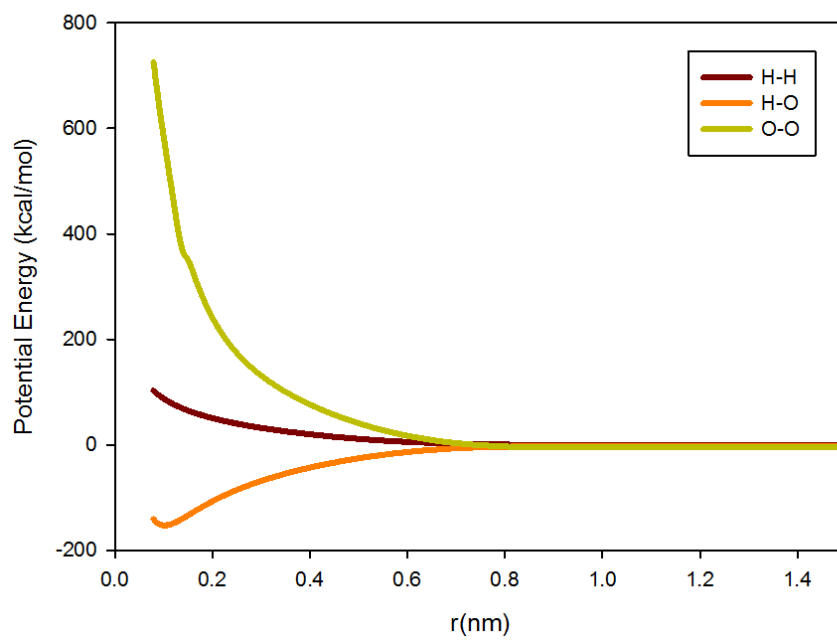


Figure 5.11: Potential functions for the tabulated water model optimized for $T = 300K$.

Table 5.7: Computation time for a 10 ps self-diffusion coefficient simulation at 300K on 1 CPU.

Model Type	van der Waal's cutoff	Coulombic cutoff	CPU time
Mod. TIP3P Neria	Non-truncated LJ	2.0nm	148053.09 s
Mod. TIP3P Kim	Non-truncated LJ	2.0nm	147244.89 s
Tabulated Water Model	2.5nm	2.5nm	62224.38 s

g_{OO} , g_{OH} , and g_{HH} are commonly used when the structure of the liquid water is studied. These intermolecular partial pair correlation functions for liquid water at 298K were also experimentally studied by Soper et al.^[146].

Radial distribution functions of the modified tabulated water model, g_{OO} , g_{OH} , and g_{HH} are compared with experimental data in Figure 5.12. Our tabulated water model has a reasonable first peak and third peak position for g_{OO} , but the second peak position occurs at a shorter distance when compared with experiment. The amplitude of the first peak is too low while it is too high at the second peak. The oxygen-hydrogen pair correlation functions are very similar to the experimental data. The main difference is the height of the first peak. The height of the first peak is much higher compared to the experimental data. In case of g_{HH} , it has a good agreement in overall structure with the experimental data, but the first and second peak position occur slightly at further distance.

Computational times of our self-diffusion coefficient simulations with modified TIP3P models and tabulated water model are shown in Table 5.7. The tabulated model for 300K shows that it is more than 2 times ($\simeq 2.4$) faster than modified TIP3P models with 2.0nm Coulombic cutoff radius.

5.3.3 Comparison with other models

Here, we compare our result to literature^[24,84,97,100,178]. Liquid densities and diffusion coefficients simulated with rigid three site models^[24,84,97,178] and the flexible F3C model^[100] are compared with the results of our tabulated water model and modified TIP3P models. All of these models (Table 5.8) are similar in nature but the Lennard-Jones, Coulombic terms, bond length and bond angle differ and give significant differences in calculated properties for water.

Flexible TIP3P modified models offer better prediction than literature values of rigid models in liquid density (Figure 5.13). An exception case is SPC/E model. Although it slightly underestimates liquid density, it overall performs much better than other rigid models. This can be mainly attributed to a self-polarization energy correction that is achieved via slightly increased atomic partial charges on the hydrogen and oxygen sites. However, because polarization effects are highly environment dependent, this simple treatment makes the model questionable for use in heterogenous systems where bulk water is interfaced with another dielectric medium (e.g. a membrane, oil, a protein, or an ion channel)^[175]. Since we are interested in the system with a dielectric surface wall

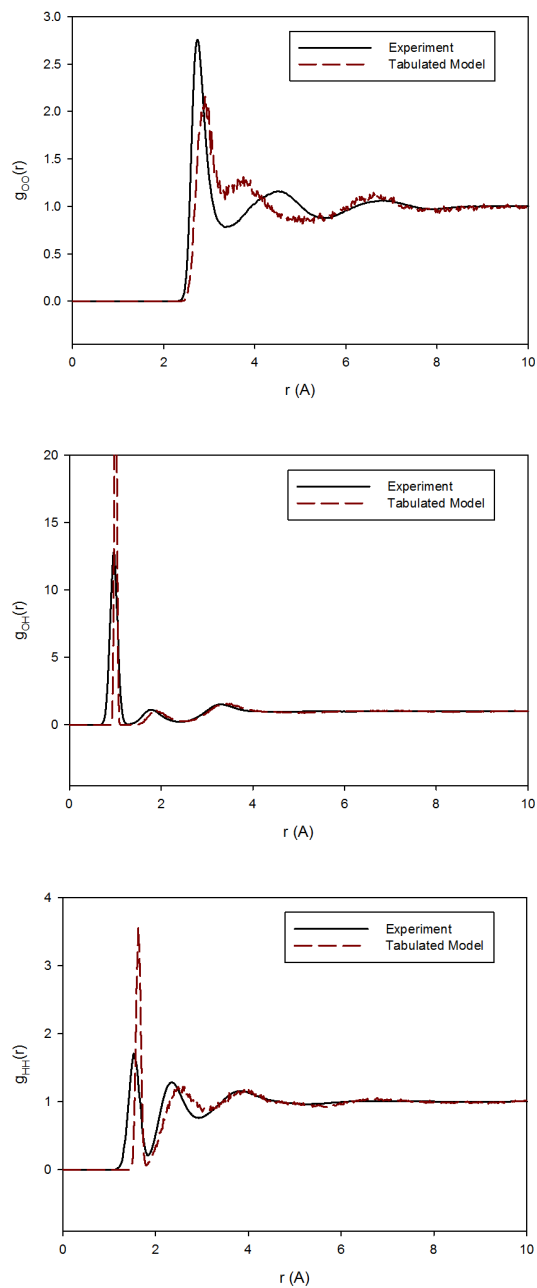


Figure 5.12: Radial distribution function of tabulated water model at $T = 298$ K (Liquid density = 998 kg/m^3). Experimental values are from ref. ^[146]

Table 5.8: Nonbonded parameters, geometry and electrostatic properties of other three-point water models.

Parameter and unit	TIP3P	SPC	SPC/E	F3C
r_0^{OO} (nm)	0.31506	0.315533	0.315533	0.3165541
ϵ^{OO} (kcal mol ⁻¹)	0.1521	0.1553	0.15533	0.1848
r_0^{HH} (nm)	0	0	0	0.0801809
ϵ^{HH} (kcal mol ⁻¹)	0	0	0	0.01
r_0^{OH} (nm)	0	0	0	0.1593161
ϵ^{OH} (kcal mol ⁻¹)	0	0	0	0.0429884
q^O (e units)	-0.834	-0.82	-0.8476	-0.82
q^H (e units)	-0.417	-0.41	-0.4238	0.41
l_0^{OH} (nm)	0.09572	0.1	0.1	0.1
θ_0^{HOH} (deg)	104.52	109.47	109.47	109.47
K_l (kcal mol ⁻¹ Å ⁻²)	-	-	-	250
K_θ (kcal mol ⁻¹ rad ⁻²)	-	-	-	60

(silica), SPC/E is not suitable even with its good liquid density and self-diffusion coefficient. The introduction of bond flexibility is increasingly discussed as an indirect and computationally less expensive way of introducing polarizability effects, resulting in better agreement with experiment for some properties of water^[129].

Most rigid models (TIP3P, SPC, etc.) tend to over predict the diffusion coefficient^[129], while SPC/E model yields good results for the diffusion coefficient at ambient condition. Flexible F3C model and our tabulated water model also give comparable diffusion coefficient as the SPC/E model. However, our simulations of flexible modified TIP3P models underestimate the diffusion coefficient in all temperature range. This might be due to the absence of Ewald Summation^[51] in the PumMa MD package^[2]. All literature values above used Ewald summation for the simulation of diffusion coefficient (Figure 5.13). It is a method for computing the interaction energies of periodic systems, particularly electrostatic energies. Recently Takahashi^[155] compared the self-diffusion coefficient calculated by using different shift-function methods and the Ewald summation. Takahashi's study showed that the improvement of the cutoff boundary conditions or long-range interaction treatment strongly affect the accuracy of the self-diffusion coefficient.

5.4 Conclusion

In this chapter, we have studied structural and dynamic properties of flexible three site water models that are optimized for PumMa Molecular Dynamics simulation package: a modified version of TIP3P and a tabulated water model.

We showed the effect of two different cutoff radii: the van der Waal's cutoff radius and the Coulombic cutoff radius for modified TIP3P model. They both

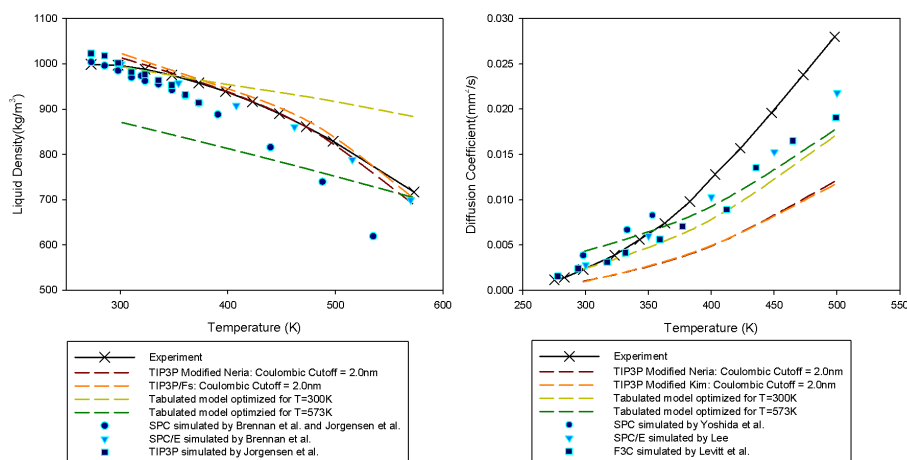


Figure 5.13: Comparison with other 3 site models^[24,84,85,97,100,178]. Experimental values for liquid density are from ref.^[169]. Self-diffusion coefficients are from ref.^[95].

have a substantial effect on liquid density while only the Coulombic cutoff radius has an influence on the self-diffusion coefficient.

The tabulated model is optimized by parameterizing O-H bond length, HOH bond angle, and the charge of each site. In this study we have shown that the charge is the most dominant parameter which determines the liquid density of the water model. Increasing the bond length also reduces the dependency of the density. The slope of the liquid density versus the temperature is significantly lower for the higher bond lengths. The bond angle has the least influence on the liquid density.

The Radial Distribution Function is studied in addition to the liquid density and the self-diffusion coefficient. Our results for the liquid density for modified TIP3P models are in good agreement with recent studies, while the self-diffusion coefficient is underestimated due to the absence of the Ewald summation method. Our optimized tabulated model is good for isothermal systems and showed a more than 2 times faster computation compared to conventional models.

6

Development of EEM based silicon-water and silica-water wall potentials for non-reactive Molecular Dynamics simulations

Molecular dynamics simulations of heat transfer in gases are computationally expensive when the wall molecules are explicitly modeled. To save computational time, an implicit boundary function is often used. Steele's potential has been used in studies of fluid-solid interface for a long time. In this work, the conceptual idea of Steele's potential has been extended in order to simulate water-silicon and water-silica interfaces. A new wall potential model is developed by using the electronegativity-equalization method (EEM), a ReaxFF empirical force field and the non-reactive molecular dynamics package PumMa. Contact angle simulations are performed in order to validate the wall potential model. Contact angle simulations with the resulting tabulated wall potentials gave a silicon-water contact angle of 129° , a quartz-water contact angle of 0° , and a cristobalite-water contact angle of 40° , which are in reasonable agreement with experimental values.

6.1 Introduction

As mentioned earlier, MD can be used to investigate the influence of the gas-surface interaction in more detail, because this technique allows the walls to be modeled explicitly with an interaction potential. Explicit walls are expected to give the best results, but at the price of high computational costs. Since several layers in the wall need to be simulated, the number of particles in the wall may be larger than the number of particles in the fluid. Therefore, the majority of the computation effort is expended for the simulation of the wall particles.

Parts of this chapter are described in:

Kim, J., Iype, E., Frijns, A. J. H., Nedeá, S. V., and van Steenhoven, A. A. Development of EEM based silicon-water and silica-water wall potentials for non-reactive molecular dynamics simulations. *Journal of Computational Physics*, 268: 51-62, 2014.

Because of this, the solid wall is sometimes replaced by an implicit boundary condition. Different types of boundary conditions have been suggested over the years; examples include the reflective and thermal walls^[58]. The reflective wall reverts the particle when it hits the wall, whereas the thermal wall introduces a stochastic force on a particle when it strikes the wall, giving the particle a new velocity sampled from a Maxwellian distribution. A more complex gas-surface interaction model, based on Cercignani-Lampis model^[33], is also available.

A major drawback of these models is that they do not supply any information about the underlying configuration of the solid wall. They also neglect the gas-surface force interaction effects which can be significant in nano-channel flows. To be able to include such information, the boundary condition has to be derived from the solid's point of view. In their pioneering work, Lennard-Jones and Devonshire derived such relations for several types of crystals^[98]. Subsequently, Hove and Krumhansl^[74], and Steele^[151] used these relations to derive potentials which describe the interaction between a gas molecule and a solid wall. Crucial in these derivations are the lattice sums using Fourier series to arrive at the proposed potential. Based on this work, Abraham^[6] proposed four types of wall potentials: the Lennard-Jones wall as given by Steele, the Lennard-Jones (10-4) wall, a Boltzmann weighted wall and a reflective wall. Both Steele and 10-4 wall potentials have been used extensively over the years. For instance, Steele's potential has been used in studies on the solvent forces of dense fluids or on the dynamics of liquid filled pores and the 10-4 potential has been used in work on the solid-fluid interface, the flow in micropores, and in work on the velocity auto-correlation function of confined fluids^[22,94,158].

Recently, further progresses have been reported in this field of wall potentials^[143,148]. Spijker et al.^[148] suggested a wall potential model which can be used for SC, FCC, and BCC type of solid wall crystal structure. Siderius et al.^[143] suggested a model that can describe cylindrical, spherical, and other pore geometries. Unfortunately all Steele, Spijker and Siderius' studies are limited to van der Waals force interaction between an electrically neutral surface and argon molecules (Lennard-Jones potential). In semiconductor industry, one of the most common gas-surface interactions is the water-silicon interaction. And in many cases a silicon surface is filmed with silica: a thin layer of silicon dioxide forms naturally on the surface when silicon is exposed to the ambient air. To describe the water-silicon and water-silica interactions, it is necessary to develop a new wall model, which includes charge interaction, sophisticated crystal structure, and a more sophisticated potential than the Lennard-Jones potential.

The objective of this chapter is to present a new method to develop a tabulated potential model^[174] that can describe the interaction between water (a multi-atomic molecule) and silicon/silica(a multi-atomic solid wall) for non-reactive MD. By using the electronegativity-equalization method (EEM)^[130] and the reactive empirical force field (ReaxFF)^[56,165,166], we are able to develop a pairwise interaction potential between a water atom(oxygen, hydrogen) and a solid wall including charge interactions.

6.2 Tabulation process

Our study starts from the concept of Steele’s potential. Steele showed that the total energy of an isolated gas atom interacting with the atoms in a crystalline solid of a given lattice symmetry can be decomposed as a Fourier series in the position variables in the plane parallel to the surface under the assumption of pairwise additivity and inverse power-law interaction^[151].

In a similar concept, under the assumption of pairwise additivity, we numerically integrate the forces acting between an isolated gas atom and the atoms in a crystalline solid. We include a charge interaction in our model, which is omitted in most other conventional wall potential models.

It is important to have the right atomic charges to enhance physical realism of MD because atomic charges in molecules contribute most of the characteristic chemical properties^[123]. In our model, the electronegativity-equalization method (EEM) is used to calculate the charge distribution of water atoms and silicon or silica atoms for different configurations. EEM will be used to derive a tabulated wall potential. Figure 6.1 shows an overview of the tabulation process. A more detailed description for each process is shown in the next sections.

6.2.1 Crystal structure

In order to develop the wall potential for silicon and silica (silicon dioxide), we first need to find the crystal structure of each wall. Many solids have a specific crystal structure, for example a simple cubic (SC), face centered cubic (FCC) or body centered cubic (BCC). Silicon crystallizes in the same pattern as diamond, in a structure Ashcroft and Mermin called “two interpenetrating face-centered cubic” structure^[12] (Figure 6.2, left) . The cube side for silicon unit cell is $0.543nm$. The angle between a and b is 90° and c is perpendicular to the other two.

Unlike silicon, silica does not have a specific crystal structure. We have chosen the most basic silica crystal structures for this study, which are the α -quartz model and the α -cristobalite model. The α -quartz wall is modeled using a silica slab that consists of $5 \times 5 \times 2$ unit cells of α -quartz. The lattice constant of one unit cell of α -quartz are chosen from the study of Will et al.^[171] (Figure 6.2, center), in which a and b are $0.491239 nm$ and c is $0.540385 nm$. The angle between a and b is 120° and c is perpendicular to the other two.

The α -cristobalite is studied in order to investigate fused silica and the function of siloxane group. The α -cristobalite plate is modeled based on the work of Downs et al.^[48] (Figure 6.2, right). The a and b values are $0.49717 nm$ and c value is $0.69223 nm$. The angle between a and b is 90° and c is perpendicular to the other two.

With these crystal structures, a wall is formed of several layers with the (1,0,0)-plane facing the fluid. The molecular structure of a silicon wall consists of 400 atoms as shown in Figure 6.2. The molecular structure for α -quartz consists of 432 wall atoms and α -cristobalite consists of 600 wall atoms. The sizes of the walls are chosen such that they are bigger than the cut-off radius

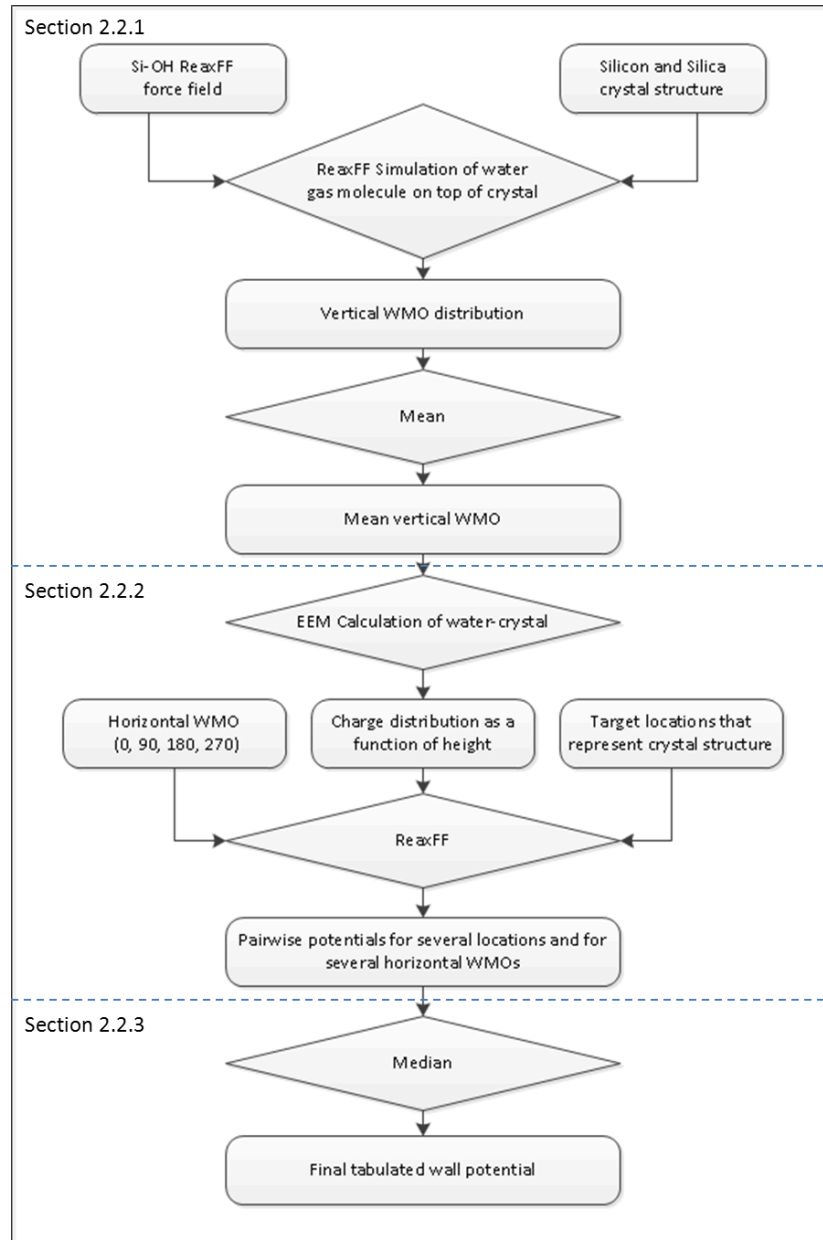


Figure 6.1: Overview of the tabulation process.

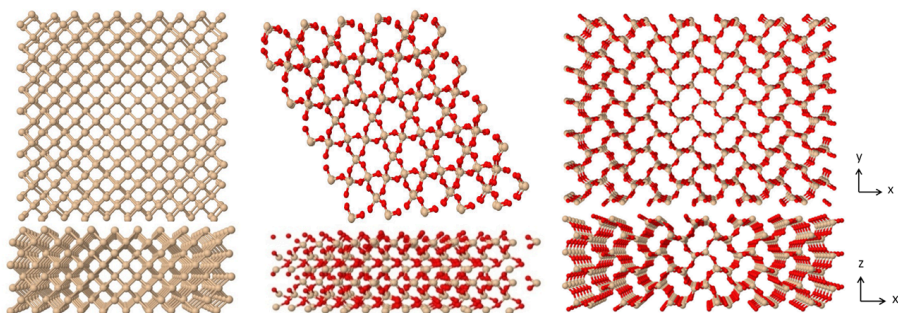


Figure 6.2: Crystalline structure of silicon (left), α -quartz (center), and α -cristobalite (right). (Brown: silicon atom, red: oxygen atom).

of water molecules in all directions from the target locations. The interaction forces between these crystal structures and a single water atom approaching this structure is evaluated at various target locations.

6.2.2 Si-OH ReaxFF force field

The interactions between oxygen and silicon and between hydrogen and silicon atoms are modeled by a ReaxFF force field. ReaxFF is an empirical force field package^[56,165,166], which is described in Chapter 2. There are several optimized ReaxFF force fields for various molecular systems. Among these optimized force fields, Fogarty et al.^[56] developed a SiO ReaxFF force field that provides a description that is appropriate for both silicon and silica, and is capable of describing the interaction with water molecules. Our work is done based on the work of Fogarty’s SiO ReaxFF force field.

ReaxFF involves an electronegativity-equalization method (EEM) charge derivation method^[130], allowing calculation of geometry dependent charge distributions. EEM is a semi-empirical density-functional theory based method, where atomic electronegativity and hardness are parameterized for the calculation of charge distribution in molecules^[116]. EEM has been successfully used for the calculation of bond charges in determining the electrostatic energies including hydrogen bonding^[123].

In ReaxFF, the energy of a system, E_{system} is calculated as:

$$E_{system} = E_{bond} + E_{lp} + E_{over} + E_{under} + E_{val} + E_{pen} + E_{3conj} + E_{tors} + E_{4conj} + E_{H-bond} + E_{vdWaals} + E_{Coulomb} \quad (6.1)$$

where E_{bond} represents the bond energy, E_{lp} is the energy due to the presence of lone pair, and E_{over} and E_{under} are the energies arising from over and under-coordination, respectively, of atoms with respect to their valency. The valence angle (three-body) energies are accounted for in the terms E_{val} and E_{tors} ,

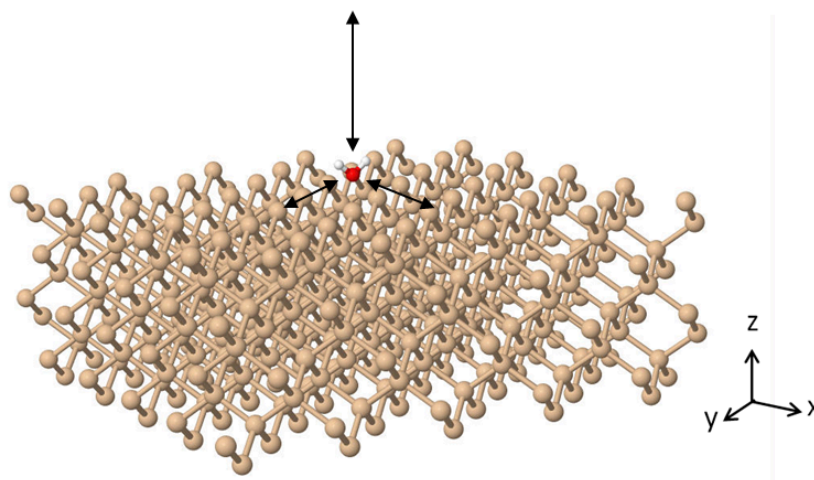


Figure 6.3: Water molecule is placed on the top of the solid wall and moved in order to capture the charge distribution of each location.

respectively. E_{pen} is a penalty energy function to stabilize a three body system with the center atom having two double bonds connected to it. Conjugated chemical bonds are stabilized by adding corrections for three bodies, E_{3conj} , and four bodies, E_{4conj} , conjugation terms to the respective systems. E_{H-bond} represents the hydrogen bond interactions. The long-range interactions such as van der Waals interactions, $E_{vdWaals}$, and Coulombic interactions, $E_{Coulomb}$, are accounted for between every pair of atoms irrespective of the presence of chemical bonds^[80].

The bond energy (E_{bond}) will not be included in the derivation of our wall potential, since we do not want to model chemical reactions, i.e. creating or breaking bonds, between wall and water atoms, during the tabulation of the pairwise interaction potential.

E_{system} will be determined at a fixed target location (x, y) on the surface, while the height z between the wall and the single molecule changes from 0 to the cutoff radius (Figure 6.3).

The charge distributions that are calculated by EEM can vary in magnitude and distribution according to (i) the water molecule orientation (WMO), (ii) the normal distance between the water molecule and silicon/silica wall, and (iii) the position of water molecule along the surface.

Water molecule orientations

It is important to take water molecule orientations (WMO) into account when tabulating the potential since the charge distribution is sensitive to water molecule orientations (WMO). WMO_{vert} and WMO_{hor} are defined by two

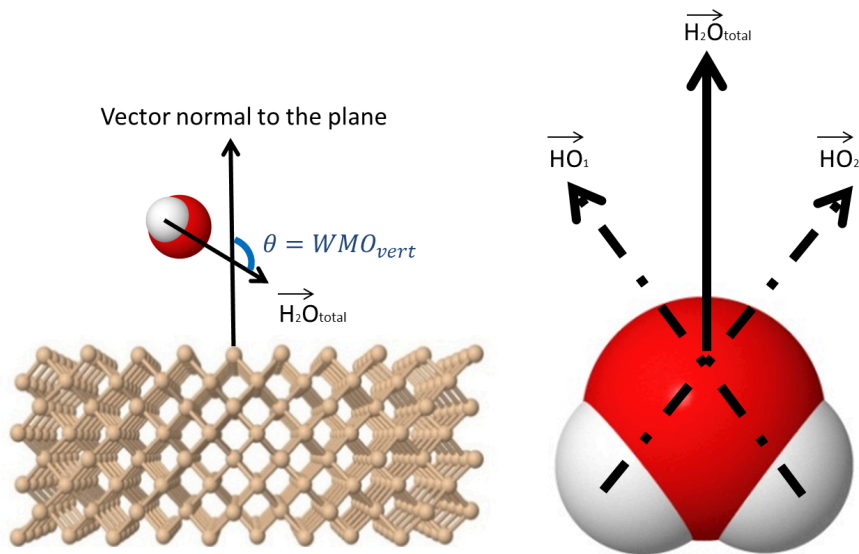


Figure 6.4: Definition of the vertical water molecule orientation, WMO_{vert} .

\vec{HO} vectors as shown in Figure 6.4. \vec{HO}_1 and \vec{HO}_2 are normalized as unit vectors and added to a single vector. WMO_{vert} is obtained by computing the orientation of the resulting vector with respect to the direction normal to the wall surface, while WMO_{hor} is obtained with respect to the direction parallel to the wall surface (Figure 6.4).

Figure 6.5 shows that the molecular orientation WMO_{vert} can have a large influence on the interaction between a molecule and the wall, especially when hydrogen bonding exists. In order to find a reasonable WMO_{vert} for building the tabulated wall potential process, we have calculated a distribution of WMO_{vert} through ReaxFF simulations. 500 water molecules and 300,000 iteration steps (1 step = 0.25 fs) are used for each material. Water molecules are freely placed above the silicon/silica wall surface and sampled when they landed on the top of the wall surface.

The mean WMO_{verts} are taken for building the final wall potential. During the 300,000 iteration steps, configurations are taken at every 200 iterations. As a result, 5916, 4859, and 14458 WMO_{vert} samples are collected for silicon, α -quartz, and α -cristobalite respectively. Only the water molecules in the first layer are collected for the distribution. The distributions are shown in Figure 6.6. The calculated mean WMO_{vert} are 92° , 22° and 32° for silicon, α -quartz, and α -cristobalite respectively.

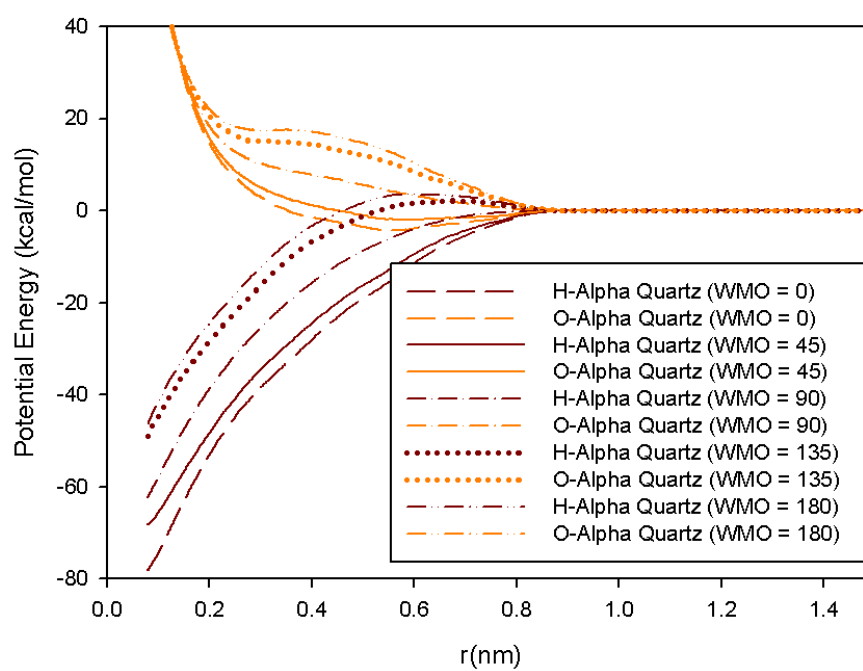


Figure 6.5: Potential functions for different WMO_{vert} for α -quartz. Orientations of 0°, 45°, 90°, 135°, and 180° result in different potential shapes.

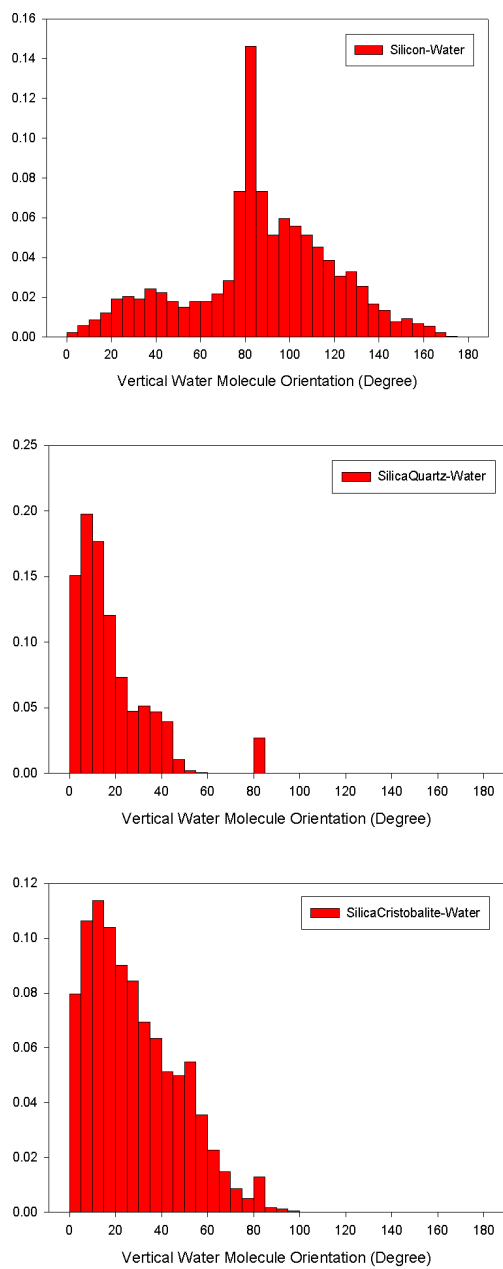


Figure 6.6: Distribution of WMO_{vert} for silicon, α -quartz, and α -cristobalite sampled through ReaxFF simulations.

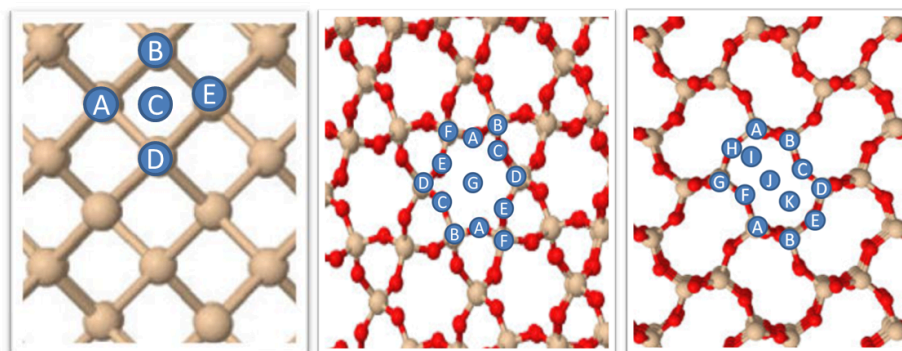


Figure 6.7: Top view of silicon(left), α -quartz(center), and α -cristobalite(right). Sampling locations of the potentials are indicated by the blue circles. Potentials are sampled at 5 target locations for silicon, while they are sampled at 7 target locations for α -quartz and 11 for α -cristobalite. (Brown: silicon atom, Red: oxygen atom)

Tabulation of pairwise potential: height

With given WMO_{vert} , the tabulation process is done as follows. The water molecule is placed at a distance z from the multi-layered solid wall, where the distance z is measured between the center of the water molecule and the first layer of the solid wall. This distance z is varied from 0 to the cutoff radius and the charge distribution at 1281 different z points is computed by the EEM method.

Then a hydrogen atom is fixed to the target location (x, y) while the distance z between the atom and the wall is varied from 0 to the cutoff radius. During this calculation, the pre-calculated charge distribution is used. The same procedure is then repeated for an oxygen atom. At these positions, the energies for hydrogen-wall and oxygen-wall interactions are determined by ReaxFF.

Finally, the tabulated E_{system} is shifted up or down to match the energy level to have a final form of our wall potential. To include the interaction potentials for all horizontal water molecule orientations WMO_{hor} , the wall potentials for the four horizontal orientation angles, WMO_{hor} , of 0° , 90° , 180° , and 270° are tabulated and averaged as a single wall potential at wall location (x, y) .

Tabulation of pairwise potential: position along the surface

The same process is repeated for different target locations by varying the values of x and y (Figure 6.7). Wall potentials at several target locations(5 for silicon, 7 for α -quartz, and 11 for α -cristobalite) are sampled and a final wall potential, which is a median wall potential of all these target locations, is produced. We pick the target locations that represent the crystal structure (locations are on top of the wall atoms and of midpoints between the atoms).

Among the potentials taken from the different locations, we take one rep-

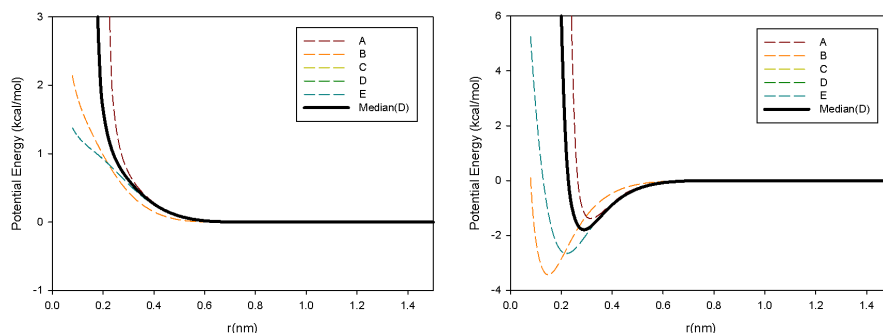


Figure 6.8: Tabulated potential of silicon wall-hydrogen(left) and silicon wall-oxygen(right) for $WMO_{vert}=32.45^\circ$ at the different locations. The sampling locations of silicon are shown in figure 6.7

representative potential which describes the average interaction as it is done in other wall potential approaches. As a representative potential, we choose the median potential function based on the well depth of the primary energy well of the potential function (Figure 6.8). The reason that we do not take a mean potential value is to preserve the shape of each potential function. By simply averaging over all target locations, some artificial peaks can be created in the tabulated potential. This will cause some nonphysical attraction and repulsion forces.

6.2.3 Final tabulated potentials

The potential functions for silicon, α -quartz and α -cristobalite that are obtained by this procedure are shown in Figure 6.9. Figures 6.6 and 6.9 show that there is a close relationship between the final potentials and the distribution functions. Silicon is known to be a hydrophobic material. The figures show that neither oxygen and hydrogen are highly attracted to silicon. However oxygen is slightly more attracted by silicon. Distribution functions in figure 6.6 show that there is a preference for the orientation wherein oxygen is heading towards the surface. In case of α -quartz and α -cristobalite, hydrogen is attracted towards the silica surfaces mainly due to H(water)-O(silica) attraction. Therefore the distributions of α -quartz and α -cristobalite are dominantly positioned in the $0 \sim 90^\circ$ area (hydrogen heading toward the surface). α -quartz showed a more hydrophilic behavior than α -cristobalite, because of the hydrogen inside silicon-cristobalite: H(water)-H(α -cristobalite) repulsion.

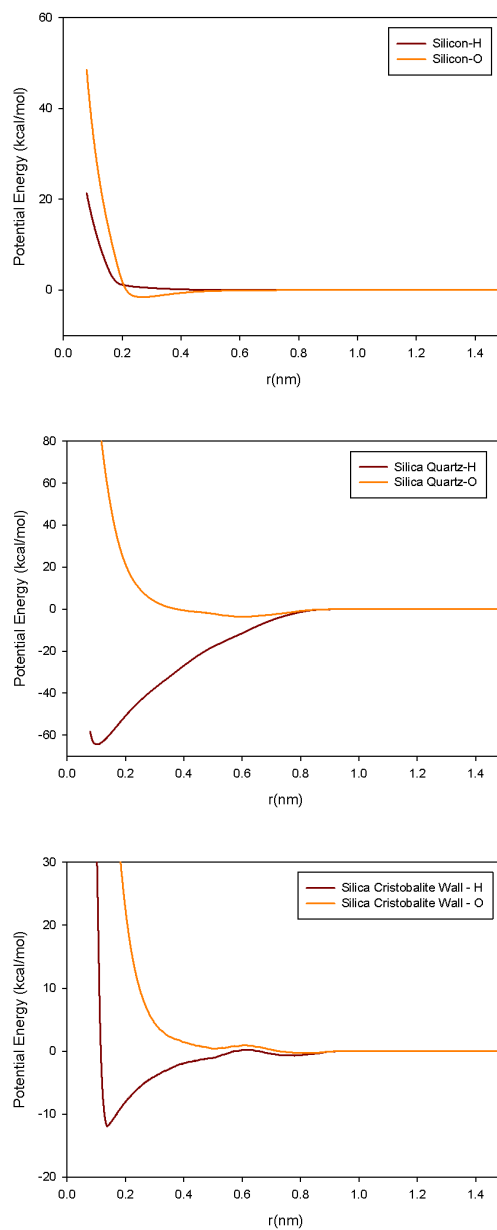


Figure 6.9: Final tabulated wall potentials for silicon-water (top), α quartz-water (middle), and α cristobalite-water (bottom). The lines are related to the interaction between the wall and a single hydrogen or oxygen atom in the water molecule.

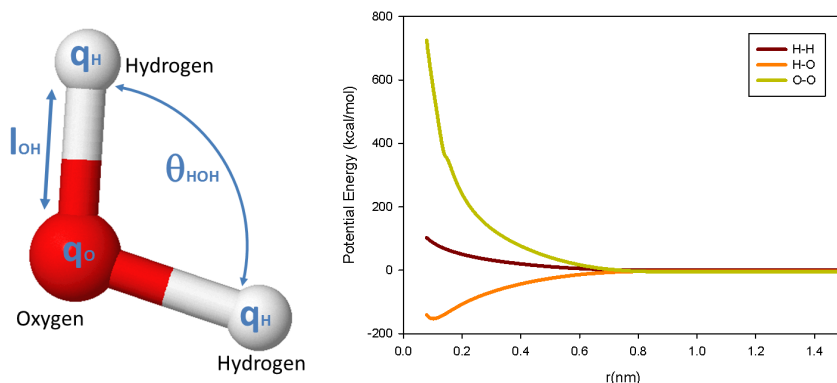


Figure 6.10: Water molecule (left) and the tabulated potential functions for the water model used for contact angle simulation (right).

6.3 Validation of wall potential

6.3.1 Validation method

The resulting potential energy function needs to be validated in the final process. Maruyama et al.^[112] performed simulations of a liquid argon droplet that is in contact with a platinum surface in order to obtain the gas-wall interaction parameter for platinum and argon. When such a liquid droplet is placed in contact with a solid surface, some degree of wetting occurs, which is determined by a force balance between adhesive and cohesive forces^[41]. The angle at which the droplet interface meets the solid surface, is called the contact angle. It is known to be a good indicator of the performance of the gas-wall interaction potential. We use the same approach.

Contact angle simulations are performed with the PumMa code^[2]. PumMa is a conventional molecular dynamics simulation software that is described in Chapter 2. In the simulations 2902 water molecules are used. They are put on the surface that is characterized by the tabulated wall potential. The reference water model in this study is a 3 point-charge tabulated water model that is described in Chapter 5. The water model is optimized with respect to the diffusion coefficient and liquid density. Detailed parameters are shown in Table 6.1 and Figure 6.10. It is refined for the PumMa MD package by our group.

The numerical results are compared to experimental data^[126] at 300K that equals the simulation temperature for the contact angle simulations, and are shown in Table 6.2. The 3 point-charge tabulated water model predicts the diffusion coefficient at 300K better than TIP3P water model^[108]. At the same time it provides a comparable result with respect to the liquid density.

The water molecules are initially placed on a regular lattice that is mod-

Table 6.1: Parameters for the water model used for contact angle simulation (See Chapter 5).

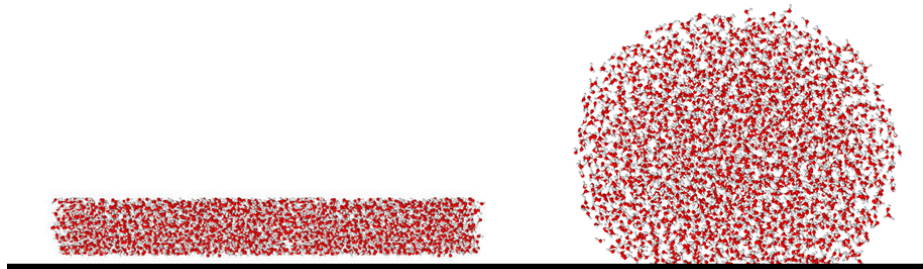
Bond length l_{OH} (nm)	0.09572
Bond Spring Constant ($kcal\ mol^{-1}\ \text{\AA}^{-2}$)	450
HOH angle θ_{HOH} (degree)	104.52
Angle constant ($kcal\ mol^{-1}\ rad^{-2}$)	55
Charge q_O (e)	1.18
Charge q_H (e)	-0.59

Table 6.2: Diffusion coefficient and liquid density for different water models and experimental studies at 300K.

	Our model	TIP3P ^[108]	Experiment ^[126]
Liquid density	991 kg/m^3 (302K)	1001 kg/m^3 (301K)	996 kg/m^3 (300K)
Diffusion coefficient	0.023 mm^2/s	0.057 mm^2/s	0.025 mm^2/s

eled by the tabulated potential functions (Figure 6.11). The MD simulation started with an equilibration period of 100ps in which the system is coupled to a Berendsen thermostat at a temperature of 300K. The Berendsen thermostat is also used for contact angle simulations by Shi et al.^[141]. A simulation time step of 0.1fs is used here.

To extract the water contact angle from the profile, a two-step procedure is adopted as is also used by several other researchers^[15,42,170]. Firstly, the location of the equimolar dividing surface is determined within every single horizontal layer of the drop. The points of the equimolar surface below a height of 0.8nm from the potential surface are not taken into account for the fit to avoid the influence from density fluctuations at the liquid-solid surface. Secondly, a circular best fit through these points is extrapolated to the surface of the wall potential where contact angle is measured(Figure 6.12).

**Figure 6.11:** Initial and an equilibrated configuration of water molecules on top of the silicon wall that is described by the tabulated potential functions.

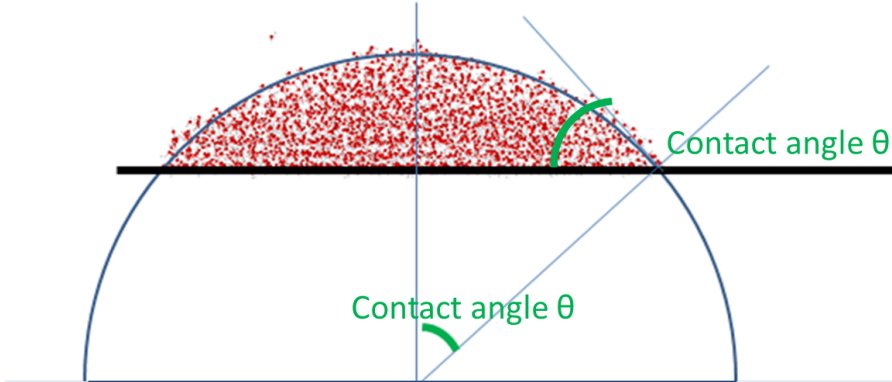


Figure 6.12: Contact angle measured by fitting a circle with center and radius to the points of equimolar dividing plane(circles).

Table 6.3: Contact angle for silicon-water ($WMO_{vert} = 92.2^\circ$), α quartz-water ($WMO_{vert} = 22.0^\circ$) and α cristobalite-water ($WMO_{vert} = 32.4^\circ$).

Interactions	Our values	Literature values	
Silicon-water	129°	86°	Experiment: Arkles ^[10]
		70.1°	Experiment: Kim et al. ^[90]
		25.6°	MD, explicit wall: Barisik et al. ^[15]
α quartz-water	0°	4°	Experiment: Li et al. ^[101]
		0°	Experiment: Pashley et al. ^[124]
α cristobalite-water	40°	40.0°	Experiment: Kanta et al. ^[88]
		39.7°	Experiment: Senn et al. ^[137]

6.3.2 Results and discussion

A contact angle simulation for silicon shows a contact angle of 129°. This is larger than reported in the experimental studies by Arkles^[10], who measured a contact angle between water and etched silicon between 86° and 88°, and Kim et al.^[90], who measured a contact angle of 70.1° for water on a bare silicon surface (Table 6.3). There can be several reasons for this deviation. Firstly, our method is based on EEM calculation which allows to calculate accurate Coulombic interactions. Therefore, our method will perform better for systems with stronger charges. Silicon can be considered to behave much more like neutral material than the other two silica materials. Backing up this reasoning, the other two silica materials gave results that are closer to the experimental values. Omission of the bonding energy will have more influence on the contact angle of silicon-water. Secondly, we are not taking into account of WMO_{hor} distribution. During the tabulating process, we are coarse graining and simplifying the

potential. The tabulating process cannot include all aspects of ReaxFF due to its limitations. However, the result is better than the simulation performed by silicon explicit wall, which was done by Barisik and Beskok. They performed a contact angle simulation with SPC/E water molecule and silicon explicit wall based on Lennard-Jones potential and Lorenth-Berthelot mixing rule^[15]. The contact angle from the simulation was 25.6° , which over estimates the attraction interaction. It shows that our EEM based method is more accurate than Lorenth-Berthelot mixing rule for silicon-water interaction.

Experimental studies of Aronov et al.^[11] and Williams et al.^[172] show that silica in general have a contact angle of $0 \sim 20^\circ$. The α -quartz simulation shows a hydrophilic behavior as well: the surface is fully wetted after the equilibrium process. For α -quartz plate, experimental studies of Li et al.^[101] and Pashley et al.^[124] showed a contact angle below 4° . Since we are using an α -quartz structure, the simulation results are reasonable. The comparison of our simulation results and experimental studies are shown in Table 6.3.

Fused silica is a silica in which a silanol group(-OH) is removed. In most forms at atmospheric temperatures, fused silica is in the form of cristobalite. Literature states that fused silica has a higher water contact angle compared to the silica with silanol groups, because siloxane group (Si-O-Si) has a weaker hydrogen bonding energy. For α -cristobalite, literature^[88,137] shows that fused silica can have a contact angle near 40° . Our simulation result shows a contact angle of 40° , which is close to the experimental results.

In order to justify the selection of median potential, an additional simulation is performed for α -cristobalite using a potential close to the median. It resulted in a contact angle of 42° . This indicates that the selection of the median potential is a suitable choice as a representative of the average potential.

As discussed earlier for silicon-water interaction, α -quartz and α -cristobalite have a relatively larger charge distribution compared to silicon and it shows a closer agreement between our model and experimental value. In the study of molecular dynamics, it is often required to have a lot of fine-tunings even for the potentials produced with reasonable physical backgrounds. The fine-tuning of a potential is frequently done by scaling the well depth of the potential^[15,112]. Our method provides a reasonable potential with a simple procedure even without any parameter optimization(fine-tuning) process.

Additionally, contact angle simulations with modified TIP3P water molecules (See Chapter 5) are performed in order to check whether our tabulated wall potential works well for other water models. Contact angle simulation results with modified TIP3P model are 125° for silicon, 0° for α -quartz, and 37° for α -cristobalite. They show slightly hydrophilic behavior compared to the simulations carried out by the 3 point-charge tabulated water model. However, the differences are all small ($3 \sim 5^\circ$). Based on this results, we can conclude that our tabulated wall potential also works well for other water models.

6.4 Conclusion

Explicit molecular dynamics simulation of gas flows are computationally demanding due to the large number of wall molecules compared to the gas molecule. This has limited the use of large scale MD simulations. In this study we improved the idea of the conventional wall potential so that it can describe the water-silicon and water-silica interactions. The new wall potential models a three-dimensional wall in the (1,0,0) plane. The wall potential is developed based on an EEM based ReaxFF force field. Through several steps, a potential energy function for the wall-water interaction is tabulated. This is then used as input for the non-reactive MD simulation code (PumMa). The contact angle is a good parameter to validate the gas-wall interaction. Our EEM based tabulated wall potential provides reasonably good contact angle results compared to experimental studies. It does not only improve the current wall potential by including a Coulombic interaction, but also shows better results than Lennard-Jones explicit wall simulations for a silicon crystal.

7

Molecular simulation of water vapor outgassing from silica nanopores

The outgassing problem, as stated in Chapter 1, is to be solved numerically by Molecular Dynamics. A slit shaped nanopore consisting of cavity and channel is built with an implicit tabulated wall potential that describes the water-silicon/silica interaction. A flexible 3-point water model is used for the simulation. The important factors of outgassing are investigated by varying the system temperature, outlet pressure, geometry, and materials of the nanopore. The results show that the temperature plays an important role in the outgassing rate, while the effect of the outlet pressure is negligible as long as it is in the high to medium vacuum range. The geometry of the channel also has an influence on the outgassing rate, but not as much as the surface material. Three different types of silica materials are tested. They represent hydrophobic material (silicon), hydrophilic material (silica-cristobalite) and super-hydrophilic material (silica-quartz). The fastest outgassing rate is found for silicon nanopore. It is also found that a thin water film is formed on the surface of the silica-quartz nanopore. This material shows hardly any outgassing of water.

7.1 Introduction

As mentioned in Chapter 1, outgassing can create problems in many applications, like wafer level packaging, contamination of the vacuum chamber, and spacecrafts. Outgassing refers to gaseous emissions from solids; these gases have been adsorbed previously^[86]. It is usually enhanced by exposure to high operating temperatures and/or low external pressures. Outgassing effects can be often found in cracks (Figure 7.1) of solid surfaces or in small cavities of MEMS/NEMS structures (Figure 7.2).

Since outgassing molecules are a source of impurities in the semiconductor industry and causes of MEMS/NEMS device failures, it is necessary to under-

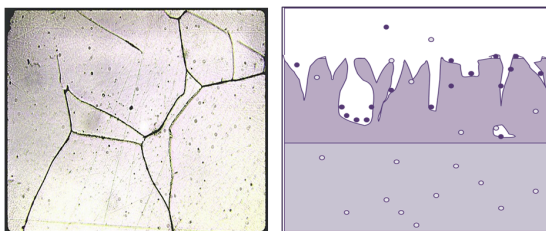


Figure 7.1: (a) A solid surface with small cracks, and (b) schematic figure of outgassing of gas molecules adsorbed on the solid surface.

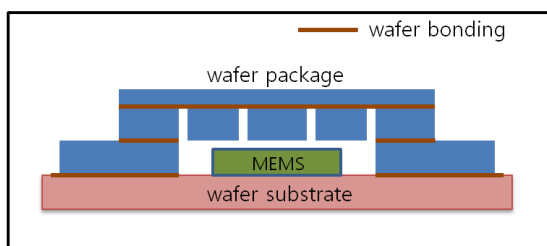


Figure 7.2: Schematic figure of MEMS device and wafer level packaging.

stand the nature of outgassing happening in micro- and nano systems in order to control it. However, considering the great complexity of micro-fabrication processes, the understanding of outgassing behavior also becomes a very complex task; it is dependent on temperature, outlet pressure, geometry, surface materials, etc. The influence of all these parameters have to be understood and controlled. In order to understand the outgassing of water molecules in cracks of the surfaces or in MEMS/NEMS devices, we simulate outgassing of water molecules from silicon/silica nanopores.

7.2 Method

7.2.1 Simulation details

The nanopore for the outgassing simulation is modelled as a slit between two walls of parallel stacked silicon/silica plates extended from a cavity (Figure 7.3). The pore width, H , is the distance between the silicon/silica walls of the nanopore. The pore width, H , is chosen such that the potential energies of interaction exerted by the two opposing surfaces are not affected by each other. In our simulation, we use a minimum pore width of $10nm$.

To simulate the outgassing of water vapor from a silicon/silica nanopore, molecular dynamics simulation methods are used for the outgassing simulations (Figure 7.4): a pressure controller described in Chapter 2, a flexible 3 point model described in chapter 5, and a water-silicon/silica tabulated wall potential

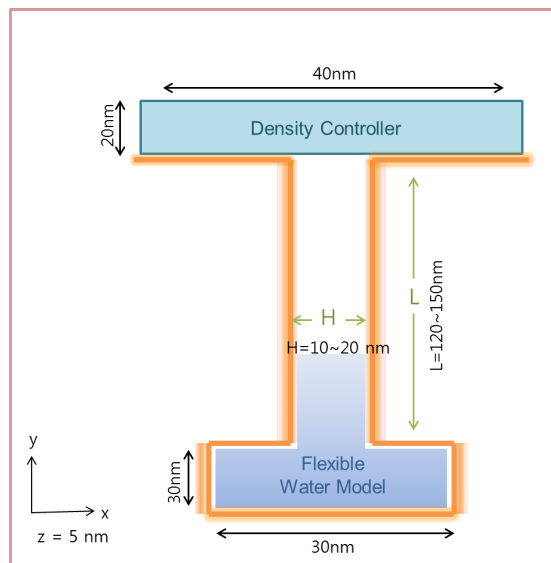


Figure 7.3: Overview of the nanopore. On top, a density/pressure controller is used. The walls are modelled by wall potentials. The simulation system is 6 nm deep in z -direction. Periodic boundary condition is applied in z -direction.

described in Chapter 6. The water molecules are modelled by the flexible TIP3P water model (flexible 3 point water model by Kim) described in Chapter 5; long range corrections (Ewald summation) are not applied.

Here, the flexible TIP3P model is used instead of the 3 point-charge tabulated water model although the 3 point-charge tabulated water model is 2.4 times faster in computation. In Chapter 5, we have found that the flexible TIP3P model provides reliable liquid density for all temperatures, while the 3 point-charge tabulated water model is only good for one optimized temperature. Since the 3 point-charge tabulated water model was not optimized for the simulating temperatures, we have chosen the flexible TIP3P model for this chapter.

The water-silicon/silica wall interactions are modelled by tabulated potentials as described in Chapter 6. Since a smooth potential is employed to represent the silicon/silica planes, the wall is frictionless. This is not true for the silicon/silica atoms in a real adsorbent. In order to add friction like behavior to the wall potential, the so-called diffuse boundary condition is employed. It is based on the diffuse boundary conditions used by Cracknell et al.^[39] and Travis et al.^[159]. However, it is modified here for the case of water molecules. Application of our molecular diffuse boundary condition proceeds as follows. After each molecular dynamics time step we check to see if the following two conditions are satisfied: (1) The center-of-mass momentum component of a given molecule in the perpendicular direction to the surface has reversed in sign compared to the previous time step. (2) The center-of-mass of that same molecule is within

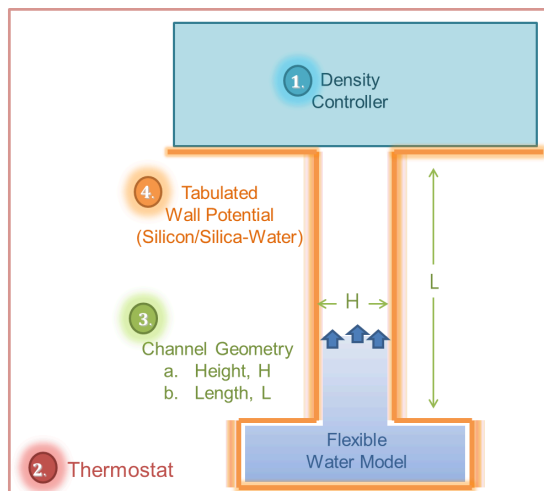


Figure 7.4: Overview of the chapter and important factors for outgassing.

the repulsive region of the water-silicon/silica wall potential. When both conditions are satisfied, we reassign a new center-of-mass velocity component of that molecule. The molecule will keep its velocity component in the perpendicular direction to the surface in order to maintain the gas-wall interaction strength, while it gets a new velocity from Maxwell-Boltzmann distribution at the appropriate temperature in the directions parallel to the surface to model a friction like behavior; since the molecules maintain the gas-wall interaction strength in the perpendicular direction, they will be attracted to the hydrophilic surface. The wall condition will not act like a thermal wall condition which has a quasi-thermostat behavior.

All three different wall materials (silicon, silica-quartz, silica-cristobalite) are used as boundary of the nanopore to investigate the effect of materials on outgassing. Silica-cristobalite is used as a reference material for the simulations of other effects. Silica-cristobalite is chosen since it has an intermediate interaction strength among three materials; the contact angle simulation result for silicon is 129° (hydrophobic), for silica-quartz it is 0° (super-hydrophilic), and for silica-cristobalite it is 40° (hydrophilic). Often the intermediate range of interaction strength is troublesome in the outgassing process^[86].

The simulations are performed for water vapor at the temperature $T = 300K$ inside the cavity. The number of molecules for the bulk water vapor in equilibrium with the fluid is taken to be 1000 water molecules for all simulations.

The simulations are carried out by varying the main factors of outgassing (Figure 7.4): the outlet pressure, the temperature, the geometry of the nanopore, and the material of the nanopore. The Berendsen thermostat^[18] is used for controlling the system temperature in the whole domain. A thermostat is applied to the whole domain, since a temperature controlled oven is often used in real outgassing treatments. The outlet pressure is controlled outside the

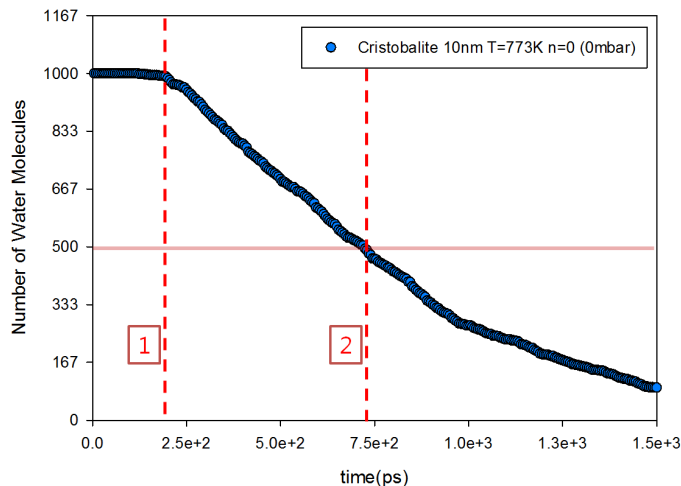


Figure 7.5: Definition of half-life (position 2). An outgassing simulation is shown for a cristobalite nanopore with channel width of 10nm , outlet pressure of 0mbar , and outgassing temperature of 773K .

nanopore (Figure 7.4) by controlling the density of that region. To calculate a reliable outgassing result, our simulations have computed 6,000,000 time steps where 1 time step represents 0.0005ps .

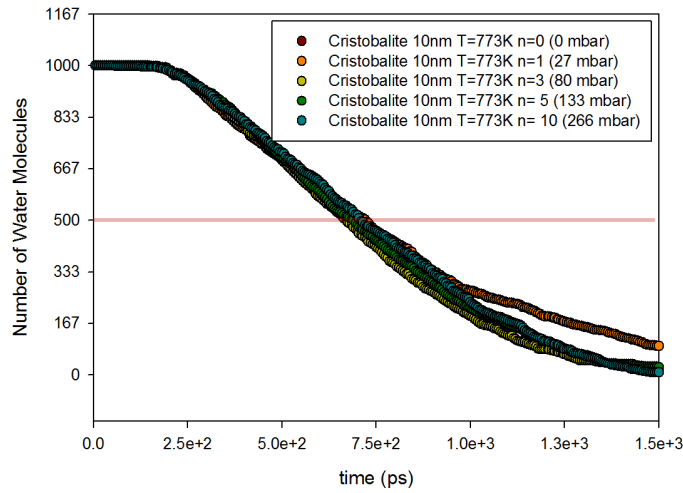
7.2.2 Half-life

In real systems, where the pumping speed is constant, the pressure in the system will follow an exponential decay with time^[86]. Half-life is therefore used throughout the chapter to represent the outgassing behavior. It is the amount of time required for a quantity to fall to half its value as measured at the beginning of the time period. It is especially a good parameter for any quantity which follows an exponential decay.

In our study half-life is defined as the time that is needed to reduce the amount of molecules to half of its initial value (Figure 7.5, position 2). The half-life includes the time for the water molecules to reach the outlet of the nanopore from their initial positions (Figure 7.5, position 1). For most of the outgassing studies, the time for the water molecules to reach the outlet of the nanopore is negligible compared to the experimental time. However, for our simulation scale, it is noticeable throughout the studies and also has an impact on the half-life: it changes by the outgassing factors. We do not divide the half-life into two different time sets as it is hard to distinguish the exact point where the outgassing phase changes.

Table 7.1: Parameter values for the study of the outlet pressure effect. Only the pressure is varied.

Set 1: Varying outlet pressure	
Outlet pressure	0mbar, 27mbar, 80mbar, 133mbar, 266mbar
Temperature	773K
Channel width, H	10nm
Channel length, L	150nm
Surface material	silica cristobalite

**Figure 7.6:** Influence of outlet pressure on outgassing.

7.3 Results and discussion

7.3.1 Effect of outlet pressure

In order to check the influence of outlet pressure on outgassing, the pressure was varied from 0mbar to 266mbar. These pressures cover perfect vacuum(0mbar), medium vacuum(27mbar, 80mbar, 133mbar) and low vacuum state(266mbar). The chosen parameter values to analyze the influence of outlet pressure on outgassing are shown in Table 7.1.

The half-lives of water molecules for different pressures are shown in Table 7.2. These values are almost the same. Figure 7.6 also shows that the decays in number of water molecules are nearly identical. This indicates that for $T = 773K$, the outgassing rate is hardly influenced by the outlet pressure. The same trend is also observed for $T = 523K$.

To explain this result, we have to look to the mechanism. The probabilities

Table 7.2: Half-lives of water molecules inside a silica-cristobalite nanopore for different outlet pressures.

Outlet pressure	0mbar	27mbar	80mbar	133mbar	266mbar
Half-life	0.71ns	0.61ns	0.67ns	0.71ns	0.79ns

Table 7.3: Parameter values for the study of the outlet temperature effect.

Set 2: Varying temperature	
Outlet pressure	0mbar
Temperature	423K, 523K, 673K, 773K
Channel width, H	10nm
Channel length, L	150nm
Surface material	silica cristobalite

that the water molecules will interact with each other for all four pressures are too small to influence the outgassing process. The smallest mean free path for our simulations (at low vacuum state) is around $0.5\mu m$ (based on an effective diameter of water vapor = $0.46nm$ ^[121]). It is more than 100 times bigger than the cut-off radius of our water-water interaction ($2.5nm$) in our MD simulations. Hence, the outlet pressure will have a negligible influence on the outgassing for all cases.

In conclusion, decreasing the outlet pressure by using a bigger pump size can be advantageous to enhance the outgassing, but not for the near vacuum state (perfect vacuum - low vacuum).

7.3.2 Effect of temperature

Early workers baked systems to about $200^\circ C$, which was effective in removing weakly bound surface water and hydrocarbon molecules^[3]. The effectiveness of high baking temperature bakes is demonstrated by Calder and Lewin^[26], who showed that outgassing could be reduced to about $10^{-16}mbar\ l/s\ cm^2$ by baking for 11 days at $300^\circ C$ or only for 1 hour at $635^\circ C$. In this section, the effect of temperature on outgassing is studied. Table 7.3 shows the parameter values for this study: $T = 423K, 523K, 673K,$ and $773K$. These test temperatures are chosen based on the study of Ishikawa et al.^[77-79]

The simulation results (Figure 7.7 (top), and Table 7.4) clearly show the benefits of high baking temperatures and the diminishing amount of water molecules inside the nanopore with increasing baking time; the half-life of the water molecules is clearly shorter for higher temperatures.

Outgassing rate is shown in Figure 7.7 (bottom). The simulation result shows that temperature increases the outgassing rate the most when temperature changes from $T = 423K$ to $T = 523K$. The influence becomes minimal for higher temperatures. This is mainly because the three higher temperatures

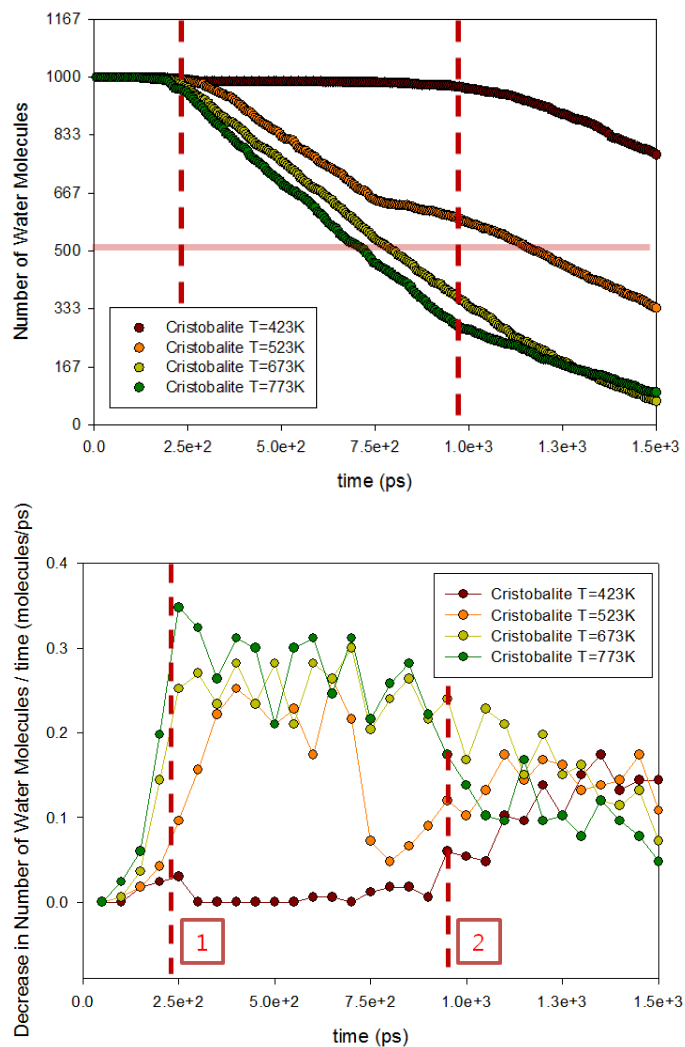


Figure 7.7: Influence of baking temperature on outgassing (top), and outgassing rate (bottom).

Table 7.4: Half-lives of water molecules inside the nanopore for different temperatures.

Temperature	423K	523K	673K	773K
Half-life	2.05ns	1.18ns	0.81ns	0.72ns

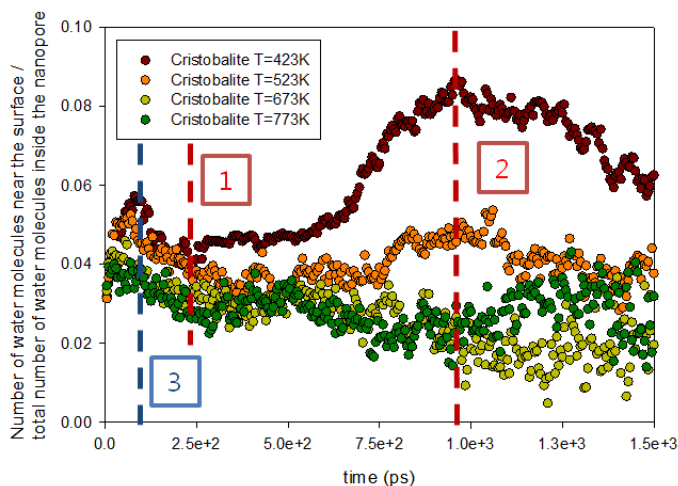


Figure 7.8: Density distribution of the water molecules in the nanopore: number of water molecules near the surface/total number of water molecules inside the nanopore. Point 1 and 2 are also shown in Figure 7.7.

($T = 523K$, $673K$, and $773K$) need similar times for water molecules to reach the outlet of the nanopore (Figure 7.7, point 1), while at $T = 423K$ it requires much longer time (Figure 7.7, point 2).

According to Hässig et al.^[68], the outgassing process can be explained with three different mechanisms: desorption, diffusion, and decomposition. By theory, desorption outnumbers the effect of diffusion greatly in the initial phase of outgassing. The rate of desorption will depend on the binding energies of the gas-wall interaction, the surface temperature, and the surface coverage^[86]. If all adsorbed molecules have been desorbed from the surface, a different mechanism of outgassing comes into action^[86]. Water molecules dissolved in the bulk should diffuse to the region where the concentration is lower. The outlet of the nanopore is such a region for our simulations. Eventually it will lead to outgassing.

In our simulations, desorption and diffusion both take place at the same time. A water molecule which is adsorbed on the surface will desorb from the surface, and will diffuse towards the outlet of the nanopore. But it will eventually re-adsorb again while it is flowing out.

In order to find out what is the dominant factor for different temperatures, we have calculated the ratio of number of water molecules that are near the wall surface and the total number of water molecules in the nanopore (Figure 7.8). A molecule which has a distance less than $2.5nm$ from the wall surface is counted as a water molecule near the surface, and the rest is considered to be in the bulk. A distance of $2.5nm$ is chosen since it is the cutoff radius for the tabulated wall potentials; there will be no direct interaction anymore when the distance

between the molecule and the wall is larger than this cut-off distance.

Based on the density ratio, desorption rate is considerably smaller for $T = 423K$ than for other temperatures inside the silica-cristobalite nanopore. It is shown that nearly two times more water molecules are near the surface for $T = 423K$ than for higher temperatures.

In Figure 7.8, there are two points where the density of the molecules near the surface increases. The first increase (from $0ps$ to point 3) can be due to a change in position of the water molecule due to the system equilibration. In the initial state, water molecules have been randomly placed inside the nanopore. However, when the simulation is started, water molecules feel the attraction from the surface and move towards the surface. The second increase (from $7500ps$ to point 2) only happens at $T = 423K$. This increase can be explained by the removal of bulk particles. If desorption rate is limiting the outgassing of water molecules, the bulk particles will be flowing out easier than the particle absorbed on the surface where friction exists. Hence, it will be the bulk particle to be the first to reach the outlet of the nanopore. Therefore the ratio increases rapidly. However, this increase does not appear for higher temperatures (point 1). It indicates that for high temperatures, desorption rates are high enough that even the water molecules near the surface are hardly influenced by the friction of the wall surface.

After point 1 (for $T = 523K, 673K, \text{ and } 773K$) and point 2 (for $T = 423K$), the number of molecules inside the cristobalite nanopore decreases, and the pressure of gas inside the nanopore decreases at constant temperature. According to the adsorption isotherm theory^[25,96] which explains the adsorption of gas molecules on a solid surface, the quantity of gas adsorbed on a given surface decreases when the pressure decreases. We observe that the ratio decreases smoothly with time, since the pressure (related to the total number of water molecules) inside the nanopore is decreasing with time as well.

7.3.3 Effect of geometry

The geometry effects on outgassing are indicated by several researchers. Ishikawa et al.^[77-79], indicated that surface treatments and raw material quality (like surface roughness) can improve the outgassing rate substantially. It was also found by Tuller et al.^[160] that water sometimes get stuck during the outgassing at some specific locations, such as a corner.

The geometry of the nanopore is studied in order to determine how the roughness, crack size on the surface, or geometry of MEMS/NEMS device can influence the outgassing. The geometry of the nanopore is described by two variables which are shown in Figure 7.4: channel width H and channel length L .

Channel width

Two channel widths ($H = 10nm$ and $20nm$) are tested at four different temperatures as described in Table 7.5.

Table 7.5: Parameter values for the study of the geometry effect (channel width).

Set 3a: Varying channel width	
Outlet pressure	0mbar
Temperature	423K, 523K, 673K, 773K
Channel width, H	10nm, 20nm
Channel length, L	150nm
Surface material	silica cristobalite

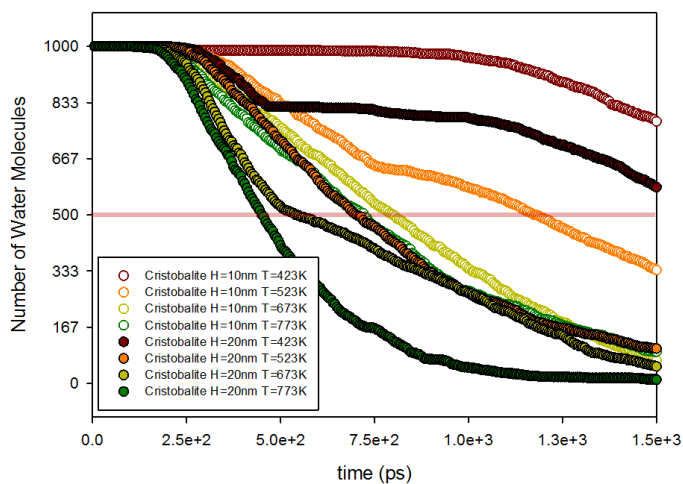

Figure 7.9: Influence of channel width on outgassing.

Table 7.6: Half-lives of water molecules inside the nanopore for different widths.

	Temperature	423K	523K	673K	773K
$H = 10nm$	Half-life	2.05ns	1.18ns	0.81ns	0.72ns
$H = 20nm$	Half-life	1.63ns	0.71ns	0.54ns	0.46ns
Factor	Half-life(20nm)/Half-life(10nm)	0.80	0.60	0.67	0.65

As shown in Figure 7.9, the channel width clearly has an influence on the outgassing of water molecules; the larger the channel width is the faster the outgassing is. By increasing the channel width from $H = 10nm$ to $H = 20nm$, half life of the water molecules is decreased by a factor of around 0.63 for temperatures above $523K$ (Table 7.6). For $423K$ the factor even increases to 0.8.

From these results, we can conclude that the effect of larger width size is more dominant for higher temperatures. A similar effect occurs for lower temperatures in the beginning of the outgassing, but eventually the outgassing rate becomes similar to the one for smaller channel width size. Increasing the channel area will increase the outgassing by diffusion. When the outgassing process is diffusion limited, it can be described by Fick's diffusion equation^[54]:

$$\text{Outgassing rate} = QA, \quad (7.1)$$

$$Q = -D \frac{dc}{dx}, \quad (7.2)$$

where Q is the diffusion flux, c is the concentration, and D is the diffusion coefficient, which depends exponentially on temperature. The diffusion coefficient can be written in equation as:

$$D = D_0 e^{\frac{-E_a}{RT}}, \quad (7.3)$$

where D_0 is temperature-independent pre-exponential, E_a is the activation energy for diffusion, R is the gas constant, and T is absolute temperature.

Therefore, the effect of larger width size will be more influential to the outgassing by diffusion than outgassing by desorption. In addition, the effect will be more dominant for higher temperature as mentioned in Section 7.3.2.

Channel length

Two channel lengths ($L = 120nm$ and $150nm$) are simulated at four different temperatures as described in Table 7.7.

As shown in Figure 7.10, the channel length also has an influence on the outgassing of water molecules; the shorter the channel length is the faster the outgassing occurs. By decreasing the channel length, the half-life of water molecules has decreased by a factor of around 0.84 for temperatures above $523K$ (Table 7.8). For $423K$ the factor is smaller and is 0.5. From these results, we can conclude that the effect of shorter channel length is more dominant for lower temperatures. This result is in line with the earlier observation that desorption has a larger influence for lower temperature. By reducing the channel length, we reduce the surface area which reduces the chance of absorption. Eventually, this will reduce the effect of desorption on the outgassing.

For a cristobalite nanopore, we can conclude that the channel length is more influential for the outgassing at lower temperature (where desorption is important), while the channel width is more influential for the outgassing at higher temperatures (where desorption is less important).

Table 7.7: Parameter values for the study of the geometry effect (channel length).

Set 3b: Varying channel length	
Outlet pressure	0mbar
Temperature	423K, 523K, 673K, 773K
Channel width, H	10nm
Channel length, L	150nm, 100nm
Surface material	silica cristobalite

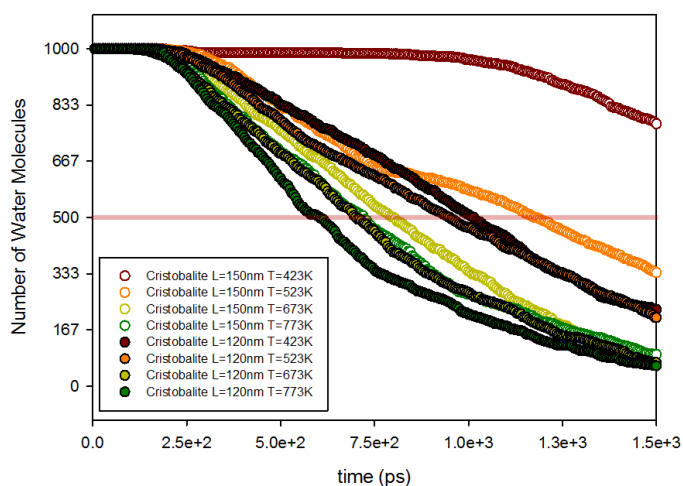


Figure 7.10: Influence of channel length on outgassing.

Table 7.8: Half-lives of water molecules inside the nanopore for different lengths.

Temperature		423K	523K	673K	773K
$L = 120nm$	Half-life	1.02ns	0.96ns	0.71ns	0.61ns
$L = 150nm$	Half-life	2.05ns	1.18ns	0.81ns	0.72ns
Factor	Half-life(120nm)/Half-life(150nm)	0.50	0.81	0.87	0.84

7.3.4 Effect of materials

All solid surfaces have attraction forces normal to the surface. So molecules landing on the surface can be adsorbed by the wall material. The adsorbed molecules can act as the main source of contaminant gas in vacuum systems.

Adsorption takes place by physical adsorption or chemical adsorption^[43]. In physical adsorption gas molecules are attracted weakly by van der Waals forces with binding energies of less than 10kcal/mol , while in chemisorption actual chemical bonding occurs between the gas molecules and the molecules and atoms on the surface of the vacuum material. Chemisorption has a binding energy more than 20kcal/mol .

Three different surface materials (silica cristobalite, silica-quartz, silicon) are simulated for four different temperatures as described in Table 7.9. Binding energy for the water-silicon tabulated wall potential is 1kcal/mol , for the water-quartz tabulated wall potential it is 60kcal/mol , and for the water-cristobalite tabulated wall potential it is 10kcal/mol (See Chapter 6). This can not be directly compared to the binding energies of physical adsorption (10kcal/mol) and chemical adsorption (20kcal/mol) values since they are the sum of multiple interactions between a gas molecule and multiple wall atoms, but they still give a clear indication on the type of water-wall interactions.

Since we did not take reactions into account for the tabulated wall potentials, all binding energies are not due to chemical adsorption. The strong binding energy might be caused due to the strong hydrogen bonding. The normal hydrogen bonds are regarded as those with strengths of about $3 \sim 5\text{kcal/mol}$ and are generally less than 12kcal/mol . However, some strong hydrogen bonds may have energies in excess of 12kcal/mol ^[36].

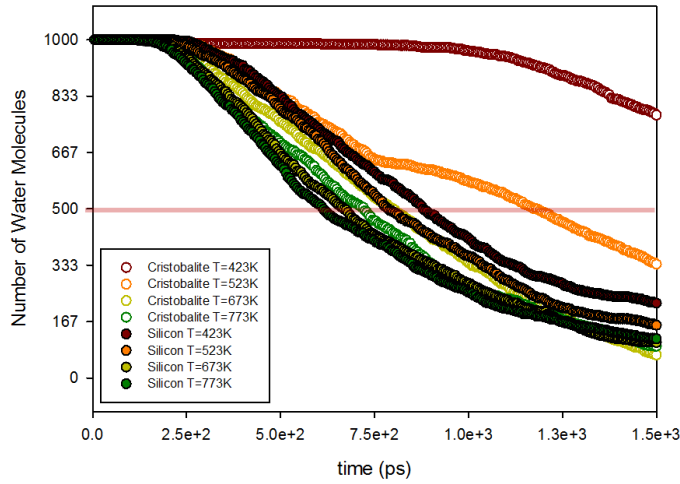
Figure 7.11 shows the outgassing of water molecules in different nanopores (silicon and silica-cristobalite), while Table 7.10 shows the half-life of the water molecules inside the nanopore for different materials. The results for silica-quartz are not shown in Figure 7.11 and Table 7.10 because it did not show any outgassing within the simulation time. Table 7.10 also shows the effect of different materials as the temperature increases: half-life of the water molecules is increasing by a factor (silicon/cristobalite) of around 0.43 for temperature $T = 423\text{K}$ to a factor of 0.86 for $T = 773\text{K}$.

Two main interpretations can be made on the basis of the results. For low binding energy, the desorption rates are so high that the corresponding molecules quickly desorb from the wall surface and cause no further problems in outgassing. For very high values of binding energy, the desorption rates are too small to see any outgassing. Silica-quartz is an example of a case of very high binding energy and it is observed that the outgassing is hardly influenced by the temperature. Once water molecules are adsorbed on the surface, they can not overcome the binding energy of the silica-quartz surface and stay there; thin water layer is formed on the surface. Hence, no outgassing happened within the simulation time.

An additional simulation has been made with $T = 1500\text{K}$, but even for this high temperature the simulation of silica-quartz shows that the tempera-

Table 7.9: Parameter values for the study of the material effect.

Set 4: Various materials	
Outlet pressure	0mbar
Temperature	423K, 523K, 673K, 773K
Channel width, H	10nm
Channel length, L	150nm,
Surface material	silica cristobalite, silica-quartz, silicon


Figure 7.11: Influence of nanopore material on outgassing.

ture has no influence on the outgassing rate. However, in industry, the baking temperature often used for silica material is around 1000°C ^[7]. This difference between experiment and simulation might be coming from neglecting the change in crystal structures at high temperatures. Silica materials are known to change its structure from silica-quartz to silica-cristobalite when the temperature increases. According to the study of Heaney^[69,70], silica-quartz transforms to silica-cristobalite at a temperature of 1050°C . As observed, silica-cristobalite allows water molecules to outgas in a reasonable time. The temperature of $T = 1000^{\circ}\text{C}$, which is used in industry, might be a temperature needed for transformation of the surface rather than a temperature needed to overcome the binding energy.

Finally, a comparison to the simpler MD model (with argon and thermal wall boundary condition) is made. Studies like in Chapter 4 have been widely used to study outgassing. However, thermal wall boundary condition cannot simulate the effect of surface material as is possible with our potential wall models, especially not the effect of hydrophilic materials. But, a simpler models

Table 7.10: Half-lives of the water molecules inside the nanopore for different materials.

	Temperature	423K	523K	673K	773K
Cristobalite	Half-life	2.05ns	1.18ns	0.81ns	0.72ns
Silicon	Half-life	0.89ns	0.79ns	0.67ns	0.62ns
Factor	Half-life(<i>silicon</i>)/Half-life(<i>cristo.</i>)	0.43	0.67	0.82	0.86

would be sufficient if the surface is hydrophobic. In the simulation using argon gas and thermal wall boundary condition, no sticking of particles on the surface was found even for low temperatures. The simulation showed that outgassing rate was directly dependent on temperature. Among the three silica materials analyzed, the result from the simpler MD model resembles the result for silicon the best.

7.4 Conclusion

In this chapter, the main factors affecting outgassing of water molecules are studied by varying the system temperature, the outlet pressure, the geometry of the nanopore and the materials of the nanopore. A negligible influence of outlet pressure on the outgassing rate is found (for pressure range up to low vacuum), while the temperature plays an important role in the outgassing process. By increasing the system temperature from 423K to 773K the half-life of the water vapor decreased with a factor of about 0.63 for the silicon channel, and a factor of 0.35 for the silica-cristobalite. Two different outgassing mechanisms (desorption and diffusion) are discussed together with the effect of temperature on outgassing rate. The geometry of the channel also has an influence on outgassing rate, but not as much as the surface material: an increase in channel height from 10nm to 20nm results in a decrease in half-life of water vapor with a factor of about 0.8 for 423K and 0.6 for 773K. For the silica-quartz nanopore, formation of a thin water film on the surface is observed due to its very high binding energy, and hardly any outgassing of water vapor is found.

8

Conclusions and Recommendations

8.1 Conclusions

An attempt to understand the nature of outgassing in micro- and nano systems is made using Molecular Dynamics (MD) simulation. Multi phase nanoflows, especially for gases and vapors, is studied throughout the thesis. Also, techniques for Molecular Dynamics (MD) that can simulate outgassing of water molecules from silicon/silica nanopore are developed. The main conclusions are listed below.

- *Geometric effect on nanoflows*

For the fully developed flow, a gravity fed flow method has been validated for the simulation of rarefied gas flow. When using the same driving force, the maximum velocity of the flow increases when the geometry changes in the order from circular to rectangular to slit geometry, where the latter becomes 2 ~ 2.5 times as large compared with either the rectangular or circular channel. For a Knudsen number (Kn) larger than 1.0, the rectangular channel shows a similar maximum and slip velocity as the circular channel while the velocity profile is qualitatively similar to the slit channel. For Kn larger than 2 ~ 3, the Knudsen number has a relatively small influence on the slip velocity for circular and rectangular channels. The effect of the accommodation coefficient on the average flow velocity for all three geometries is studied and an allometric equation model is derived.

For the developing flow, the study shows that the channel geometry has an effect on the fluid dynamics and heat transfer of choked subsonic flows in nanochannels. The low surface to volume ratio augments the nonlinearity in axial pressure distribution, and it is observed that the slip to maximum velocity ratio of three geometries is the largest for the slit, and the lowest for circular channel. For the heated wall case, it is shown that gas heating

increases the inlet and outlet effects in the channel, which is more evident for the slit geometry compared to the other geometries.

- *DSMC for nanochannel flows*

Direct Simulation Monte Carlo (DSMC) method can accurately predict both flow and heat transport phenomena in 50nm nano channels in the transition regime. However, there is some deviation between molecular dynamics (MD) and DSMC when the gradient is large. It is also found that the deviation in temperature mainly occurs at the channel walls.

- *Development of flexible three site water models*

The liquid density for the modified TIP3P model is in good agreement with recent studies while the self-diffusion coefficient is underestimated due to the absence of the Ewald summation method. Radial distribution function (RDF) of our new modified TIP3P model provides a closer agreement with experimental studies than Neria's modified TIP3P model. Our optimized tabulated model, based on ReaxFF, is good for isothermal systems and shows 2.4 times faster computation compared to conventional models while it provides a comparable liquid density and self-diffusion coefficient.

- *Development of silicon/silica tabulated wall potentials*

Tabulated wall potentials for water-silicon/silica interaction are developed to describe the silicon/silica wall surface. Our simulated contact angle is 129° for silicon-water, 0° for silica-quartz, and 40° for silica-cristobalite. Our EEM based tabulated wall potentials predicts reasonably good contact angles compared to experimental studies: experimental contact angles are 70.1° ~ 86° for silicon-water, 0° ~ 4° for silica-quartz, and 39.7° ~ 40° for silica-cristobalite. This indicates that our tabulated wall potentials are capable to capture the main aspects of the water-silica/silicon interactions.

- *Investigation of the outgassing factors*

A negligible influence of outlet pressure on outgassing rate is observed, while temperature, material and geometry of the nanopore play an important role in the outgassing process. Influences of these factors are found to be closely connected to the outgassing mechanisms (desorption and diffusion). By increasing the system temperature from 423K to 773K the half-life of the water vapor decreased with a factor of about 0.63 for the silicon channel, and with a factor of 0.35 for the silica-cristobalite. The geometry of the channel also has an influence on outgassing rate, but not as much as the surface material: an increase in channel height from 10nm to 20 nm results in a decrease in half-life of water vapor with a factor of about 0.8 for 423K and 0.6 for 773K. A formation of thin water film on the surface of the silica-quartz nanopore is

observed. Hardly any outgassing of water vapor from the silica-quartz nanopore is found.

8.2 Recommendations for further research

During this research, a number of interesting aspects are identified. Some of them are investigated in this study but some are not, due to lack of time. The study shows a way, to a limited extent, to model gaseous nano scale systems using molecular dynamics techniques. Further extensions will enable to speed up the simulations and/or to increase the accuracy. Some possible directions are given in this section.

- *Applying a hybrid MD-DSMC method for micro- and nanoflows*

The first recommendation is to increase the simulation space, by using the MD-DSMC hybrid method. In such hybrid MD-DSMC method MD is used to compute the interactions near the boundary, while DSMC is used to compute the interaction in the rest of the area to speed up the computation. Nedeia et al. ^[118,119] studied this method in non-flow situations. In Chapter 4 it is found that there is a larger deviation between MD and DSMC near the boundary, while these results are close to each other in the bulk region (see for example Figure 4.20). This indicates that the hybrid approach will probably also work in these simulations. Extending their studies and applying it to flow situations will open new possibilities for numerical studies in micro- and nanoflows at larger time and space domains.

- *DSMC parameters for nanochannel research*

In Chapter 4, it is found that the DSMC method can be applied for nanoflows to speed up the computations. However, it is observed that, for $H = 50nm$, the cell size should be chosen much smaller than the typical bin size (1/3 of molecular mean free path in areas where the gradient is large and less than 1/2 in other area for microchannels) to calculate channel flow accurately. It would be useful to investigate the recommended cell size for nano scale simulations. This study can be carried out similarly as the studies for microchannels^[87,92]. DSMC parameters (cell size, minimum number of particles in a cell) can be varied, and velocity and temperature profiles for each parameter setting can be compared to each other in order to check where the deviations occur.

- *ReaxFF based water molecule*

In Chapter 4, a 3 point water model has been developed based on ReaxFF. The tabulated model was optimized by parameterizing O-H bond length, HOH bond angle, and the charge of each site. It would be worthwhile to calculate the

distribution of O-H bond length and HOH bond angle from ReaxFF simulations and use the average as an input of the new water model. Next, instead of using the fixed charge value, EEM based method can be used to build a tabulated potential for the water-water intermolecular interactions(H-H, H-O, and O-O interactions). By doing so, improvement in the liquid density curve is expected since an EEM based method can more accurately capture the real charge interaction between two water molecules than the fixed charge method.

- *Coupling of wall potential model with the vibrating wall concept*

Another possible direction for further research in wall potentials is to look for a way to couple it with existing implicit wall models. The problem of the wall potential models is that they can not provide a thermal interaction between the wall and the fluid. In order to couple the wall potential with the thermal wall, it is necessary to modify the tangential velocity of the reflected particle with a new model which takes into account the kinetic energy gained from the wall potential. If the thermal wall is directly coupled with a wall potential, it will cool down the system to a lower value than the objected temperature. The attraction force from the wall potential will reduce the kinetic energy of the particle that escapes the wall potential. The position of the thermal wall can be positioned at the well minimum of the potential energy function in order to interact with all particles colliding the wall. The study can be further continued to the coupling of the wall potential and van den Akker's vibrating wall model^[163], which allows to exchange energy between the wall and the particle. By coupling two models together, it will be possible to simulate not only the thermal interactions of hydrophobic materials but also for hydrophilic materials. This will allow us to study phenomena such as condensation of hot gas molecules on a cold wall surface with implicit wall models.

- *Extending the outgassing research to other wall materials*

Other than silica materials, outgassing from stainless steel and aluminium nanopores can be investigated in the future. The desorption energy of water on these surfaces lies in the range of 19 to 23kcal/mol^[86]. In case of aluminium, it might be possible to build a tabulated potential based on empirical force field method as was done in Chapter 6. However, a wall potential for stainless steel will be harder to develop since it is a more complex material than silicon or silica as it is a compound of many materials. However, the wall potential for stainless steel can also be developed based on Steele's wall potential while optimizing the well depth. It will provide a much more simpler gas-wall interaction compared to the real water-stainless steel interaction. But, such modified Steele's potential will not be able to predict the water orientations near the surface, nor capture the charge interactions between water molecule and stainless surface. This might be improved by optimizing the potential well depth through contact angle simulations and compare those with experimental contact angle data.

- *Extending the outgassing research to circular and rectangular nanopores*

During the outgassing study, only a two dimensional nanopore model (slit) is used. In Chapter 3 and 4, we have studied the geometry effect on nanochannel flows by using circular and rectangular channels. To further analyze the geometry effect on outgassing (Section 7.3.3), investigating the circular and rectangular structures would be an obvious choice. However, it is difficult to create a three-dimensional geometry with a tabulated wall potential, and it would be especially challenging to do that for a circular channel. It is of course possible to follow the same steps as in Chapter 6, but a different tabulated wall potential is needed to be produced for different channel sizes, since the integration of the forces acting between an isolated gas atom and the wall atoms will differ for different wall curvatures. This is computationally very expensive. The first step can be made by following the approach by Siderius et al.^[143]. They reinterpreted the Steele 10-4-3 potential and derived a new cylindrical Steele 10-4-3 potential. It would be worthwhile to check whether their method is applicable to the tabulated wall potentials.

- *Including reactions*

In reality, reactions often happen in nanosystems for example in micro reactors or catalytic surfaces . However, with classical (non-reactive) MD this can not be taken into account. ReaxFF can not simulate a system with a size of $10 \sim 1000nm$ or larger. Therefore, an up-scaling method needs to be used. In this thesis, we have shown a potential up-scaling method from ReaxFF to classical MD (Chapter 6). However, reactions have been omitted in this process. This can be included in future research. In case of surface reactions only the reaction kinetics near the wall need to be taken into account. In order to speed up the simulations a hybrid-like method can be used here as well. One suggestion can be to create a buffer zone near the boundary, which inserts and deletes molecules based on the input reaction data that is studied by ReaxFF. By including reactions to a system with a size of $10 \sim 1000nm$ or larger, it will be possible to simulate many more processes in the semiconductor industry like contamination of photo-resistance, catalysis process, etc.

A

Pressure calculation in nanochannel flow

A.1 Pressure calculation in developing flow

The pressure calculation in Molecular Dynamics is often done by using the Irving-Kirkwood method^[76]. With this method, Barisik^[14] showed that Molecular Dynamics can predict a pressure in the nano channel system, with less than 10% difference from experimental results even for the liquid state, while ideal-gas law gives an error larger than 100% near the liquid state. According to Irving-Kirkwood method the contribution of each particle to the pressure tensor consists of two parts, a configuration part and a kinetic part:

$$P_{kl} = \frac{1}{V} \langle \sum_{i=1}^N m_i (v_k^i - v_k^{avg})(v_l^i - v_l^{avg}) - W_{kl} \rangle \quad (\text{A.1})$$

$$W_{kl} = \frac{1}{2} \sum_{i=1}^N \sum_{j=1, j \neq i}^N (r_k^j - r_k^i) f_l^{i,j} \quad (\text{A.2})$$

Local Irving-Kirkwood method is used here to check the pressure for developing flow inside the nanochannel flow. A developing flow inside a smaller and shorter slit channel with a height $H = 10nm$ and length $L = 100nm$ is simulated to test the method. Smaller scale simulation is carried out in order to check the method with shorter computational time. The simulation is started from the Maxwell-Boltzmann velocity distribution at $300K$. The walls are kept at a constant temperature $T_w = 300K$. A thermal wall condition is applied as boundary condition at the top and bottom plates.

It is found that, the cut-off radius must be chosen carefully to get an accurate value for the Irving-Kirkwood method. For our regime, a cut-off bigger than 3.5σ is required to obtain an accurate result. Figure A.2 shows the inaccuracy when a cut-off radius of 2.5σ is used.

The simulation results (Figure A.2) show that there is a difference in the pressure calculation in the region where expansion flow occurs. The absolute

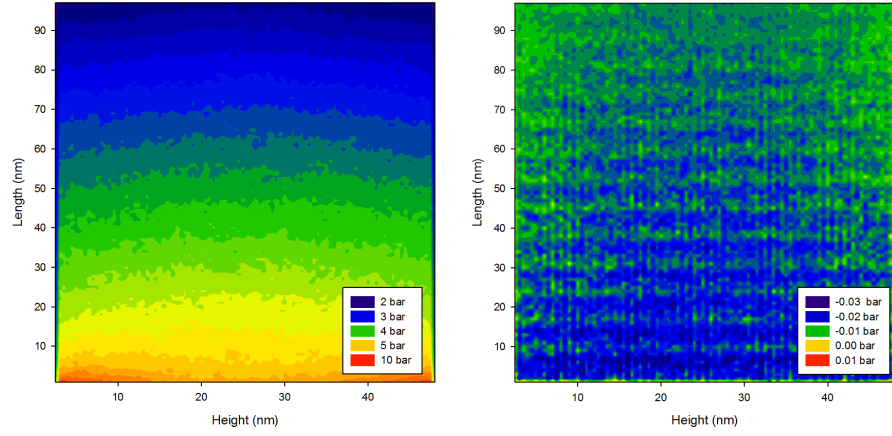


Figure A.1: Kinetic Component(left)and Virial component(right) calculated by the Irving-Kirkwood method for a slit($H = 50nm$, $L = 100nm$) flow.

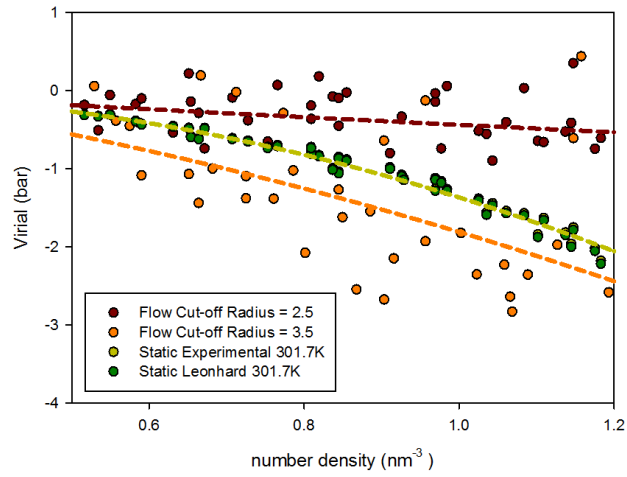


Figure A.2: Virial profile for different density at outlet in flow condition and static condition(Leonhard et al.^[99]) at $T = 300K$. Fitting curves are obtained with 2nd order polynomial equations.

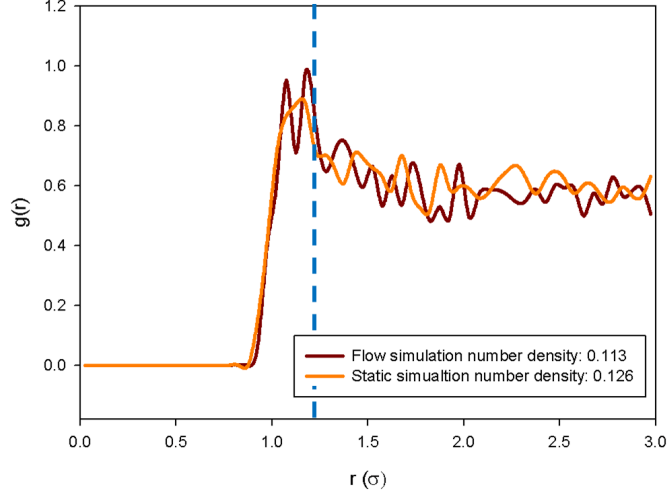


Figure A.3: RDF for flow condition and static condition.

value of the virial component showed 10 ~ 20% larger value compared to static (non-flow) situation. This is because the system is not in equal distribution at molecular scale due to a sudden change in density. Therefore, it does not have the same virial component value although static system and flow system share a same density and a same temperature.

Difference in the distribution is identified by investigating the radial distribution function (RDF). RDF describes how density varies as a function of distance from a reference particle. From RDF results (Figure A.3), it is observed that for the flow situation, more particles are close to each other compared to static situation, especially when distance between the particles is smaller than $2^{1/6} \sigma$ (dotted line). From that distance $f_i^{i,j}$ increases rapidly based on Lennard-Jones potential of argon.

However, the virial component, shown in Figure A.1, is less than 1% of kinetic component for $Kn > 1$ in 50nm nanochannel. This is less than the MD fluctuation value. This shows that effect of virial component is negligible for rarefied gas situation.

A.2 Boundary effect

Boundary effect is investigated when we study the pressure change near the wall. For smaller nanochannels, this boundary effect cannot be neglected. In our simulations we use an implicit boundary condition, where no material is modelled beyond these boundary. Therefore an artificial vacuum lies outside the channel boundary. This is the one of the main causes of a smaller absolute

Table A.1: Virial component of a static fluid as calculated by MD, inside the slit of different height, and outside the boundary is vacuum. The average particle density is kept at $0.3896nm^{-3}$, while its temperature is fixed at $300K$.

Channel height	Virial pressure component
$H = 60\sigma_{Ar}$	$-0.4040bar$
$H = 30\sigma_{Ar}$	$-0.3964bar$
$H = 15\sigma_{Ar}$	$-0.3826bar$
$H = 9\sigma_{Ar}$	$-0.3634bar$

virial component value compared to static MD simulation results.

According to Barisik's results^[14], this boundary effect lasts up to $0.5nm$. For a $10nm$ slit channel the effect will be 10% of whole channel. A test simulation is done with a static fluid inside the slit of different heights with such implicit boundary condition. The average particle density in the simulation box is fixed at $0.3896nm^{-3}$ and the temperature is fixed at $300K$. Table A.1 shows a change in virial component when the height of the channel changes from 60σ to 9σ . It shows a decrease in absolute virial component value with the decrease in channel height.

According to the study of Barisik^[14], the change in virial component is even more significant with an explicit wall. Therefore we suggest to use Irving-Kirkwood method in case of channel flow smaller than $10nm$ diameter even for a rarefied gas.

B

Expansion flow with heated walls

In addition to the results given in Chapter 4, here extra information is given for the heat transfer simulation. The inlet flow temperature is kept at a constant value of $300K$, and the channels are kept at a higher temperature at $400K$ with a thermal wall boundary condition.

Figure B.1 shows the contours of the streamwise mean velocity magnitude(left) and temperature profile(right) for all geometries calculated with MD.

B.1 Pressure

It is shown in Figure B.2 that the pressure profile is linear along the x -axis for most of the regions in the channel but the profile deviates when the flow becomes expansion flow. It is found that there is a fast increase in pressure near the inlet due to the heat transfer from the wall.

Next, pressure variation along the y -axis is studied. The normalized pressure profile near the outlet region ($x = 745nm$) is compared for the three different geometries. Simulation results are fitted with a 4th order polynomial equation. The pressure profiles for the three geometries are shown in Figure B.3. Detailed fitting parameters and error are shown in Table B.1. The slit channel shows the most flat profile while the circular channel and rectangular channel show a similar profile. Pressure is higher near the boundary because temperature is the highest near the boundary. The temperature in the center drops due to the expansion flow.

B.2 Velocity

The velocity contour graph for heat transfer flow is shown in Figure B.1. By comparing the results with Figure 4.4, velocity contour graph for isothermal

Appendix-B

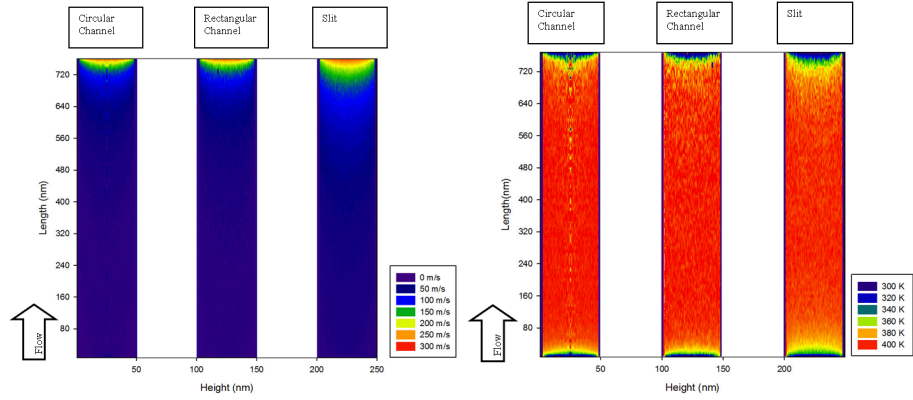


Figure B.1: Velocity contour(left) and temperature contour(right) using MD for different geometries with heated walls(wall temperature $400K$). $H = 50nm$.

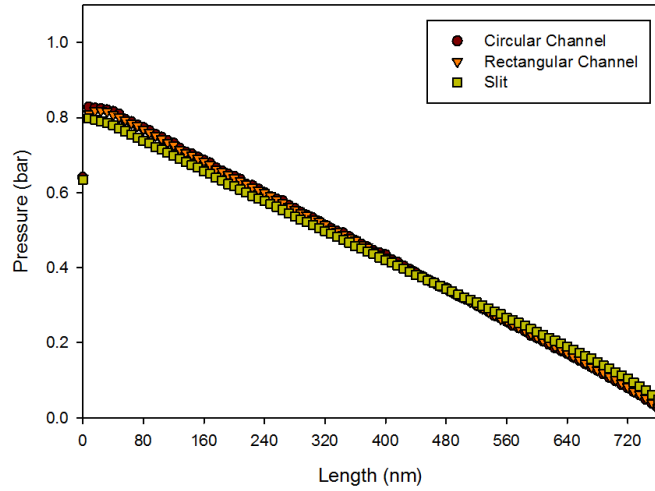


Figure B.2: Pressure profile along the channel for different geometries using MD for $T_w = 400K$. $H = 50nm$.

Table B.1: 4th order polynomial fitting of normalized pressure near the outlet region ($x = 745nm$). Normalized pressure, $P_n = P/P_{center}$ and normalized height $H_n = Y/H$.

Geometry	4th order polynomial fitting	Adj. R-Square
Circular Channel	$P_n = 1.76H_n^4 - 3.55H_n^3 + 2.96H_n^2 - 1.18H_n + 1.184$	0.66
Rectangular Channel	$P_n = 1.35H_n^4 - 2.72H_n^3 + 2.44H_n^2 - 1.08H_n + 1.189$	0.70
Slit	$P_n = 1.21H_n^4 - 2.45H_n^3 + 1.92H_n^2 - 0.69H_n + 1.110$	0.60

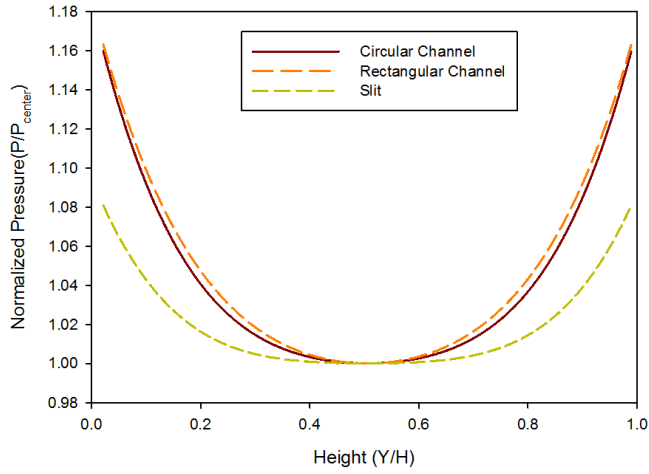


Figure B.3: Pressure profile for different geometries along the height of the channel near the outlet region ($x = 745nm$) using MD. $H = 50nm$.

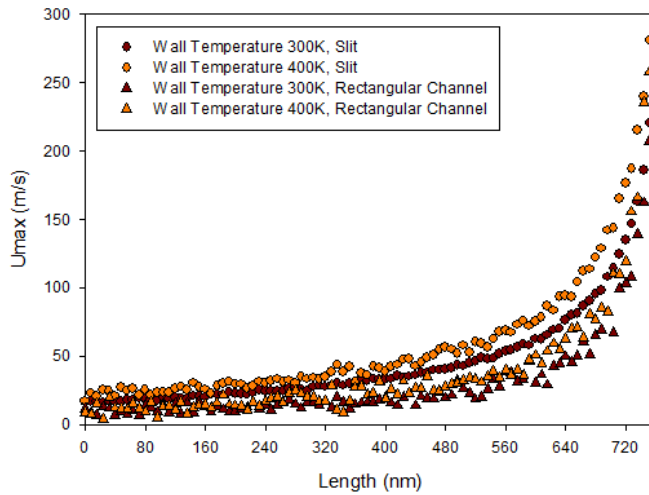


Figure B.4: Centerline velocity along the channel length for slit and rectangular geometry. Two different wall temperature (300K and 400K) and MD are used. Inlet gas temperature is 300K. $H = 50nm$.

Appendix-B

flow, an increase in the velocity drop near the outlet region is observed. Figure B.4 shows a comparison of these two situations at prescribed wall temperatures of $300K$ and $400K$. The velocity shows an increase for the heating case. This could be directly linked to the pressure increase near the inlet (Figure B.2) due to the heating.

Bibliography

- [1] <http://gasmems.eu>.
- [2] <http://pumma.nl>.
- [3] <http://vacuumtunes.co.uk>.
- [4] <http://www.originlab.com>.
- [5] Abascal, J. L. F., Sanz, E., Fernández, R. G., and Vega, C. A potential model for the study of ices and amorphous water: Tip4p/ice. *The Journal of Chemical Physics*, 122(23):234511, 2005.
- [6] Abraham, F. F. The interfacial density profile of a lennard-jones fluid in contact with a (100) lennard-jones wall and its relationship to idealized fluid/wall systems: A monte carlo simulation. *The Journal of Chemical Physics*, 68(8):3713–3716, 2008.
- [7] Akermark, T., Hultquist, G., and Lu, Q. Release of water and hydrogen during outgassing of some materials. *Journal of Materials Engineering and Performance*, 5(4):516–520, 1996.
- [8] Alexander, F. J. and Garcia, A. L. The direct simulation monte carlo method. *Computers in Physics*, 11(6):588–593, 1997.
- [9] Allen, P. and Tildesley, D. *Computer Simulation of Liquids*. Oxford Science Publ. ISBN 9780198556459.
- [10] Arkles, B. Hydrophobicity, hydrophilicity and silanes. *Paint Coatings Industry Magazine*, 22:114–132, 2006.
- [11] Aronov, D., Rosenman, G., and Barkay, Z. Wettability study of modified silicon dioxide surface using environmental scanning electron microscopy. *Journal of Applied Physics*, 101(8):084901, 2007.
- [12] Ashcroft, N. W. and Mermin, N. D. *Solid State Physics* (, 1976). Holt, Rinehart and Winston, New York, 1976.

Bibliography

- [13] Barber, R. W. and Emerson, D. R. A numerical investigation of low reynolds number gaseous slip flow at the entrance of circular and parallel plate micro-channels. In *ECCOMAS Computational Fluid Dynamics Conference*, pages 4–7, 2001.
- [14] Barisik, M. and Beskok, A. Equilibrium molecular dynamics studies on nanoscale-confined fluids. *Microfluidics and Nanofluidics*, 11(3):269–282, 2011.
- [15] Barisik, M. and Beskok, A. Wetting characterisation of silicon (1, 0, 0) surface. *Molecular Simulation*, 39(9):700–709, 2013.
- [16] Barisik, M., Kim, B., and Beskok, A. Smart wall model for molecular dynamicssimulations of nanoscale gas flows. *Communications in Computational Physics*, 7:977–993, 2010.
- [17] Berendsen, H. J. C., Grigera, J. R., and Straatsma, T. P. The missing term in effective pair potentials. *Journal of Physical Chemistry*, 91(24):6269–6271, 1987.
- [18] Berendsen, H. J. C., Postma, J. P. M., Van Gunsteren, W. F., and Hermans, J. Interaction models for water in relation to protein hydration. In *Intermolecular Forces*, pages 331–342. Springer, 1981.
- [19] Beskok, A., Trimmer, W., and Karniadakis, G. E. Rarefaction and compressibility effects in gas microflows. *Journal of Fluids Engineering*, 118(3):448–456, 1996.
- [20] Bird, G. A. *Molecular Gas Dynamics and the Direct Simulation of Gas Flows*. Oxford science publications. ISBN 9780198561958.
- [21] Bird, R. B., Stewart, W. E., and Lightfoot, E. N. *Transport phenomena*. John Wiley & Sons, 2007.
- [22] Bitsanis, I., Magda, J. J., Tirrell, M., and Davis, H. T. Molecular dynamics of flow in micropores. *The Journal of Chemical Physics*, 87(3):1733–1750, 1987.
- [23] Borg, M. K., Macpherson, G. B., and Reese, J. M. Controllers for imposing continuum-to-molecular boundary conditions in arbitrary fluid flow geometries. *Molecular Simulation*, 36(10):745–757, 2010.
- [24] Brennan, J. K., Bandosz, T. J., Thomson, K. T., and Gubbins, K. E. Water in porous carbons. *Colloids and Surfaces A: Physicochemical and Engineering Aspects*, 187:539–568, 2001.
- [25] Brunauer, S., Emmett, P. H., and Teller, E. Adsorption of gases in multimolecular layers. *Journal of the American Chemical Society*, 60(2):309–319, 1938.

- [26] Calder, R. S. and Lewin, G. Reduction of stainless-steel outgassing in ultra-high vacuum. *British Journal of Applied Physics*, 18(10):1459, 1967.
- [27] Cao, B.-Y., Chen, M., and Guo, Z.-Y. Effect of surface roughness on gas flow in microchannels by molecular dynamics simulation. *International Journal of Engineering Science*, 44(13):927–937, 2006.
- [28] Car, R. and Parrinello, M. Unified approach for molecular dynamics and density-functional theory. *Physical Review Letters*, 55(22):2471, 1985.
- [29] Carey, V. *Statistical Thermodynamics and Microscale Thermophysics*. ISBN 9780521654203.
- [30] Carter, R. S., Rush, J. J., and for Materials Research (U.S.), I. *Molecular Dynamics and Structure of Solids*. NBS special publication.
- [31] Cercignani, C. and Pagani, C. D. Variational approach to rarefied flows in cylindrical and spherical geometry. In *Rarefied Gas Dynamics, Volume 1*, volume 1, page 555, 1967.
- [32] Cercignani, C. Higher order slip according to the linearized boltzmann equation. Technical report, DTIC Document, 1964.
- [33] Cercignani, C. and Lampis, M. Kinetic models for gas-surface interactions. *Transport Theory and Statistical Physics*, 1(2):101–114, 1971.
- [34] Chapra, S. C. and Canale, R. P. *Numerical methods for engineers: with software and programming applications*. ISBN 9780072431933.
- [35] Charvet, P.-L., Nicolas, P., Bloch, D., and Savornin, B. Mems packaging reliability assessment: Residual gas analysis of gaseous species trapped inside mems cavities. *Microelectronics Reliability*, 53(9):1622–1627, 2013.
- [36] Chen, J., McAllister, M. A., Lee, J. K., and Houk, K. N. Short, strong hydrogen bonds in the gas phase and in solution: Theoretical exploration of pka matching and environmental effects on the strengths of hydrogen bonds and their potential roles in enzymatic catalysis. *The Journal of Organic Chemistry*, 63(14):4611–4619, 1998.
- [37] Chenoweth, K., van Duin, A. C. T., and Goddard, W. A. Reaxff reactive force field for molecular dynamics simulations of hydrocarbon oxidation. *The Journal of Physical Chemistry A*, 112(5):1040–1053, 2008.
- [38] Colin, S. Rarefaction and compressibility effects on steady and transient gas flows in microchannels. *Microfluidics and Nanofluidics*, 1(3):268–279, 2005.
- [39] Cracknell, R. F., Nicholson, D., and Gubbins, K. E. Molecular dynamics study of the self-diffusion of supercritical methane in slit-shaped graphitic micropores. *Journal of the Chemical Society, Faraday Transactions*, 91(9):1377–1383, 1995.

Bibliography

- [40] Dang, L. X. and Pettitt, B. M. Simple intramolecular model potentials for water. *Journal of Physical Chemistry*, 91(12):3349–3354, 1987.
- [41] De Gennes, P.-G. Wetting: statics and dynamics. *Reviews of modern physics*, 57(3):827, 1985.
- [42] De Ruijter, M. J., Blake, T. D., and De Coninck, J. Dynamic wetting studied by molecular modeling simulations of droplet spreading. *Langmuir*, 15(22):7836–7847, 1999.
- [43] De Segovia, J. L. Physics of outgassing. *CERN European Organization for Nuclear Research-Reports-CERN*, pages 99–110, 1999.
- [44] de Vos Burchart, E. *Studies on Zeolites; Molecular Mechanics, Framework Stability and Crystal Growth*. PhD thesis, Delft University of Technology, 1992.
- [45] Deissler, R. G. An analysis of second-order slip flow and temperature-jump boundary conditions for rarefied gases. *International Journal of Heat and Mass Transfer*, 7(6):681–694, 1964.
- [46] Delhommelle, J. and Millié, P. Inadequacy of the lorentz-berthelot combining rules for accurate predictions of equilibrium properties by molecular simulation. *Molecular Physics*, 99(8):619–625, 2001.
- [47] Dongari, N., Durst, F., and Chakraborty, S. Predicting microscale gas flows and rarefaction effects through extended navier–stokes–fourier equations from phoretic transport considerations. *Microfluidics and Nanofluidics*, 9(4-5):831–846, 2010.
- [48] Downs, R. T. and Palmer, D. C. The pressure behavior of α -cristobalite. *Am Mineral*, 79:9–14, 1994.
- [49] Duan, Z. Second-order gaseous slip flow models in long circular and non-circular microchannels and nanochannels. *Microfluidics and Nanofluidics*, 12(5):805–820, 2012.
- [50] Duan, Z. and Muzychka, Y. S. Slip flow in the hydrodynamic entrance region of circular and noncircular microchannels. *Journal of Fluids Engineering*, 132(1):011201, 2010.
- [51] Ewald, P. The calculation of optical and electrostatic grid potential. *Ann. Phys.*, 64(3):253–287, 1921.
- [52] Ewart, T., Perrier, P., Graur, I. A., and Méolans, J. G. Mass flow rate measurements in a microchannel, from hydrodynamic to near free molecular regimes. *Journal of Fluid Mechanics*, 584:337–356, 2007.
- [53] Fang, Y. and Liou, W. W. Computations of the flow and heat transfer in microdevices using dsmc with implicit boundary conditions. *Journal of Heat Transfer*, 124(2):338–345, 2002.

-
- [54] Fick, A. Ueber diffusion. *Annalen der Physik*, 170(1):59–86, 1855.
- [55] Firpo, G., Repetto, L., de Mongeot, F. B., and Valbusa, U. Focused-ion beam fabrication of nanometer orifices for leak detection. *Journal of Vacuum Science & Technology B*, 27(6):2347–2350, 2009.
- [56] Fogarty, J. C., Aktulga, H. M., Grama, A. Y., Van Duin, A. C. T., and Pandit, S. A. A reactive molecular dynamics simulation of the silica-water interface. *The Journal of Chemical Physics*, 132(17):174704, 2010.
- [57] Fox, R. W., McDonald, A. T., and Pritchard, P. J. *Introduction to fluid mechanics*, volume 5. John Wiley & Sons New York, 1998.
- [58] Frezzotti, A. A particle scheme for the numerical solution of the Enskog equation. *Physics of Fluids (1994-present)*, 9(5):1329–1335, 1997.
- [59] Gad-el Hak, M. Flow physics in MEMS. *Mécanique & industries*, 2(4):313–341, 2001.
- [60] Gao, F., Hokkanen, A., Pekko, P., Kärkkäinen, A., and Kiihamäki, J. Outgassing of water molecules during silicon fusion bonding. *Physics Procedia*, 32:628–634, 2012.
- [61] Garcia, A. L. and Baras, F. Direct simulation Monte Carlo: novel applications and new extensions. In *Proceedings of the 3rd Workshop on Modelling of Chemical Reaction Systems, Heidelberg*, 1997.
- [62] Glowinski, R. and Lichnerowicz, A. *Computing Methods in Applied Sciences and Engineering*. Society for Industrial and Applied Mathematics, 1990. ISBN 9780898712643.
- [63] Graur, I. A., Perrier, P., Ghoulani, W., and Méolans, J. G. Measurements of tangential momentum accommodation coefficient for various gases in plane microchannel. *Physics of Fluids*, 21(10):102004, 2009.
- [64] Graur, I. and Sharipov, F. Gas flow through an elliptical tube over the whole range of the gas rarefaction. *European Journal of Mechanics-B/Fluids*, 27(3):335–345, 2008.
- [65] Gravesen, P., Branebjerg, J., and Jensen, O. S. Microfluidics—a review. *Journal of Micromechanics and Microengineering*, 3(4):168, 1993.
- [66] Hadjiconstantinou, N. G. Comment on Cercignani’s second-order slip coefficient. *Physics of Fluids*, 15(8):2352–2354, 2003.
- [67] Hanasaki, I. and Nakatani, A. Fluidized piston model for molecular dynamics simulations of hydrodynamic flow. *Modelling and simulation in materials science and engineering*, 14(5):S9, 2006.

Bibliography

- [68] Hässig, M., Altwegg, K., Balsiger, H., Calmonte, U., Jäckel, A., Schläppi, B., Sémon, T., Wurz, P., Berthelier, J.-J., De Keyser, J., et al. Spacecraft outgassing, a largely underestimated phenomenon. In *2nd International Conference on Space Technology (ICST)*, 2011.
- [69] Heaney, P. J. Structure and chemistry of the low-pressure silica polymorphs. *Reviews in Mineralogy and Geochemistry*, 29(1):1–40, 1994.
- [70] Heaney, P. J., Veblen, D. R., and Post, J. E. Structural disparities between chalcedony and macrocrystalline quartz. *American Mineralogist*, 79(5-6): 452–460, 1994.
- [71] Hill, T. *An Introduction to Statistical Thermodynamics*. Dover Books on Physics. ISBN 9780486130903.
- [72] Hloucha, M. *Global simulations of the simple liquids Ne, Ar, N₂ and CO*. PhD thesis, University of Koln, 1998.
- [73] Horn, H. W., Swope, W. C., Pitera, J. W., Madura, J. D., Dick, T. J., Hura, G. L., and Head-Gordon, T. Development of an improved four-site water model for biomolecular simulations: Tip4p-ew. *The Journal of chemical physics*, 120(20):9665–9678, 2004.
- [74] Hove, J. and Krumhansl, J. A. The evaluation of lattice sums for cubic crystals. *Physical Review*, 92(3):569, 1953.
- [75] Ierardi, V., Firpo, G., and Valbusa, U. Nano-holes for vacuum applications. In *Journal of Physics: Conference Series*, volume 439, page 012033. IOP Publishing, 2013.
- [76] Irving, J. H. and Kirkwood, J. G. The statistical mechanical theory of transport processes. iv. the equations of hydrodynamics. *The Journal of Chemical Physics*, 18(6):817–829, 2004.
- [77] Ishikawa, Y. and Odaka, K. Reduction of outgassing from stainless surfaces by surface oxidation. *Vacuum*, 41(7):1995–1997, 1990.
- [78] Ishikawa, Y. and Yoshimura, T. Importance of the surface oxide layer in the reduction of outgassing from stainless steels. *Journal of Vacuum Science & Technology A*, 13(4):1847–1852, 1995.
- [79] Ishikawa, Y., Koguchi, Y., and Odaka, K. Outgassing rate of some austenitic stainless steels. *Journal of Vacuum Science & Technology A*, 9(2):250–253, 1991.
- [80] Iype, E., Hütter, M., Jansen, A. P. J., Nedeia, S. V., and Rindt, C. C. M. Parameterization of a reactive force field using a monte carlo algorithm. *Journal of Computational Chemistry*, 34(13):1143–1154, 2013.

-
- [81] Iype, E., Nedea, S. V., Rindt, C. C. M., van Steenhoven, A. A., Zondag, H. A., and Jansen, A. P. J. Dft study on characterization of hydrogen bonds in the hydrates of mgso4. *The Journal of Physical Chemistry C*, 116(35):18584–18590, 2012.
- [82] Jang, J. and Kim, Y.-H. Gaseous slip flow of a rectangular microchannel with non-uniform slip boundary conditions. *Microfluidics and Nanofluidics*, 9(2-3):513–522, 2010.
- [83] Jeong, N., Lin, C.-L., and Choi, D. H. Lattice boltzmann study of three-dimensional gas microchannel flows. *Journal of Micromechanics and Microengineering*, 16(9):1749, 2006.
- [84] Jorgensen, W. L. and Jenson, C. Temperature dependence of tip3p, spc, and tip4p water from npt monte carlo simulations: Seeking temperatures of maximum density. *Journal of Computational Chemistry*, 19(10):1179–1186, 1998.
- [85] Jorgensen, W. L., Chandrasekhar, J., Madura, J. D., Impey, R. W., and Klein, M. L. Comparison of simple potential functions for simulating liquid water. *The Journal of Chemical Physics*, 79(2):926–935, 1983.
- [86] Jousten, K. Thermal outgassing. *CERN European Organization for Nuclear Research-Reports-CERN*, pages 111–126, 1999.
- [87] Kaburaki, H. and Yokokawa, M. Computer simulation of two-dimensional continuum flows by the direct simulation monte carlo method. *Molecular Simulation*, 12(3-6):441–444, 1994.
- [88] Kanta, A., Sedev, R., and Ralston, J. Thermally-and photoinduced changes in the water wettability of low-surface-area silica and titania. *Langmuir*, 21(6):2400–2407, 2005.
- [89] Karniadakis, G. E., Beskok, A., and Aluru, N. R. *Microflows and nanoflows: fundamentals and simulation*. Interdisciplinary Applied Mathematics. ISBN 9780387908199.
- [90] Kim, B. S., Shin, S., Shin, S. J., Kim, K. M., and Cho, H. H. Micro-nano hybrid structures with manipulated wettability using a two-step silicon etching on a large area. *Nanoscale Research Letters*, 6(1):1–10, 2011.
- [91] Kim, J., Frijns, A. J. H., Nedea, S. V., and Steenhoven, A. A. Geometry effects on rarefied nanochannel flows. *Microfluidics and Nanofluidics*, 15(5):661–673, 2013. ISSN 1613-4982. doi: 10.1007/s10404-013-1181-1.
- [92] Koura, K. A sensitive test for accuracy in evaluation of molecular collision number in the direct-simulation monte carlo method. *Physics of Fluids A: Fluid Dynamics (1989-1993)*, 2(7):1287–1289, 1990.

Bibliography

- [93] Koura, K. and Matsumoto, H. Variable soft sphere molecular model for inverse-power-law or lennard-jones potential. *Physics of Fluids A: Fluid Dynamics (1989-1993)*, 3(10):2459–2465, 1991.
- [94] Krishnan, S. H. and Ayappa, K. G. Modeling velocity autocorrelation functions of confined fluids: A memory function approach. *The Journal of Chemical Physics*, 118(2):690–705, 2002.
- [95] Krynicki, K., Green, C. D., and Sawyer, D. W. Pressure and temperature dependence of self-diffusion in water. *Faraday Discussions of the Chemical Society*, 66:199–208, 1978.
- [96] Langmuir, I. the constitution and fundamental properties of solids and liquids. part i. solids. *Journal of the American Chemical Society*, 38(11):2221–2295, 1916.
- [97] Lee, S. H. Temperature dependence on structure and self-diffusion of water: A molecular dynamics simulation study using spc/e model. *Bull. Korean Chem. Soc*, 34(12):3801, 2013.
- [98] Lennard-Jones, J. E. and Devonshire, A. F. Critical phenomena in gases. i. *Proceedings of the Royal Society of London. Series A, Mathematical and Physical Sciences*, pages 53–70, 1937.
- [99] Leonhard, K. and Deiters, U. K. Monte carlo simulations of neon and argon using ab initio potentials. *Molecular Physics*, 98(20):1603–1616, 2000.
- [100] Levitt, M., Hirshberg, M., Sharon, R., Laidig, K. E., and Daggett, V. Calibration and testing of a water model for simulation of the molecular dynamics of proteins and nucleic acids in solution. *The Journal of Physical Chemistry B*, 101(25):5051–5061, 1997.
- [101] Li, W. and Gu, T. Equilibrium contact angles as a function of the concentration of nonionic surfactants on quartz plate. *Colloid and Polymer Science*, 263(12):1041–1043, 1985.
- [102] Liang, Z. and Tsai, H.-L. A method to generate pressure gradients for molecular simulation of pressure-driven flows in nanochannels. *Microfluidics and Nanofluidics*, 13(2):289–298, 2012.
- [103] Lindroos, V., Franssila, S., Tilli, M., Paulasto-Krockel, M., Lehto, A., Motooka, T., and Airaksinen, V.-M. *Handbook of silicon based MEMS materials and technologies*. Elsevier, 2009.
- [104] Liou, W. W. and Fang, Y. Heat transfer in microchannel devices using dsmc. *Microelectromechanical Systems, Journal of*, 10(2):274–279, 2001.

-
- [105] Liu, J. Q., Tai, Y.-C., Pong, K.-C., and Ho, C.-M. Micromachined channel/pressure sensor systems for micro flow studies. *Proceedings of the 7th International Conference on Solid-State Sensors and Actuators*, 93: 995–99, 1993.
- [106] Madey, T. E., Faradzhev, N. S., Yakshinskiy, B. V., and Edwards, N. V. Surface phenomena related to mirror degradation in extreme ultraviolet (euv) lithography. *Applied Surface Science*, 253(4):1691–1708, 2006.
- [107] Mahoney, M. W. and Jorgensen, W. L. A five-site model for liquid water and the reproduction of the density anomaly by rigid, nonpolarizable potential functions. *The Journal of Chemical Physics*, 112(20):8910–8922, 2000.
- [108] Mark, P. and Nilsson, L. Structure and dynamics of the tip3p, spc, and spc/e water models at 298 k. *The Journal of Physical Chemistry A*, 105(43):9954–9960, 2001.
- [109] Mark, P. and Nilsson, L. Structure and dynamics of liquid water with different long-range interaction truncation and temperature control methods in molecular dynamics simulations. *Journal of Computational Chemistry*, 23(13):1211–1219, 2002.
- [110] Markvoort, A. J., Smeijers, A. F., Pieterse, K., van Santen, R. A., and Hilbers, P. A. J. Lipid-based mechanisms for vesicle fission. *The Journal of Physical Chemistry B*, 111(20):5719–5725, 2007.
- [111] Maruyama, S. Molecular dynamics method for microscale heat transfer. *Advances in Numerical Heat Transfer*, 2(6):189–226, 2000.
- [112] Matsumoto, S., Maruyama, S. T. Kurashige, Kimura, Y., and Yamaguchi, T. Liquid droplet in contact with a solid surface. *Microscale Thermophysical Engineering*, 2(1):49–62, 1998.
- [113] McMullin, D. R., Judge, D. L., Hilchenbach, M., Ipavich, F., Bochsler, P., Wurz, P., Bürgi, A., Thompson, W. T., and Newmark, J. S. In-flight comparisons of solar euv irradiance measurements provided by the celsius/sem on soho. *Radiometric Calibration of SOHO, ISSI Sci. Rep. SR*, 2:135–144, 2002.
- [114] Meller, J. et al. Molecular dynamics. *Encyclopedia of Life Sciences*, 2001.
- [115] Mendoza, F. N., López-Lemus, J., Chapela, G. A., and Alejandre, J. The wolf method applied to the liquid-vapor interface of water. *The Journal of chemical physics*, 129(2):024706, 2008.
- [116] Menegon, G., Shimizu, K., Farah, J. P. S., Dias, L. G., and Chaimovich, H. Parameterization of the electronegativity equalization method based on the charge model 1. *Physical Chemistry Chemical Physics*, 4(24):5933–5936, 2002.

Bibliography

- [117] Naris, S., Valougeorgis, D., Kalempa, D., and Sharipov, F. Flow of gaseous mixtures through rectangular microchannels driven by pressure, temperature, and concentration gradients. *Physics of Fluids*, 17(10):100607, 2005.
- [118] Nedeá, S. V., Frijns, A. J. H., van Steenhoven, A. A., Markvoort, A. J., and Hilbers, P. A. J. Hybrid method coupling molecular dynamics and monte carlo simulations to study the properties of gases in microchannels and nanochannels. *Physical Review E*, 72:016705, Jul 2005. doi: 10.1103/PhysRevE.72.016705.
- [119] Nedeá, S. V., Markvoort, A. J., van Steenhoven, A. A., and Hilbers, P. A. J. Heat transfer predictions for micro-/nanochannels at the atomistic level using combined molecular dynamics and monte carlo techniques. *Journal of Heat Transfer*, 131(3):033104, 2009.
- [120] Neria, E., Fischer, S., and Karplus, M. Simulation of activation free energies in molecular systems. *The Journal of Chemical Physics*, 105(5): 1902–1921, 1996.
- [121] O’Hanlon, J. F. *A User’s Guide to Vacuum Technology*. ISBN 9780471467151.
- [122] Oran, E. S., Oh, C. K., and Cybyk, B. Z. Direct simulation monte carlo: Recent advances and applications 1. *Annual Review of Fluid Mechanics*, 30(1):403–441, 1998.
- [123] Ouyang, Y., Ye, F., and Liang, Y. A modified electronegativity equalization method for fast and accurate calculation of atomic charges in large biological molecules. *Physical Chemistry Chemical Physics*, 11(29):6082–6089, 2009.
- [124] Pashley, R. M. and Kitchener, J. A. Surface forces in adsorbed multilayers of water on quartz. *Journal of Colloid and Interface Science*, 71(3):491–500, 1979.
- [125] Pong, K.-C., Ho, C.-M., Liu, J., and Tai, Y.-C. Non-linear pressure distribution in uniform microchannels. *ASME-PUBLICATIONS-FED*, 197: 51–51, 1994.
- [126] Price, W. S., Ide, H., and Arata, Y. Self-diffusion of supercooled water to 238 k using pgse nmr diffusion measurements. *The Journal of Physical Chemistry A*, 103(4):448–450, 1999.
- [127] Quinn, M. J. *Parallel Programming*, volume 526. TMH CSE, 2003.
- [128] Raabe, G. and Sadus, R. J. Influence of bond flexibility on the vapor-liquid phase equilibria of water. *The Journal of Chemical Physics*, 126(4): 044701, 2007.

-
- [129] Raabe, G. and Sadus, R. J. Molecular dynamics simulation of the effect of bond flexibility on the transport properties of water. *The Journal of Chemical Physics*, 137(10):104512, 2012.
- [130] Reed, J. L. Electronegativity and atomic charge. *Journal of Chemical Education*, 69(10):785, 1992.
- [131] Reese, J. M. and Zhang, Y. Simulating fluid flows in micro and nano devices: the challenge of non-equilibrium behaviour. *Journal of Computational and Theoretical Nanoscience*, 6(10):2061–2074, 2009.
- [132] Roohi, E., Darbandi, M., and Mirjalili, V. Direct simulation monte carlo solution of subsonic flow through micro/nanoscale channels. *Journal of Heat Transfer*, 131(9):092402, 2009.
- [133] Ryckaert, J.-P., Ciccotti, G., and Berendsen, H. J. C. Numerical integration of the cartesian equations of motion of a system with constraints: molecular dynamics of *n*-alkanes. *Journal of Computational Physics*, 23(3):327–341, 1977.
- [134] Rykov, V. A., Titarev, V. A., and Shakhov, E. M. Rarefied poiseuille flow in elliptical and rectangular tubes. *Fluid Dynamics*, 46(3):456–466, 2011.
- [135] Schaaf, S. A. and Chambré, P. L. *Flow of rarefied gases*. Princenton University Press, 1961.
- [136] Schläppi, B., Altwegg, K., Balsiger, H., Hässig, M., Jäckel, A., Wurz, P., Fiethe, B., Rubin, M., Fuselier, S. A., Bertheliet, J.-J., et al. Influence of spacecraft outgassing on the exploration of tenuous atmospheres with in situ mass spectrometry. *Journal of Geophysical Research: Space Physics* (1978–2012), 115(A12), 2010.
- [137] Senn, B. C., Pigram, P. J., and Liesegang, J. Surface electrical resistivity and wettability study of fused silica. *Surface and Interface Analysis*, 27(9):835–839, 1999.
- [138] Sharipov, F. Rarefied gas flow through a long rectangular channel. *Journal of Vacuum Science & Technology A*, 17(5):3062–3066, 1999.
- [139] Sharipov, F. Data on the velocity slip and temperature jump on a gas-solid interface. *Journal of Physical and Chemical Reference Data*, 40(2):023101, 2011.
- [140] Shen, C., Tian, D.-B., Xie, C., and Fan, J. Examination of the lbm in simulation of microchannel flow in transitional regime. *Microscale Thermophysical Engineering*, 8(4):423–432, 2004.
- [141] Shi, B. and Dhir, V. K. Molecular dynamics simulation of the contact angle of liquids on solid surfaces. *The Journal of Chemical Physics*, 130(3):034705, 2009.

Bibliography

- [142] Shi, B., Sinha, S., and Dhir, V. K. Molecular dynamics simulation of the density and surface tension of water by particle-particle particle-mesh method. *The Journal of Chemical Physics*, 124(20):204715, 2006.
- [143] Siderius, D. W. and Gelb, L. D. Extension of the steale 10-4-3 potential for adsorption calculations in cylindrical, spherical, and other pore geometries. *The Journal of Chemical Physics*, 135(8):084703, 2011.
- [144] Skeel, R. D. Variable step size destabilizes the störmer/leapfrog/verlet method. *BIT Numerical Mathematics*, 33(1):172–175, 1993.
- [145] Smeijers, A. F., Pieterse, K., Markvoort, A. J., and Hilbers, P. A. J. Coarse-grained transmembrane proteins: hydrophobic matching, aggregation, and their effect on fusion. *The Journal of Physical Chemistry B*, 110(27):13614–13623, 2006.
- [146] Soper, A. K. Bridge over troubled water: the apparent discrepancy between simulated and experimental non-ambient water structure. *Journal of Physics: Condensed Matter*, 8(47):9263, 1996.
- [147] Spiga, M. and Morino, G. L. A symmetric solution for velocity profile in laminar flow through rectangular ducts. *International Communications in Heat and Mass Transfer*, 21(4):469–475, 1994.
- [148] Spijker, P., ten Eikelder, H. M. M., Markvoort, A. J., Nedeá, S. V., and Hilbers, P. A. J. Implicit particle wall boundary condition in molecular dynamics. *Proceedings of the Institution of Mechanical Engineers, Part C: Journal of Mechanical Engineering Science*, 222(5):855–864, 2008.
- [149] Srinivasan, S. G., Ashok, I., Jonsson, H., Kalonji, G., and Zahorjan, J. Dynamic-domain-decomposition parallel molecular dynamics. *Computer Physics Communications*, 102(1):44–58, 1997.
- [150] Starin, S. R., O'Donnell Jr, J. R., Ward, D. K., Wollack, E. J., Bay, P. M., and Fink, D. R. An anomalous force on the map spacecraft. In *2002 AIAA Guidance, Navigation and Control Conference*, 2002.
- [151] Steele, W. A. *The interaction of gases with solid surfaces*, volume 3. Pergamon Press Oxford, 1974.
- [152] Suetin, P., Porodnov, B., Chernjak, V., and Borisov, S. Poiseuille flow at arbitrary knudsen numbers and tangential momentum accommodation. *Journal of Fluid Mechanics*, 60(03):581–592, 1973.
- [153] Sun, J., He, Y. L., Tao, W. Q., Rose, J. W., and Wang, H. S. Multi-scale study of liquid flow in micro/nanochannels: effects of surface wettability and topology. *Microfluidics and Nanofluidics*, 12(6):991–1008, 2012.
- [154] Sun, Z.-X., Tang, Z., He, Y.-L., and Tao, W.-Q. Proper cell dimension and number of particles per cell for dsmc. *Computers & Fluids*, 50(1):1–9, 2011.

-
- [155] Takahashi, K. Z. Truncation effects of shift function methods in bulk water systems. *Entropy*, 15(8):3249–3264, 2013.
- [156] To, Q. D., Bercegeay, C., Lauriat, G., Léonard, C., and Bonnet, G. A slip model for micro/nano gas flows induced by body forces. *Microfluidics and Nanofluidics*, 8(3):417–422, 2010.
- [157] Toukan, K. and Rahman, A. Molecular-dynamics study of atomic motions in water. *Physical Review B*, 31:2643–2648, 1985.
- [158] Toxvaerd, S. The structure and thermodynamics of a solid–fluid interface. *The Journal of Chemical Physics*, 74(3):1998–2005, 1981.
- [159] Travis, K. P. and Gubbins, K. E. Transport diffusion of oxygen-nitrogen mixtures in graphite pores: A nonequilibrium molecular dynamics (nemd) study. *Langmuir*, 15(18):6050–6059, 1999.
- [160] Tuller, M., Or, D., and Dudley, L. M. Adsorption and capillary condensation in porous media: Liquid retention and interfacial configurations in angular pores. *Water Resources Research*, 35(7):1949–1964, 1999.
- [161] Tzeng, P.-Y., Chen, P.-H., and Liu, M.-H. Numerical investigation of gaseous microchannel flow in transition regimes. *Journal of Flow Visualization and Image Processing*, 12(1), 2005.
- [162] van den Akker, E. A. T. *Particle-based Evaporation Models and Wall Interaction for Microchannel Cooling*. PhD thesis, Eindhoven University of Technology, 2010.
- [163] van den Akker, E. A. T., Frijns, A. J. H., Hilbers, P. A. J., and van Steenhoven, A. A. A molecular dynamics boundary condition for heat exchange between walls and a fluid. *Molecular Simulation*, 37(10):855–864, 2011.
- [164] van den Akker, E. A. T., Frijns, A. J. H., Kunkelmann, C., Hilbers, P. A. J., Stephan, P., and van Steenhoven, A. A. Molecular dynamics simulation of the microregion. *International Journal of Thermal Sciences*, 59: 21–28, 2012.
- [165] Van Duin, A. C. T., Dasgupta, S., Lorant, F., and Goddard, W. A. Reaxff: a reactive force field for hydrocarbons. *The Journal of Physical Chemistry A*, 105(41):9396–9409, 2001.
- [166] Van Duin, A. C. T., Strachan, A., Stewman, S., Zhang, Q., Xu, X., and Goddard, W. A. Reaxffsio reactive force field for silicon and silicon oxide systems. *The Journal of Physical Chemistry A*, 107(19):3803–3811, 2003.
- [167] Verlet, L. Computer "Experiments" on Classical Fluids. I. Thermodynamical Properties of Lennard-Jones Molecules. *Physical Review*, 159:98–103, July 1967. doi: 10.1103/PhysRev.159.98.

Bibliography

- [168] Wagner, W. A convergence proof for bird's direct simulation monte carlo method for the boltzmann equation. *Journal of Statistical Physics*, 66 (3-4):1011–1044, 1992.
- [169] Washburn, E. W., West, C. J., and Hull, C. *International Critical Tables*, volume III. McGraw-Hill, New York, 1928.
- [170] Werder, T., Walther, J. H., Jaffe, R. L., Halicioglu, T., and Koumoutsakos, P. On the water-carbon interaction for use in molecular dynamics simulations of graphite and carbon nanotubes. *The Journal of Physical Chemistry B*, 107(6):1345–1352, 2003.
- [171] Will, G., Bellotto, M., Parrish, W., and Hart, M. Crystal structures of quartz and magnesium germanate by profile analysis of synchrotron-radiation high-resolution powder data. *Journal of Applied Crystallography*, 21(2):182–191, 1988.
- [172] Williams, R. and Goodman, A. M. Wetting of thin layers of sio₂ by water. *Applied Physics Letters*, 25(10):531–532, 2003.
- [173] Wisniak, J. Heike kamerlingh the virial equation of state. *Indian Journal of Chemical Technology*, 10(5):564–572, 2003.
- [174] Wolff, D. and Rudd, W. G. Tabulated potentials in molecular dynamics simulations. *Computer Physics Communications*, 120(1):20–32, 1999.
- [175] Wu, Y., Tepper, H. L., and Voth, G. A. Flexible simple point-charge water model with improved liquid-state properties. *The Journal of Chemical Physics*, 124(2):024503, 2006.
- [176] Xue, H., Fan, Q., and Shu, C. Prediction of micro-channel flows using direct simulation monte carlo. *Probabilistic Engineering Mechanics*, 15 (2):213–219, 2000.
- [177] Yamamoto, K., Takeuchi, H., and Hyakutake, T. Characteristics of reflected gas molecules at a solid surface. *Physics of Fluids (1994-present)*, 18(4):046103, 2006.
- [178] Yoshida, K., Wakai, C., Matubayasi, N., and Nakahara, M. A new high-temperature multinuclear-magnetic-resonance probe and the self-diffusion of light and heavy water in sub-and supercritical conditions. *The Journal of Chemical Physics*, 123(16):164506, 2005.
- [179] Zarkova, L., Hohm, U., and Damyanova, M. Comparison of lorentz–berthelot and tang–toennies mixing rules using an isotropic temperature-dependent potential applied to the thermophysical properties of binary gas mixtures of ch₄, cf₄, sf₆, and c (ch₃)₄ with ar, kr, and xe. *International Journal of Thermophysics*, 25(6):1775–1798, 2004.

- [180] Ziarani, A. S. and Mohamad, A. A. A molecular dynamics study of perturbed poiseuille flow in a nanochannel. *Microfluidics and Nanofluidics*, 2(1):12–20, 2006.

Symbols

Symbol	Description	Unit
g	Gravity	m/s^2
k	Coulomb's constant	$N \cdot m^2/C^2$
k_B	Boltzmann constant	J/K
l	Bond length	nm
m	Mass	kg
n	Number density	—
q	Charge	e
q_w	Heat flux at a wall	$J/m \cdot s$
r	Distance	nm
r_c	Cut-off radius	nm
v	Particle velocity	m/s
x	x -coordinate	nm
y	y -coordinate	nm
z	z -coordinate	nm
A	Area	nm^2
B	Virial-coefficient	—
B_2	Second virial-coefficient	—
BO	Bond order	—
D	Self-diffusion coefficient	mm^2/s
D_o	Temperature-independent pre-exponential	—
E	Energy	J
E_a	Activation energy	J
F	Force	N
H	Height	nm
IT	Iteration step	—
J_E	Collision integral for Enskog equation	—
K_l	Bond spring constant	$kcal \text{ mol}^{-1} \text{ \AA}^{-2}$
K_θ	Angle constant	$kcal \text{ mol}^{-1} \text{ rad}^{-2}$
KE	Kinetic energy	J
Kn	Knudsen number	—
L	Length	nm

Nomenclature

Symbol	Description	Unit
N	Number of particles	–
P	Pressure	<i>bar</i>
P_{coll}	Collision probability	–
Q	Volume flow rate	m^3/s
T	Temperature	<i>K</i>
T_w	Wall temperature	<i>K</i>
TAP	Taper constant	–
\mathcal{U}	Potential energy	<i>J</i>
U	Flow velocity	m/s
U_{avg}	Average velocity	m/s
U_{max}	Maximum velocity	m/s
U_{slip}	Slip velocity	m/s
V	Volume	m^3
$Y(n)$	Pair correlation function at contact	–
α	Accommodation coefficient	–
ϵ	Energy well depth	<i>J</i>
θ	Bond angle	<i>deg</i>
λ	Mean free path	<i>nm</i>
λ_{therm}	Thermostat scaling factor	–
μ	Viscosity	$kg/m \cdot s$
ϕ	Probability of a real collision	–
σ	Molecular diameter	<i>nm</i>
Δt	Time step	<i>fs</i>
Ω	Collision integral for Boltzmann equation	–

Summary

Gas flows in micro- and nanosystems are of great importance for various applications in semiconductor industry. Rarefaction and the small length scales in micro- and nanosystems cause the Navier-Stokes equation to break down, making the CFD solution invalid. For such conditions, particle based methods, such as Molecular Dynamics (MD) are preferred. The PumMa MD package is used and extended in order to study nanoscale flows and heat transfer: fully developed and developing flows in nanochannels, and outgassing of water molecules from a silicon/silica nanopore are studied.

A three dimensional MD simulation is used to study the effect of different nanochannel geometries on rarefied argon gas flows. Both fully developed and developing channel flows have been studied. For the fully developed flow, the velocity profiles in the channel are obtained and analyzed for three different channel geometries: a circular, a rectangular (square), and a slit channel. A channel width of $50nm$ is used for all simulations. It is found that when using the same driving force, the maximum velocity of the flow increases when the geometry changes in the order from circular to rectangular to slit geometry, where the latter becomes $2 \sim 2.5$ times as large compared with either the rectangular or circular channel. For a Knudsen number (Kn) larger than 1.0, the rectangular channel shows a similar maximum and slip velocity as the circular channel while the velocity profile is qualitatively similar to the slit channel. The effect of different Knudsen numbers on the velocity profiles is also investigated. We found that for Kn larger than $2 \sim 3$, the Knudsen number has a relatively small influence on the slip velocity for circular channels and rectangular channels. The effect of the accommodation coefficient on the average flow velocity for all three geometries is analyzed and an allometric equation model is derived. For the developing flow, a choked subsonic flow has been studied. The study focuses on the transition regime and goes up to the free molecular regime. The flow is driven by a pressure difference between the inlet and the outlet. The expansion flow at the outlet of the channel is accompanied by a temperature drop and a sudden increase in velocity. Causes behind the differences between three different geometries (circular, rectangular and slit) and two different situations (isothermal condition and heated wall condition) are analyzed and studied. The calculated velocity slip and temperature distribution are compared with the results from direct simulation Monte Carlo (DSMC) simulations. It is shown that

the DSMC method can accurately predict both flow and heat transport phenomena in $50nm$ nano channels in the transition regime, when the cell size is chosen much smaller than the typical bin size of the classical DSMC method.

For outgassing, we study materials which are commonly used in semiconductor industry: water and silicon and silica surfaces. In order to simulate the outgassing of water molecules in cracks and silicon/silica nanopores, it is necessary to develop a potential energy function for water and for the water-silicon/silica interactions. To develop a suitable water model for PumMa MD, a set of MD simulations of a modified TIP3P model and a ReaxFF based tabulated water model have been performed. The characteristic liquid density, self-diffusion coefficients, and radial distribution functions are determined and compared to experimental data. Our new tabulated water model provides $2 \sim 2.4$ times faster simulations than the other three site water models, and at the same time it provides a comparable liquid density and self-diffusion coefficient. For modelling flows and heat transfer, the interaction between the gas and the solid device surfaces is essential. However, water-silicon/silica interaction is generally not well modeled for non-reactive MD. Another problem is that a significantly high computational time is used when the wall molecules are explicitly modeled in MD simulations. To save computation time, implicit boundary functions are often used. Steele's potential has been used in studies of fluid-solid interface for a long time. The idea of Steele's potential is extended in order to simulate water-silicon/silica interfaces. A new wall potential model is developed based on an electronegativity-equalization method (EEM) based ReaxFF empirical force field and the non-reactive molecular dynamics package PumMa which allows a tabulated potential function as a input. Contact angle simulations have been performed in order to validate the wall potential model. Contact angle simulations with tabulated wall potentials showed Silicon contact angle of 129° , silica-quartz contact angle of 0° , and silica-cristobalite contact angle of 40° which are in reasonable agreement with experimental values. To add a friction like behavior to the tabulated wall model, Maxwell type diffusion has been implemented as well.

With the models now available, a complete nanopore simulation with a water-silicon interaction wall potential can be simulated. We investigate the important factors of outgassing by varying the temperature, the outlet pressure, the geometry (width and length) of the nanopore, and the materials of the nanopore. We observe a negligible effect of outlet pressure, while temperature plays an important role in the last stage of the outgassing process. A geometry effect is found closely related to the dominant outgassing mechanism in that situation. The material is very important for desorption. For materials with a low binding energy, like silicon, the desorption rates are so high that the corresponding molecules quickly desorb from the wall surface and cause no further problem in outgassing. For materials with a very high values of binding energy, like silica-quartz, the desorption rates are too small to have any outgassing.

Acknowledgements

This thesis came into existence with four years of work in the Energy Technology group at Eindhoven University of Technology (TU/e). These years I worked mostly at TU/e, but I have also been working at the University of Strathclyde in Glasgow and at INFICON in Liechtenstein. I met many people during this period and I thank all of them. They have contributed in the completion of this thesis in one way or another. The financial support from the GASMEMS (European Community's seventh Framework Program) is gratefully acknowledged as well.

First and foremost, I like to express my gratitude to my promotor Professor Anton van Steenhoven for his kind advices and insightful suggestions. During my PhD years, he patiently waited me to find my own way and guided me with his generous smile. I give deep thanks to my supervisors dr.ir. Arjan Frijns and dr. Silvia Nedeia. They have been supportive since the first day I started my PhD project, and helped me to keep myself on track. I would like to express my great appreciation to Linda who has been very kind and helpful with regard to most of the administrative tasks.

I sincerely thank the Committee members, prof.dr. A. Frezzotti, prof.dr.ir. C.R. Kleijn, prof.dr.ir. D.M.J. Smeulders, and prof.dr. P.A.J. Hilbers for assessment and valuable comments on my thesis. I would also like to thank dr. Yonghao Zang (University of Strathclyde) and dr. Martin Wuest (INFICON) for their advices and guidance during my GASMEMS secondments.

Of course I would like to thank all the GASMEMS members for the discussions and fun activities during the GASMEMS workshops we had. It was great to have friends working in the same field of interest. The discussions have provided new ideas, and I was not feeling alone when I went to conferences because of them.

The list of acknowledgement will not be complete without mentioning the people who made my stay in TU Eindhoven a memorable one. Firstly, I would thank Pieter van den Akker, who was my first office mate and laid the foundation of my work. I would also like to thank my other office mates Lakhdar, Esubalew, Felix, Mohammadreza for all the interesting talks and happy moment we shared together. Next, I would like to thank all my colleagues for all the fun events and coffee breaks we had. Henk, Erik, Kiran, Ilhan, Zhipeng, Konstantin, Daniel, Claire, Maurice, Shuiquan, Gökcalp, Bobby, Raluca, Manoj, Kees, Ernst, Amar,

Acknowledgements

Cong and Ding, thank you all for your friendship.

I would like to especially name Eldhose Iype. We started our PhD at nearly the same time and without him, I could have not finished my PhD. As I told him some time back, I thank God for sending him. I really enjoyed his friendship, discussions and the times we had together.

During my four years of PhD, I have gained a number of friends from different parts of Europe. I would like to thank all of them and special mentions to Hyun-Do, Young-Joon, Jang-min, Seulki, Wonmin, Sejong, YoonKyung, and Jungmi in Eindhoven. I would also like to thank Kara, Jiyeon, Judy, Mr and Mrs. Jang for the enjoyable times in Glasgow. I feel myself very lucky to meet you. Special thanks to Gloria, HyungKeun, and Jin for the continuous support from Germany. I would also like to thank MoonKyung and HeeSeon for the friendship throughout my PhD years.

At the very end, I would like to thank my family. This thesis is heartily dedicated to my parents who prayed all day and night for me throughout the time of my research. May the Almighty God richly bless all of you.

List of publications

Journal publications

- Kim, J., Frijns, A. J. H., Nedea, S. V., and van Steenhoven, A. A. Pressure calculations in nanochannel gas flows. *Journal of Physics: Conference Series - Proceedings of 1st European Conference on Gas MicroFlows (GASMEMS2012)*, 362:012020, 2012.
- Kim, J., Frijns, A. J. H., Nedea, S. V., and van Steenhoven, A. A. Geometry effects on rarefied nanochannel flows. *Microfluidics and Nanofluidics*, 15(5): 661-673, 2013.
- Kim, J., Iype, E., Frijns, A. J. H., Nedea, S. V., and van Steenhoven, A. A. Development of EEM based silicon-water and silica-water wall potentials for non-reactive molecular dynamics simulations. *Journal of Computational Physics*, 268: 51-62, 2014.

Conference proceedings

- Kim, J., Frijns, A. J. H., Nedea, S. V., and van Steenhoven, A. A. Development of a molecular dynamics simulation model for heat transfer in vapors, *Proceedings on CDROM of 2nd International GASMEMS Workshop (GASMEMS10)*, Les Embiez, France GASMEMS2010-HT07:1-6, 2010.
- Kim, J., Frijns, A. J. H., Nedea, S. V., and van Steenhoven, A. A. DSMC and MD simulation on geometry and rarefaction effect for nanochannel flow, *Proceedings on CDROM of 3rd International GASMEMS Workshop (GASMEMS11)*, Bertinoro, Italy, GASMEMS11-29:1-7, 2011.
- Kim, J., Frijns, A. J. H., Nedea, S. V., and van Steenhoven, A. A. The effects of geometry and Knudsen numbers on micro- and nanochannel flows. *Oral : Proceedings of the 9th International Conference on Nanochannels, Microchannels, and Minichannels (ICNMM 2011)*, June 19-22, Edmonton, Canada, ASME, 1-8, 2011.
- Kim, J., Frijns, A. J. H., Nedea, S. V., and van Steenhoven, A. A. Molecular Dynamics Simulation on Rarefied Gas Flow in Different Nanochannel

List of publications

- Geometries, *Proceedings of the 28th RGD Conference: Zaragoza, Spain*, 2012.
- Kim, J., Frijns, A. J. H., Nedeá, S. V., and van Steenhoven, A. A. Effects of expansion flow in nanochannels. *Proceedings of the 3rd European Conference on Microfluidics (μ Flu'12), Heidelberg, Germany*, 182: 1-10, 2012.

Curriculum vitae

Junghan Kim was born in Seoul (Republic of Korea) on February 29th, 1980. He attended United World College (UWC) of South East Asia in Singapore, where he obtained his high school degree in 1998. In the same year, he started his bachelor education in Mechanical Engineering at Korea Advanced Institute of Science and Technology (KAIST) in Korea. In 2004, he finished his Bachelor of Science studies and joined Bio-MedLab, Inc to work on micro-endoscope project. One year later, he left Bio-MedLab and joined the software company GIT, Co. as a software engineer for developing an automotive diagnostic system for Hyundai and KIA Motors. In October 2006, he left GIT and started his master's study at University of Stuttgart in January 2007. During his master's project at University of Stuttgart, he specialised in Molecular Simulation under supervision of prof. Jadran Vrabec. After obtaining his master's degree, JungHan started his PhD at Eindhoven University of Technology in the Energy Technology group of prof. Anton van Steenhoven (currently headed by prof. David Smeulders). During his PhD period he spent 6 months at University of Strathclyde (Glasgow, Scotland) and 3 months at INFICON (Liechtenstein) as secondments of his PhD project. The results of his PhD work are presented in this thesis.